University of Alberta

In-Situ Spectroscopic Characterization of
Operating Polythiophene Nonvolatile Memory Devices

by

Xiangyu Chen

A thesis submitted to the Faculty of Graduate Studies and Research
in partial fulfillment of the requirements for the degree of

Master of Science

Department of Chemistry

Spring 2014
Edmonton, Alberta

Dedicated to my family

ABSTRACT

Au/P3HT/PEO-EV(ClO_4)$_2$/C/Au nonvolatile memory devices were developed based on resistive switch of conducting polymers in the solid state. The P3HT layer was switched using a “write/erase” bias, while internal composition of the device was monitored using in-situ UV-Vis absorbance spectrometer coupled with electronic measurement system. Optical absorption and conductivity changes revealed reversible transition between P3HT neutral and polaron forms, which had different conductance and absorbance at OFF and ON states of the memory device. The results demonstrated the redox reaction in solid state devices, and directly correlate absorption and device conductivity. Finally, a polaron propagation mechanism was proposed and confirmed using a simplified dual pulse experiment setup. The reported results provide an understanding of the mechanism in nonvolatile polymer memory devices, which can be used to improve the memory performance and evaluate possible commercial applications.

ACKNOWLEDGEMENTS

First, I would like to deeply thank my supervisor, Dr. Richard McCreery, for his encouragement and financial support during my master studies in his research group. This thesis cannot be accomplished without his wide knowledge, understanding and encouragement. I really thank for his detailed guidance, logic way of thinking and patience, which makes my research quick and smooth.

Second, I would like to give my sincere thanks to Dr. Nils Petersen and Dr. Michael Serpe, for their encouragement and patient discussion in research. The suggestions and knowledge I got are really helpful.

Third, I would like to thank all the group members in the Dr. McCreery group, for their kind help and friendship. Specifically, I want to give my sincere thanks to Dr. Adam Bergren and Bryan Szeto, for their kind help on designing the research instrument and software. I want to thank Dr. Nikola Pekas and Dr. Haijun Yan for their creative research discussion, mentoring on operation of research procedures and patient scientific instrument training. I would like to thank Dr. Rajesh Pillai and Dr. Bikas Das and Dr. Sayed Nagy for their useful and helpful discussion. I also want to show my warm thanks to Dr. Amr Mahmoud, Jerry Fereiro and Akhtar Bayat, who always provide kind help with warm heart and smile.

Additionally, I would like to give my thanks to Mr. Dieter Starke, who helped design and fabricate special and exquisite sample holders with great patience.

Finally, and most importantly, I would like to give my sincere thanks to my family, for their understanding, encouragement and love. Thank my parents, Yaping Pang and Xiaodong Chen, for raising me up and endless love. Thank my grandparents for their understanding and encouragement throughout my life. Specially, I would like to thank my fiancée, Xinrui Ma, for her continuous support and understanding since we met. I cannot achieve anything without their love.

TABLE OF CONTENTS

Chapter 1 1

Introduction 1

1.1 Introduction of Nonvolatile Memory Device 1

1.2 Resistive Switching Memory 3

1.2.1 Structure of Resistive Switching Memory 3

1.2.2 Classification of Resistive Switching 6

1.2.3 Materials used in Memory Devices 8

1.2.4 Resistive Switching Mechanism 13

1.2.4.1 Charge Transfer 13

1.2.4.2 Ionic Conduction 15

1.2.4.3 Conformational Change 16

1.2.4.4 Space Charge and Traps 17

1.2.4.5 Filamentary Conduction 17

1.2.5 Requirements of Memory Performance 18

1.2.5.1 Writing Process 19

1.2.5.2 Reading Process 19

1.2.5.3 Erasing Process 19

1.2.5.4 ON/OFF Ratio 19

1.2.5.5 Cycle Life 20

1.2.5.6 Retention Time 20

1.3 Characterization of Memory Devices 21

1.3.1 Electronic Characterization of Memory Devices 21

1.3.1.1 Current-Voltage Characterization of Memory Device 22

1.3.1.2 Pulse Current-Voltage Characterization of Memory Device 24

1.3.2 Spectroscopic Characterization of Memory Devices 25

1.3.2.1 Raman Spectroscopy 25

1.3.2.2 UV-Vis Spectroscopy 28

1.4 Research Objective 31

Chapter 2 34

Fabrication and OPTICAL MONITORING of Polythiophene Nonvolatile Memory Devices 34

2.1 Introduction 34

2.2 Device Fabrication 37

2.2.1 Fabrication of Bottom Electrodes 39

2.2.1.1 Wafer Cleaning 39

2.2.1.2 Deposition of Cr/Au 39

2.2.1.3 Photolithography 40

2.2.2 Polythiophene Layer Preparation 42

2.2.3 Electrolyte Layer Preparation 46

2.2.4 Deposition of Top Contacts 52

2.3 In-situ Optical Monitoring System 55

2.3.1 Apparatus used for solution experiment 55

2.3.2 Apparatus used for measuring repetitive write/read/erase/read memory cycles 58

2.3.3 Apparatus used for measuring memory switching characteristics .. 60

2.4 Summary 62

Chapter 3 63

In-Situ Spectroscopic Characterization of Memory Devices 63

3.1 Introduction 63

3.2 Results and discussion 65

3.2.1 Spectroelectrochemistry in Solution 65

3.2.2 Absorption Spectroscopy in Solid State Devices 76

3.2.3 Dual Pulse Experiment 87

3.2.4 Polaron propagation and device switching mechanism 94

3.3 Summary 100

Conclusions and future work 101

Bibliography 103

LIST OF TABLES

Table 1-1 Glossary of materials abbreviations 9

Table 2-1 Spin coater program for P3HT layer deposition..... 43

Table 2-2 Formula of PEO- $EV(ClO_4)_2$ solution 48

Table 3-1 Calculated concentrations of P3HT neutral and polaron forms 71

Table 3-2 RC constant of system 99

LIST OF FIGURES

Figure 1.1 Various nonvolatile solid state memory devices applications by market size (2009) 2

Figure 1.2 Schematic illustration of a resistive switching memory cell 3

Figure 1.3 Sketch of a cross-bar memory array with the memory material sandwiched between the bottom contacts and the top contacts 4

Figure 1.4 (a) Schematic illustration of a 3D-stacked organic resistive memory assembly featuring a 8 × 8 crossbar structure (b) Cross-sectional TEM image of the stacked device highlighting the three layers of organic memory cells. (c) The chemical structures of cured PI and PCBM used as the memory material 5

Figure 1.5 Classification of resistive electrical switching effects for nonvolatile memory applications 6

Figure 1.6 The two basic operation schemes of resistance switching memory cells. a) Unipolar switching b) Bipolar switching 7

Figure 1.7 Structure of poly (3-hexylthiophene). 11

Figure 1.8 Regio-regular poly-3-hexylthiophene with edge-on orientation of the polymer chains 11

Figure 1.9 (a) Absorption extinction co-efficient (red line), excitation spectrum (dotted black line) and emission spectrum (green line) for 93% RR P3HT in solution at 4×10^{-5} mol/L concentration. (b) Absorption co-efficient (red line), excitation spectrum (dotted black line) and emission spectrum (green line) for the 93% RR P3HT film 12

Figure 1.10 Chemical structure of TCNQ, $TCNQ^{\cdot -}$ and $TCNQ^{2-}$ 14

Figure 1.11 Chemical structure of Rose Bengal in its (a) neutral state, state 1, (b) reduced state without any conformational change, and (c) reduced state with conformational change, state 3 16

Figure 1.12 Histogram of ON and OFF state currents for 210 cycles of a device containing Al NPs 20

Figure 1.13 Wiring schematics for (a) two-, (b,c) three-, and (d) four-wire measurements of current–voltage (i-V) behavior of molecular junctions 23

Figure 1.14 Memory pulse measurement program containing write, erase and read waveform: three pulses, four levels 24

Figure 1.15 (a) Device schematic with bias polarities. The 1-μm channel is visible as a horizontal line in the left image. (b−d) Raman line scan image from three-terminal devices for the indicated bias values, composed of ten spectra acquired along the line between D and S..... 27

Figure 1.16 Electronic molecular energy levels..... 29

Figure 1.17 (a) ΔA of NAB/SiO2 after a -4 V pulse and subsequent +4 V pulse. ΔA of the two voltage pulses are nearly symmetric about zero ΔA; (b) ΔA of a NAB/SiO_2 at 410 nm before and after a -4 V pulse..... 31

Figure 2.1 Schematic of memory devices under investigation (a) three terminal device with Gate, Drain and Source geometries. Chemical structures of (b) neutral form of P3HT (c) PEO and (d) ethyl viologen diperchlorate 36

Figure 2.2 Process flow chart for the fabrication of Polythiophene Nonvolatile Memory Devices..... 38

Figure 2.3 Transmittance Spectra of 10nm Cr and 100nm Au layers deposited on quartz wafer, simulated by Filmstar..... 40

Figure 2.4 Top view of completed bottom electrodes using microscope 42

Figure 2.5 Top view of substrates with spin coated P3HT layer using microscope. 43

Figure 2.6 AFM images ($5\times5\mu m^2$) of spin-coated P3HT layer using tapping mode and contact mode respectively. (a) Rms roughness of P3HT layer (Ra) is 1.8nm.

(b) Thickness of P3HT layer is 26.2nm using Gaussian Fits. (c) Statistical depth profile for the image in (b). 45

Figure 2.7 Drop coated ethyl viologen diperchlorate separated in polyethylene oxide matrix, with a valley shape in cross section. 46

Figure 2.8 Effect of concentration and spin speed on PEO layer thickness and rms roughness 48

Figure 2.9 Spin coated PEO layer using the indicated conditions on P3HT surface. (a)1% PEO did not stick to P3HT layer because of the low viscosity. (f) Crystal patterns formed at high spin speed and high concentration of PEO, and resulted in much higher roughness. 49

Figure 2.10 Top view of substrates with spin coated PEO layer using microscope. 51

Figure 2.11 SEM images of spin coated PEO-EV$(ClO_4)_2$ layers. (a) PEO-EV$(ClO_4)_2$ solution formed uniform solid layer after spin coating with thickness of 550±20 nm. (b) A zoom out image shows 550nm PEO-EV$(ClO_4)_2$ on 100nm Au layer. (c) Top view of spin coated PEO-EV$(ClO_4)_2$ layer. 51

Figure 2.12 Top view of completed devices with top contacts using microscope.53

Figure 2.13 Transmittance Spectra of 10nm C and 20nm Au layers, simulated by Filmstar 53

Figure 2.14 Transmittance of bottom and top electrodes using apparatus demonstrated in 2.3.2 with exposure time of 0.1s 54

Figure 2.15 Schematic of optical system Setup used for solution experiment 57

Figure 2.16 Schematic of In-situ optical system used for monitoring repetitive write/read/erase/read memory cycles 59

Figure 2.17 Schematic of electronic measurement part used for testing memory characteristics 61

Figure 3.1 Cyclic voltammetry of solid P3HT film spin coated on quartz/C/Au substrates 65

Figure 3.2 Absorbance changes at 560nm and 650nm during the cyclic voltammetry of solid P3HT film in acetonitrile containing 1.0M TBHFP versus $Ag/AgNO_3$ reference electrode 66

Figure 3.3 Spectroelectrochemistry characterization of P3HT film in 0.1M TBHFP acetonitrile solution 70

Figure 3.4 Fitting of Nernst equation using the concentration data calculated from Beer's Law 71

Figure 3.5 Correlation of A_{560nm}, A_{650nm} and current when constant voltage is applied for 30s 74

Figure 3.6 Fitting of Cottrell equation using current and time data from 2s to 2.5s. (a) Fitting using oxidation data. (b) Fitting using reduction data. 75

Figure 3.7 Absorption spectra of memory channel when different constant V_{SG} is applied 76

Figure 3.8 ΔAbsorbance of P3HT film in (a) solid state and (b) solution, showing isosbestic point at around 610nm 78

Figure 3.9 Correlation of A_{560nm}, A_{650nm} and V_{SG} in $Au/P3HT/PEO+EV(ClO_4)_2/C/Au$ memory device 79

Figure 3.10 MCR analysis of absorption spectra obtained during different constant bias is added to Source and Gate electrodes of memory device. (a)MCR calculated spectra of two components in the P3HT layer. (b)MCR calculated loading of the two components during constant potential is applied. 81

Figure 3.11 In-situ detection and correlation of A_{560nm}, A_{650nm} and I_{SD} on working memory device. (a) In the W/R/E/R cycles, V_{SG} is applied as 4V to write the device and -4V to erase, both for 1s. (b) I_{SG} is recorded during memory switching process. (c) V_{SD} is always applied as 0.5V to read out memory device status continuously. (d) SD current (e) Absorbance at 560nm (f) Absorbance at 650nm are used to identify the ON and OFF states 83

Figure 3.12 In-situ detection and correlation of A_{560nm}, A_{650nm} and I_{SD} on working memory device in (a) open circuit and (b) closed circuit. 85

Figure 3.13 In-situ detection of memory retention time in (a) open circuit and (b) closed circuit. 86

Figure 3.14 Characteristics of memory device during writing process using fast dual pulse system in (a) open circuit and (b) closed circuit..... 89

Figure 3.15 SD Current, ΔA_{560nm} and ΔA_{650nm} response of a P3HT memory device in the writing process using dual-pulse measurements under air, nitrogen, and acetonitrile vapor conditions. (a) SD current (b) ΔA_{560nm} and (c) ΔA_{650nm} response corresponding to the 1 second writing process 92

Figure 3.16 SD Current, ΔA_{560nm} and ΔA_{650nm} retention response using dual-pulse measurements under air, nitrogen, and acetonitrile vapor conditions. (a) SD current (b) ΔA_{560nm} and (c)ΔA_{650nm} response after writing process for 80s..... 93

Figure 3.17 Proposed polaron propagation mechanism. EV is ethyl viologen and P is P3HT 95

Figure 3.18 (a) SG and SD current recorded by high resolution detection system. (b) SD current in the beginning of writing process..... 97

Figure 3.19 Propagation time of 4 memory devices using high resolution detection system with 0.375 μs resolution. (a)SG current (b) SD current (c)SD current in log scale in order to show the propagation time. 98

LIST OF ABBREVIATION

6T-PEO	sexithiophene-poly(ethylene oxide)
ACN	acetonitrile
CMOS	complementary metal–oxide–semiconductor
DCB	1,2-dichlorobenzene
$EV(ClO_4)_2$	viologen diperchlorate
HOMO	highest occupied molecular orbital
LUMO	lowest unoccupied molecular orbital
MCR	multivariate curve resolution
MOSFET	metal–oxide–semiconductor field-effect transistor
NAB	nitroazobenzene
NVM	nonvolatile memory
P3HT	poly(3-hexylthiophene)
P6OMe	poly[3-(6-methoxyhexy)thiopene]
PCBM	[6,6]-phenyl-C61-butyric acid methyl ester
PEDOT:PSS	poly(3,4-ethylenedioxythiophene) poly(styrenesulfonate)
PEO	poly(ethylene oxide)

PS	polystyrene
SCLC	space charge-limited current
TCNQ	tetracyanoquinodimethane
TFT	thin film transistor
TOF-SIMS	time-of-flight secondary ion mass spectrometry
TTF	tetrathiofulvalene
WORM	write once read many

CHAPTER 1

INTRODUCTION

1.1 Introduction of Nonvolatile Memory Device

"Portable" consumer electronics have become pervasive in recent years in the form of cell phones, music players, memory sticks, etc. Approximately 95% of the common devices shown in Figure 1.1 use solid-state nonvolatile memory (NVM), which currently comprises a ~$65 billion/year market, not counting disk drives.[1] The most common form of NVM is "flash" memory based on the silicon "floating gate". However, silicon-based NVM requires a high voltage to operate, and has limited cycle life. Among various alternative to current solid state memory devices, polymer memory devices show significant promise, with two reviews of research in the area appearing recently.[2, 3] These polymer molecules with unique structure have distinctive behaviours and functions not currently available with silicon, specifically including lower manufacturing cost, low energy demand and possibly longer lifetime.

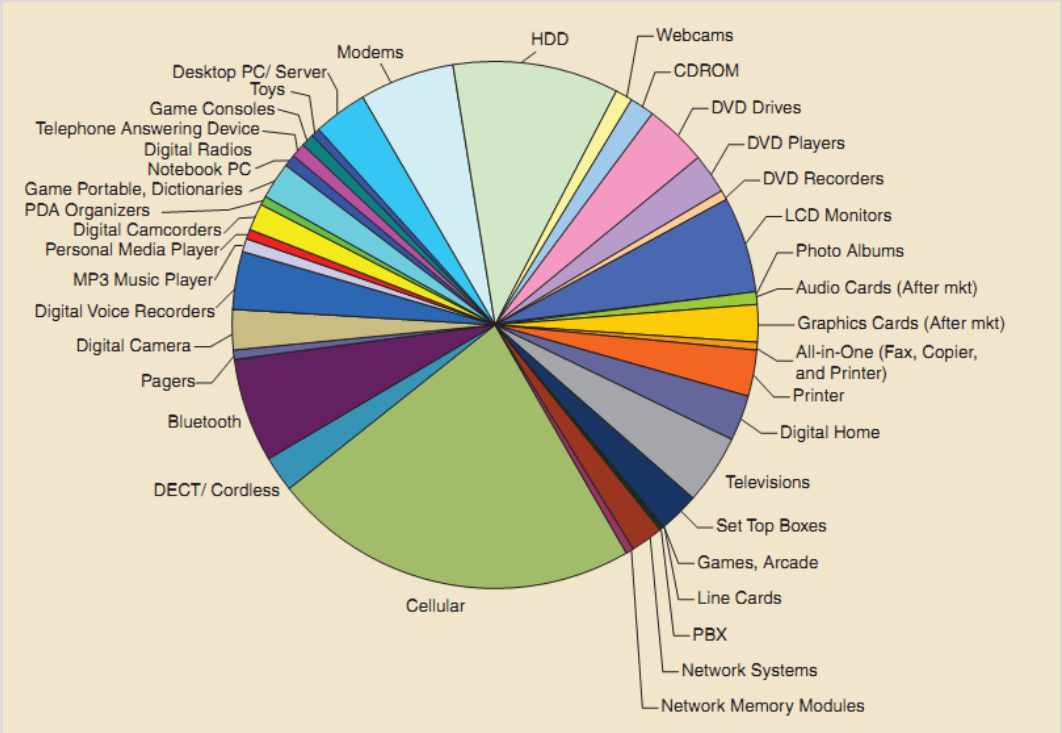

Figure 1.1 Various nonvolatile solid state memory devices applications by market size (2009), Solid state nonvolatile memory has enabled the rapid growth of portable electronics. Reprinted with permission from ref 1.[1] © [2009] IEEE.

The candidate's research group at the National Institute for Nanotechnology is developing NVM based on resistive switching accompanying "dynamic doping" of conducting polymers through redox reactions in the solid state. The current project collaborates with the Xerox Research Centre of Canada (Mississauga) to investigate polythiophene for NVM applications. A critical problem in this research is determining the redox changes in the polymer, which ultimately control its conductivity. Direct structural probes of working microelectronic devices are quite rare, and we have demonstrated the value of "live" monitoring in previous research.[4-7]

1.2 Resistive Switching Memory

1.2.1 Structure of Resistive Switching Memory

Typically, resistive switching memory has a two-terminal structure, in which at least one resistive switchable material is sandwiched between the (possibly different) bottom and top electrodes, as shown in Figure 1.2. The layer between the electrodes can be either inorganic or organic material, but usually has a high conducting ON state and a low conducting OFF state, which can be programmed from one to another by application of a voltage through the electrodes.

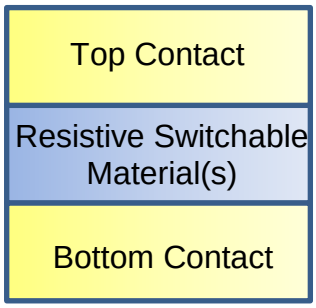

Figure 1.2 Schematic illustration of a resistive switching memory cell.

This two-terminal device can be easily placed on the substrate to form a low density cross-bar memory array (Figure 1.3). Current research includes attempts to integrate resistive switching memory cell with commercial fabrication techniques of the semiconductor industry, such as complementary metal–oxide–semiconductor (CMOS) technology, in order to achieve high density, massively parallel processing and low cost.

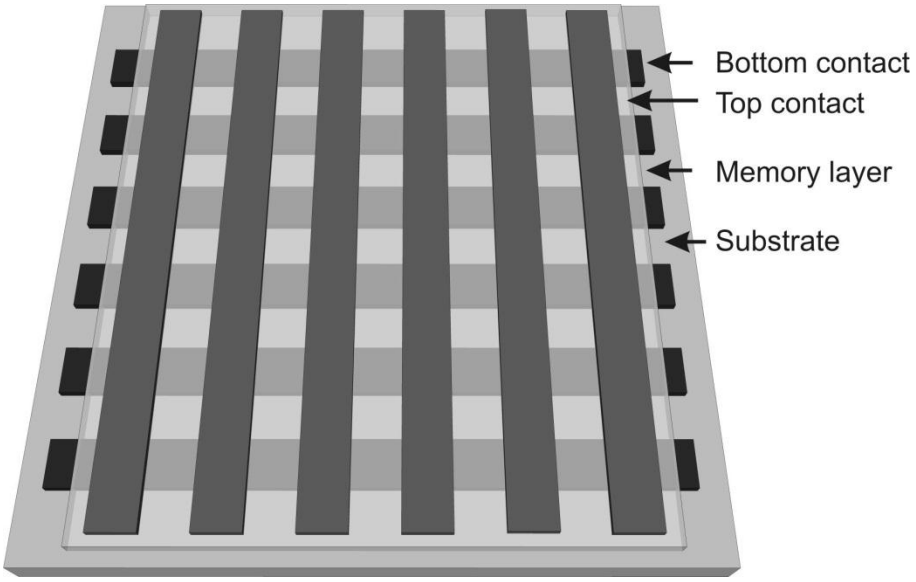

Figure 1.3 Sketch of a cross-bar memory array with the memory material sandwiched between the bottom contacts (horizontal lines) and the top contacts (vertical lines). Reprinted with permission from "Polymer and Organic Nonvolatile Memory Devices". Copyright (2011) American Chemical Society.[3]

However, organic memories so far have a low data density for data storage applications, which limits their commercial practicality.[8-11] In order to solve this issue, Song et al. proposed a three-dimensional stacking cross-bar polymer resistive memory array to increase memory cell density, shown as Figure 1.4.[12] A PI:PCBM composite layer was successfully employed as the resistive switching layer between Al electrode layers, and achieved 83% fabrication yield. The memory cells in every layer performed well with respective writing and erasing, and exhibited a reasonable extrapolated memory retention time over 8000h.

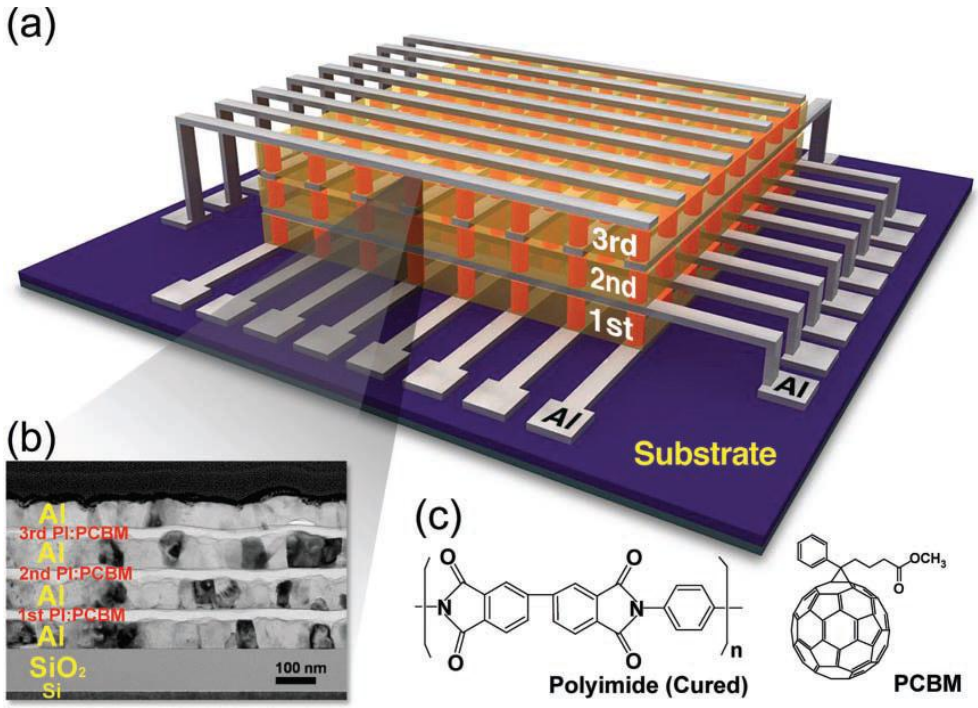

Figure 1.4 (a) Schematic illustration of a 3D-stacked organic resistive memory assembly featuring a 8 × 8 crossbar structure. A total of 192 cells (coloured range) were produced in three active layers (coloured yellow) sandwiched between pairs of Al electrode layers. (b) Cross-sectional TEM image of the stacked device highlighting the three layers of organic memory cells. (c) The chemical structures of cured PI and PCBM used as the memory material. **R**eprinted with permission from ref 12.[12] Copyright © 2010 WILEY-VCH Verlag GmbH & Co. KGaA, Weinheim.

1.2.2 Classification of Resistive Switching

Figure 1.5 shows a classification of resistive switching methods based on physical and chemical principles. Thermal effects, electronic effects and electrochemical effects have been discovered within organic nonvolatile memory devices.[3]

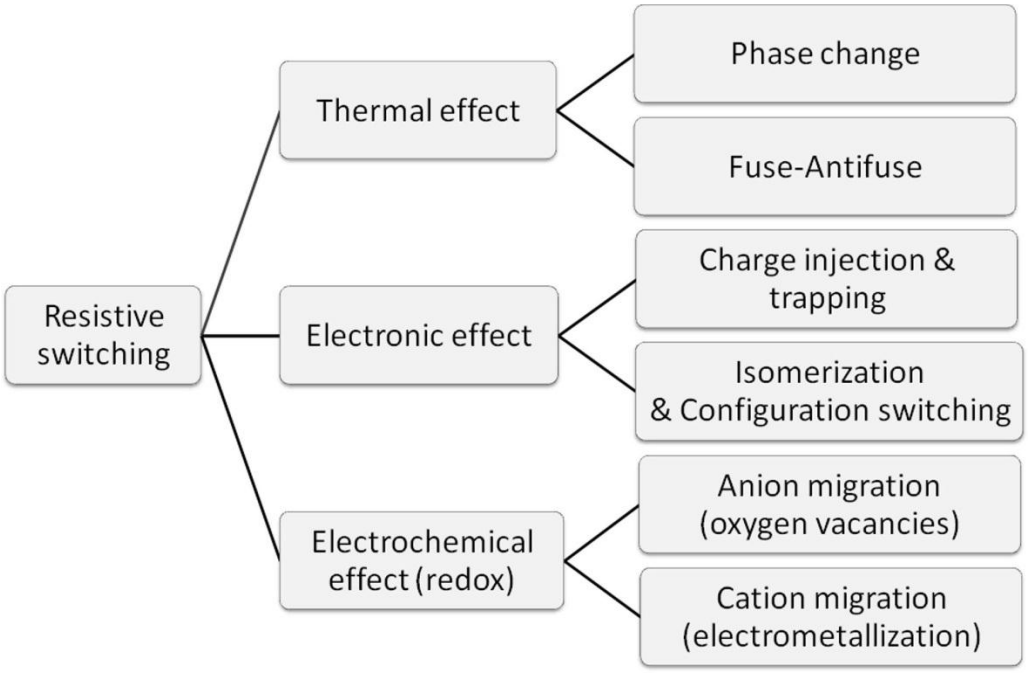

Figure 1.5 Classification of resistive electrical switching effects for nonvolatile memory applications. Reprinted with permission from "Polymer and Organic Nonvolatile Memory Devices". Copyright (2011) American Chemical Society.[3]

In order to record data in the memory device, a low conducting OFF state is shifted to a high conducting ON state by a current or voltage applied between the resistive layer(s). Based on the electrical polarity required for resistive switching, the two schemes can be distinguished: unipolar switching operation and bipolar switching operation (Figure 1.6).[13] The unipolar switching operation does not depend on the write (SET) voltage polarity. The erase

(RESET) process into the OFF state happens at a voltage below the write voltage. In contrast, bipolar switching operation occurs when the SET to the ON state happens at one polarity of voltage and the RESET to the OFF state happens at the opposite voltage polarity.

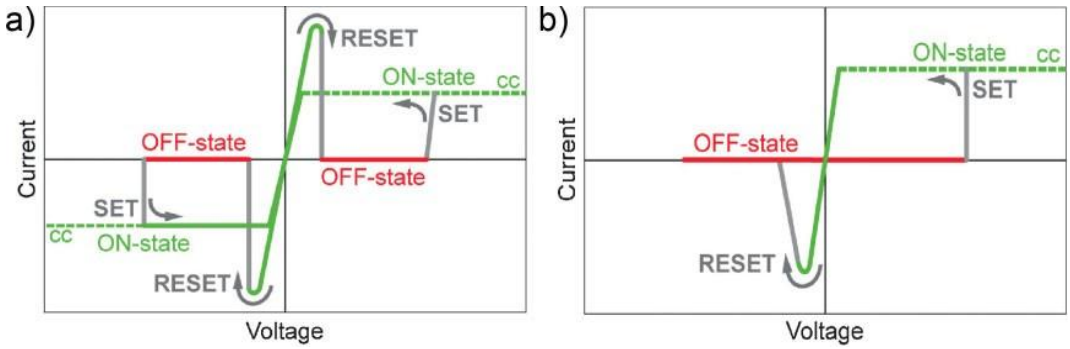

Figure 1.6 The two basic operation schemes of resistance switching memory cells. I–V curves recorded for a triangular shaped voltage signal. cc denotes the compliance current. Dashed lines indicate that the real voltage at the system will differ from the control voltage because of the cc in action. a) Unipolar switching. The SET voltage is always higher than the RESET voltage, and the RESET current is always higher than the cc during SET operation. b) Bipolar switching. The SET operation occurs on one polarity of the voltage or current, the RESET operation requires the opposite polarity. In some systems, no cc is used. Please note that the I–V curves of real systems may deviate considerably from these sketches, for both operation schemes. Reprinted with permission from ref 13.[13]

1.2.3 Materials used in Memory Devices

In 1968, Gregor first reported a resistive switching behavior in organic devices.[14] During the nearly five decades since this study, a great variety of organic semiconductor materials has been proposed and synthesized, and used in organic memory devices. These memory devices have been regarded as advanced devices with their low cost fabrication by ink-jet printing or spin-coating.[8-10, 15]

Table 1-1 shows a brief summary of different materials used in nonvolatile memory devices.[2] Usually, at least two materials are used to make one memory device, like P3HT with PEO-ethyl viologen,[16] poly(vinyl alcohol) with PCBM, [17] PCDF-PTrFE with pentacene,[18] and PCDF-PTrFE with MEH-PPV.[19]

Table 1-1 Glossary of materials abbreviations. Reprinted with permission from ref 2 [2]. Copyright © 2007 WILEY-VCH Verlag GmbH & Co. KGaA, Weinheim

Acronym	Common or IUPAC name
2NT	2-naphthylthiol
6T	Sexi-thiophene
8HQ	8-hydroxyquinoline
AIDCN	2-amino-4,5-imidazoledicarbonitrile
Alq3	Aluminum tris(8-hydroxyquinolate)
BDCP	2,6-bis(2,2-biscyanovinyl)pyridine
BET	2-benzene-ethanethiol
C1-C10	Poly(2-methoxy-5(2'-ethyl)octoxy-phenylenevinylene)
C545T	Coumarin 545T
CDHAB	4'-cyano-2,6-dimethyl-4-hydroxy azobenzene
CNPF	Poly(9-malonitrylfluorene); "cyanopolyfluorene"
CNT	Carbon nanotube
CuPc	Copper phtalocyanine
DC	Decacyclene
DCJBT	4-(Dicyanomethylene)-2-*t*-butyl-6-(1,1,7,7-tetra-methyljulolidyl-9-enyl)-4H-pyran
DCM2	[2-methyl-6-[2-(2,3,6,7-tetrahydro-1H,5H-benzo[i,j]quinolizin-9-yl)-ethenyl]-4H-pyran-4-ylidene] propane-dinitrile
DDQ	2,3-dichloro-5-6-dicyano-1,4-benzoquinone
DMA	9,10-dimethylanthracene
DT	1-dodecanethiol
EuVB	Europium vinylbenzoate complex
HMDS	Hexamethyldisilazane
ITO	Indium-tin-oxide
MEH-PPV	Poly(2-methoxy-5(2'-ethyl)hexoxy-phenylenevinylene)
NBMN	3-nitrobenzyl malonitrile
NiPc	Nickel phthalocyanine
NPB	*N*,*N*'-di(naphthalene-1-yl)-*N*,*N*'-diphenyl-benzidine
P3HT	Poly(3-hexylthiophene)
P6OMe	Poly[3-(6-methoxyhexyl) thiophene]
PAH	Poly(allylamine-hydrochloride)
PBMA	Poly(butylmethacrylate)
PCBM	6,6-phenyl-C61-butyric acid methyl ester
pDA	1,4-phenylenediamine
PEDOT	Poly(ethylenedioxythiophene)
PEMA	Poly(ethylmethacrylate)
PEO	Poly(ethylene oxide)

PMMA	Poly(methylmethacrylate)
PPhA	Poly(phenyl acetylene)
PS	Polystyrene
PSF	Poly(spirofluorene)
PSS	Poly(styrene-sulphonate)
PTFE	Poly(tetrafluoethylene)
PTrFE	Poly(trifluoroethylene)
PVDF	Poly(vinylidene difluoride)
PVK	Poly(vinylcarbazole)
TAPA	(+)-2-(2,4,5,7-tetranitro-9-fluorenylideneaminooxy)propionic acid
TCNQ	Tetracyanoquinodimethane
TDCN	Toluylene 2,4-dicarbamidonitrile
TPD	*N*,*N*'-diphenyl-*N,N'*-bis(3-methylphenyl)-1,1'-biphenyl-4,4'-diamine
TPP	Triphenylphosphine
TTF	Tetrathiafulvalene
xBP9F	Crosslinked poly[biphenyl-(9-fluorenyl)-methylene]
xHTPA	Crosslinked poly(hexyl triphenylamine)

Among all the well-known conducting polymers, polythiophene and its derivatives [poly(3-alkylthiophenes)] have attracted particular attention because of their excellent electrical and chemical properties.[20, 21] These polymers can be dissolved by common organic solvents, which makes solution-processing possible. As a result, they are widely used in various applications: memory devices,[22, 23] solar cells,[24] light emitting diodes,[25] etc. Particularly, poly(3-hexylthiophene) (P3HT, Figure 1.7) has continuously drawn researchers' attention, due to its solubility in common solvents, reported high charge carrier mobility of 0.05 to 0.1 $cm^2\ V^{-1}\ s^{-1}$, [26] and a band gap of ~2.0 eV.[27] When deposited on suitable substrates, regioregular P3HT, which means P3HT only contain head-to-tail (HT) couplings, usually self-assembles into a highly ordered thin film from solution in well-controlled conditions (Figure 1.8). [28-30]

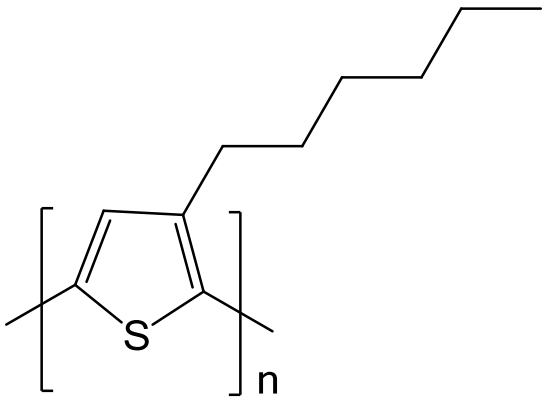

Figure 1.7 Structure of poly (3-hexylthiophene).

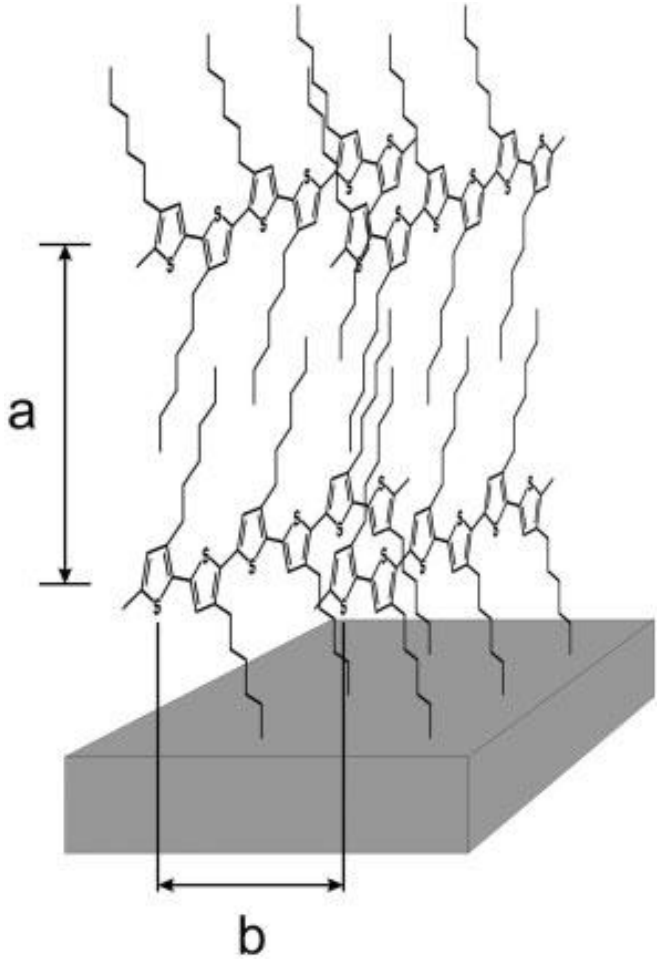

Figure 1.8 Regio-regular poly-3-hexylthiophene with edge-on orientation of the polymer chains. Reprinted with permission from ref 30.[30] Copyright © 2006 Wiley-VCH Verlag GmbH & Co. KGaA

Cook et al.[31] reported spectra of P3HT neutral and polaron forms by generating P3HT polaron with a laser in solution and thin film, as shown in Figure 1.9. P3HT neutral and polaron forms respectively had peaks at 455nm and 585nm in solution. However, in solid thin film, there were red shifted, where neutral form had a peak at 519nm and the peak of polaron form was located at 730nm, and the intensity was much weaker. Because there was no counterion to stabilize the polaron form, the excited P3HT had a very short life time of few hundreds ps.

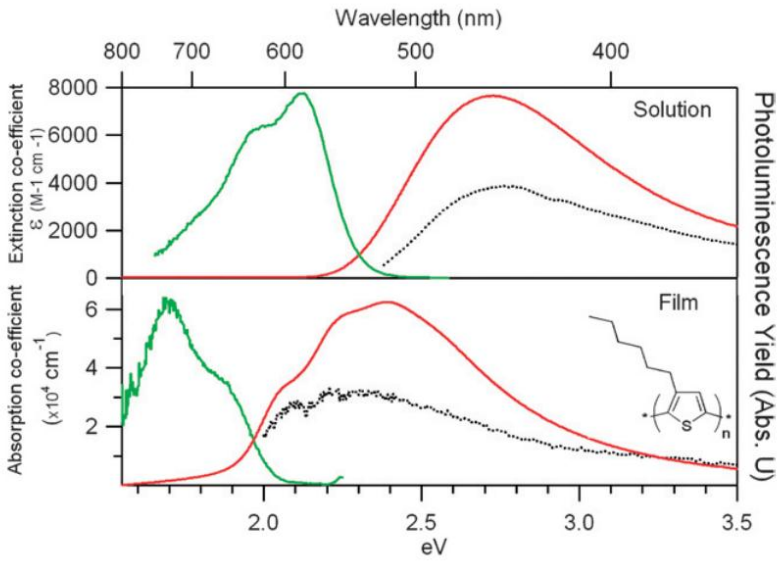

Figure 1.9 (a) Absorption extinction co-efficient (red line), excitation spectrum (dotted black line) and emission spectrum (green line) for 93% RR P3HT in solution at 4 $\times 10^{-5}$ mol/L concentration. Note extinction co-efficient refers to moles of the P3HT monomer unit (Mw 169) (b) Absorption co-efficient (red line), excitation spectrum (dotted black line) and emission spectrum (green line) for the 93% RR P3HT film. Film thickness is ~80 nm. Excitation wavelength for emission spectra was the absorption peak maximum while excitation spectra were taken at the emission maximum. Chemical structure of the P3HT monomer is given as an inset. Reprinted with permission from ref 31. [31]

In conclusion, organic semiconductor materials must have proper electronic structure to provide ideal charge-carrier transport mobility. [32] Meanwhile, these materials also need to show good air stability, in order to achieve low-cost ambient massive fabrication, as well as resistance to complex environmental effects. Finally, an ability to self-assemble from solution to generate proper structural order in thin film is required. Among all the organic semiconductor materials, conducting polymers are more amenable to solution-based techniques. Regioregular P3HT can satisfy these three requirements, make fabrication of nonvolatile memory device possible.

1.2.4 Resistive Switching Mechanism

Resistive memory devices are based on the principle that the material changes its conductivity when a ‘‘writing’’ or ‘‘erasing’’ voltage is applied. Herein, the conductivity can be defined as the product of (1) the concentration of mobile charges and (2) the charge carrier mobility. A change of either of them or both can leads a change in conductivity. In this section, different switching mechanisms of organic memory devices are reviewed. A more detailed discussion of mechanism is reported in a recent review paper. [33]

1.2.4.1 Charge Transfer

Charge transfer happens in an electron donor-acceptor system, in which charges transfer (partially) from the donor to the acceptor.[34-36] It is assumed that field-induced transfer is the most expected mechanism in charge-transfer complexes. Kamitsos et al.[36] reported a project on Cu-

tetracyanoquinodimethane (Cu-TCNQ), where Cu was the donor and TCNQ performed as the organic acceptor. Raman spectroscopy showed that high resistance TCNQ anions in the film were changed to neutral TCNQ molecules in a relative low resistance state. The molecular structure change is shown as Figure 1.10, as one electron is taken out, the central ring will be aromatized and B3 will become single bond, result in a higher resistance.(Note that one C is not shown between the end N and C in resonance structure since the N-C-C resonance bond is always straight) Chu et al. [34] also found a charge transfer phenomenon between [6,6]-phenyl-C61-butyric acid methyl ester (PCBM) and tetrathiofulvalene (TTF) dispersed in polystyrene (PS) film, in which TTF was the organic electron donor and PCBM was the acceptor. When an electric field was applied, electrons from the highest occupied molecular orbital (HOMO) of TTF were transferred to the lowest unoccupied molecular orbital (LUMO) of PCBM, resulted in a positively charged TTF and a negatively charged PCBM, as well as a conductance increase.

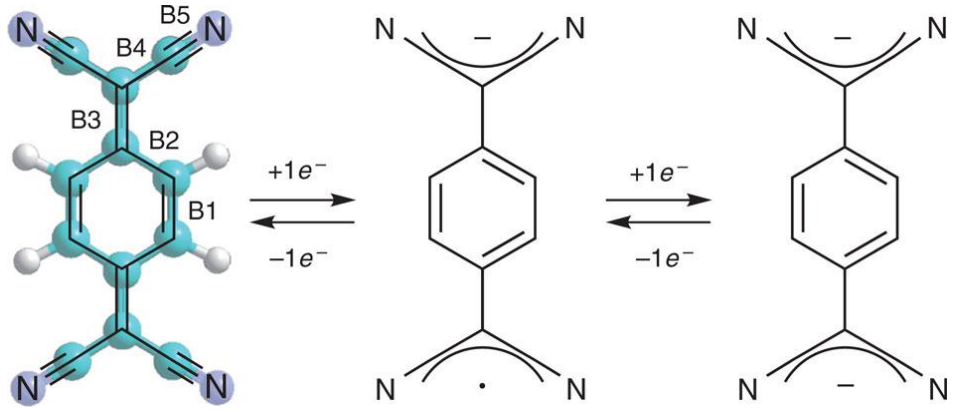

Figure 1.10 Chemical structure of TCNQ, $TCNQ^{\cdot-}$ and $TCNQ^{2-}$. In the neutral form the bond B3 in TCNQ is double and the central ring is not aromatic. The uptake of at least one electron, however, aromatizes the central ring, changing B3

from double to single and enhancing the conformational freedom of the molecule. **R**eprinted with permission from ref 37.[37]

1.2.4.2 Ionic Conduction

Ionic conduction usually occurs in polymers which have ionic groups, or in polymer matrix to which ionic materials are added.[33] The transition of ions requires relatively high activation energy and long transit time. Electrically rewritable switching behaviors have been reported in memory devices containing P3HT [38] and a sexithiophene-poly(ethylene oxide) (6T-PEO) block copolymer [39]. $LiCF_3SO_3$ and NaCl were added into the second PEDOT:PSS layer as dopants.[38, 39] Meanwhile, ethylene carbonate (EC) was used as plasticizer to enhance the mobility of inorganic ions.[38-40] Thus sandwich structure memory devices containing two stacked polymer layers were made with the configuration of ITO/PEDOT:PSS($LiCF_3SO_3$,EC)/P3HT(EC)/Al and ITO/PEDOT:PSS(NaCl,EC)/6T-PEO/Al, respectively [38, 39]. The memories are partially non-volatile with a retention time of roughly 10 minutes at room temperature. The authors reasoned that the migration of dopant ions into and out of the P3HT or 6T-PEO layer at the Al Schottky contact led to electrical bistability [38, 39]. For example, in the case of 6T-PEO, the electrochemical doping of 6T happened at both electrodes under the application of a forward bias.[39] At the interface between Al and 6T-PEO layers, 6T was reduced by the migration of Na^+ toward the metal electrode (n-type doping). At the same time, 6T was oxidized at the interface with the PEDOT:PSS electrode by the migration

of Cl^- near the interface (p-type doping).These processes create a p-n junction. As a result, bistable switching can be induced in polymer systems.

1.2.4.3 Conformational Change

Resistive switching arises from electrically induced conformational changes in various molecules.[41-43] For example, devices with Rose Bengal molecules have shown resistive switching.[43] At least three states could be achieved in these devices when applied in high bias range, as shown in Figure 1.11. In the low voltage region, reverse electro-reduction of Rose Bengal facilitated the rearrangement of electrons in the backbone of the molecule, thus changing the molecule to a high conducting state. Under a large bias, forward-bias induced conformational change occurred in the two perpendicular planes of Rose Bengal molecule, hence the high conducting state was changed back to the low conducting state.

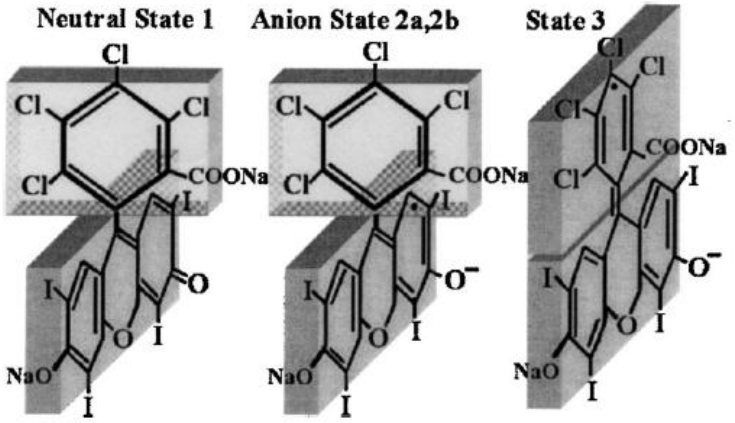

Figure 1.11 Chemical structure of Rose Bengal in its (a) neutral state, state 1, (b) reduced state without any conformational change, and (c) reduced state with conformational change, state 3. Reprinted with permission from ref 43.[43]

1.2.4.4 Space Charge and Traps

If the interface between electrodes and insulator (polymer) is Ohmic and the insulator is trap-free, then the carriers accumulate near the electrode to form a space charge. Repulsive force between such charges restricts the total number of charges which can be injected into the sample, and the resulting current is called space charge-limited current (SCLC). [44] Recently, a detailed paper reviewed the role of charges and traps in polymer devices.[45] Indeed, the electrical switching of some organic memory devices are associated with space charge and traps.[46] Majumdar et al.[46] showed that an ITO/ poly [3-(6-methoxyhexy)thiopene], (P6OMe)/Al device can be used to store data. The space charges were stored at the polymer-metal interface by application of a positive voltage pulse of 3 V for 20s to "write", and then the high conducting state was read out by a voltage pulse of 0.2V for 1min. They indicated that the retention time is more than 1 hour, however, the writing and reading processes were almost 20 seconds, which limited their practical application. Apart from measurement of conductance, capacitance was also demonstrated to exhibit two states for memory applications.[47]

1.2.4.5 Filamentary Conduction

When the ON state current is mainly localized in a small fraction of the device area, "filamentary conduction" occurs. [48, 49] There are two types of filament paths, one is associated with metallic bridges caused by the migration of electrodes,[50, 51] and the other is related to a carbon-rich filament component in

organic films.[52, 53] These mechanisms have often been used to explain memory behavior in various organic memory devices. Joo et al. [51] reported a memory device with the configuration of Cu/poly(3-hexylthiophene) (P3HT)/Al, in which Cu ions penetrated into the P3HT layer under forward bias, resulted in metallic filament formation. This work was supported by time of flight-secondary ion mass spectrometry (TOF-SIMS) analysis. Similar filaments can also be formed in PEDOT:PSS or other polymer composite materials in which Au clusters are dispersed.[54] In this case, the irreversibility of conductive path in organic layer showed a great potential use in write-once-read-many (WORM) memory.

In summary, a wide variety of polymer materials have been used in memory devices over the past five decades, and various mechanisms, models and calculations have been used to explain the operating principle. However, one serious problem that almost every review paper emphasizes is the reproducibility of the results. Variations in sample fabrication, test methods and environment all affect the device performance and reproducibility of the result. As a result, none of the currently reported organic memory devices have resulted in commercially viable technology.

1.2.5 Requirements of Memory Performance

Based on current performances of nonvolatile memory devices, such as Flash memory, there will be several requirements for designing and testing the next generation NVM:

1.2.5.1 Writing Process

The voltage used for writing process should not be very high, in order to show advantage compared to Flash memory which consumes ~12V or more. [55] Generally, write voltages should be in the range of a few mV to a few V. It will be good if the write pulse length is less than 20us, which is the programming speed of conventional Flash memory [56].

1.2.5.2 Reading Process

In order not to change the resistive during the reading process, the reading voltage should be much smaller than the writing voltage. Meanwhile, the reading current cannot be less than ~1uA, which makes integrated sense amplifiers providing a quick detection on the resistive change.

1.2.5.3 Erasing Process

Erasing process should switch the device from high conducing ON state back to low conducting OFF state, by application of reasonable erase voltage which has the value similar or less than the write voltage.

1.2.5.4 ON/OFF Ratio

This ratio determines whether the electronic circuit can distinguish the "ON" and "OFF" states. Even though an ON/OFF ratio of ~1.5 can be detected by careful circuit design, ON/OFF ratios >10 are necessary to compete with Flash memory. Moreover, high conducting ON state of NVM usually decreases after many Write/Erase cycles, which leads to a lower ON/OFF ratio with extensive

use. As a result, a large ON/OFF ratio in the initial device is essential for practical applications. Besides, because a large amount memory cells will show distributions of ON and OFF states, it is quite essential that these distributions are separated. A good example is show as Figure 1.12.

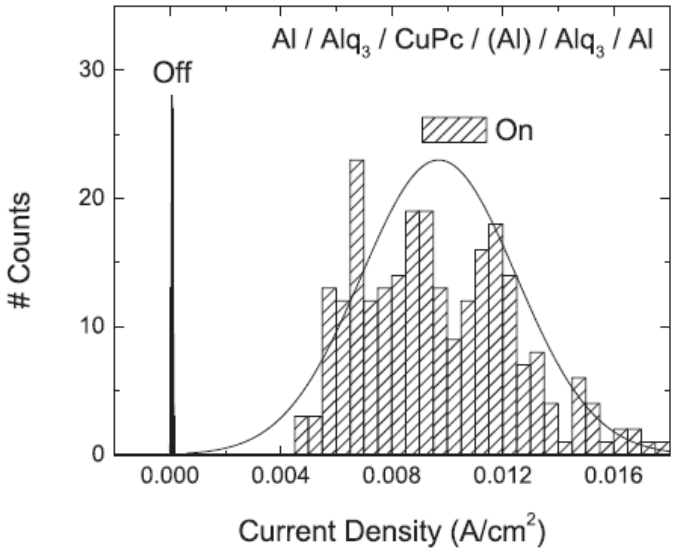

Figure 1.12 Histogram of ON and OFF state currents for 210 cycles of a device containing Al NPs. The ON/OFF ratio is over 100, and the mean ON state current density is 10 $mAcm^{-2}$. Reprinted with permission from ref 2.[2] Copyright © 2007 WILEY-VCH Verlag GmbH & Co. KGaA, Weinh

1.2.5.5 Cycle Life

Currently, Flash memories show a Write/Erase cycle life of ~10^4, based on the memory type. New NVMs should similar or better endurance to be practical commercially.

1.2.5.6 Retention Time

A retention time of >10 years is the industry standard for NVM, although different applications can tolerate shorter retention.[57] Usually, retention time

test contains constant readout pulses, sometimes at high temperature, like 85℃, to provide a thermal stressful condition. Archival data like social and legal records needs even longer storage time.

There is no current NVM technology which meets all the desirable performance specifications, but these requirements still provide goals for functional materials synthesis, NVM fabrication and evaluation.

1.3 Characterization of Memory Devices

With the development of novel compositions and structures, the understanding of the mechanisms behind the behavior of these electronic devices is becoming more essential.[6] Thus, characterization methods play a key role in performance evaluation of memory devices, as well as providing informative guidance on ways to optimize materials structure, fabrication process and device geometry. In this section, two general characterization methods are introduced: (1) Electronic Characterization and (2) Spectroscopic Characterization.

1.3.1 Electronic Characterization of Memory Devices

Electronic characterization such as current-voltage measurement cannot directly provide material structure information, but it is still the main characterization method to analyze the memory behavior.[7]Detailed discussion will be focus on current-voltage characterization and pulse characterization of memory device in this section.

1.3.1.1 Current-Voltage Characterization of Memory Device

The simplest method of measuring the current-voltage curves is to monitor the current at one electrode when a voltage is applied to the other one,[7] as shown in Figure 1.13 (a). However, ohmic potential error such as iR drop can often be observed using this two-wire configuration. To solve this problem, additional probes are added on the electrodes based on which electrode has the iR loss, shown as (b)-(d) in Figure 1.13.[7] For example, if iR loss is found in one electrode, a third probe is used to detect the actual voltage which is applied to the device and compensate for the iR loss. A four-wire configuration should be applied if both electrodes see this ohmic potential error.

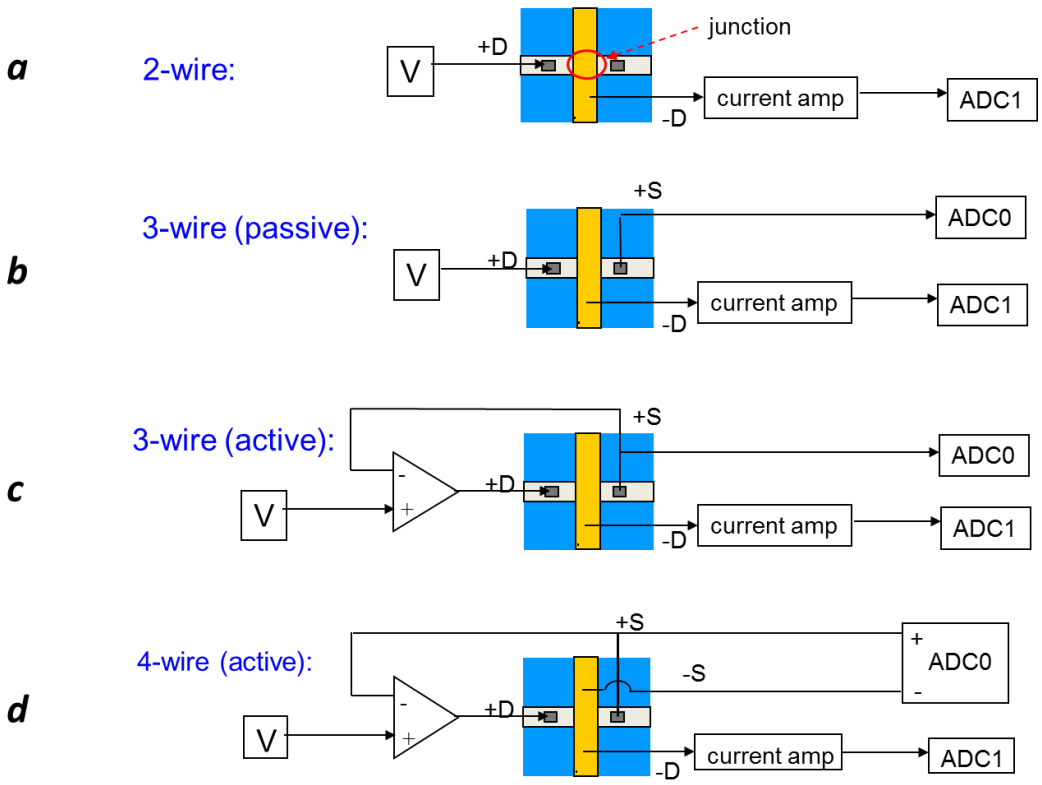

Figure 1.13 Wiring schematics for (a) two-, (b,c) three-, and (d) four-wire measurements of current–voltage (i-V) behavior of molecular junctions. V refers to the bias voltage from a digital-to-analog converter, and ADC1 stands for the analog-to-digital channel for current. ADC0 monitors voltage and has a differential input in the case of the four-wire arrangement. D and S denote drive and sense, respectively; the S leads correspond to high-impedance voltage monitors. Reprinted with permission from ref 7.[7]

1.3.1.2 Pulse Current-Voltage Characterization of Memory Device

As data storage devices, it is the most important to know how these memory devices behave with respect to W/E time, Read time, etc. Hence, pulse current-voltage characterization is widely used in memory device testing, not only to directly provide the measurement of switching behavior, but also to integrate with programing methods that might be used in commercial devices. A basic drawing as Figure 1.14 shows the commonly used read-write-read-erase-read pulse order. One should notice that the read pulse is usually smaller than write or erase pulse in order not to affect the ON or OFF state of the memory device.

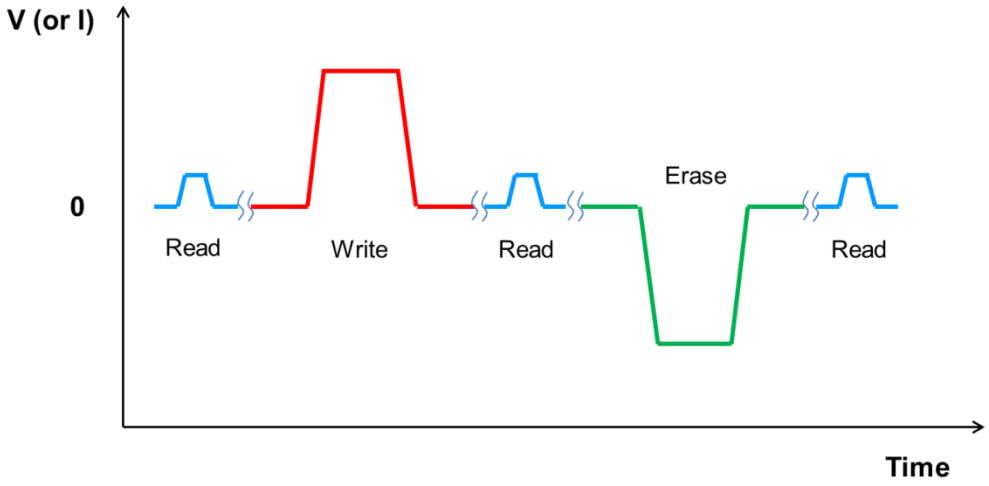

Figure 1.14 Memory pulse measurement program containing write, erase and read waveform: three pulses, four levels. Note that the intensity and duration are not the real scale.

1.3.2 Spectroscopic Characterization of Memory Devices

Among various detection tools, optical spectroscopic techniques show great potential for exploring the mechanisms in solid thin film devices, as they directly measure the functional material properties, such as oxidation states, structure changes and energy levels which are limited in current-voltage measurement. For example, Raman and FTIR spectroscopy are widely used in surface characterization. However, the signal is often too weak in Raman spectroscopy if the molecular layer contains no strong Raman scatterer, and the FTIR spectroscopy is limited by long measurement time and the need of IR transparent contacts and materials.[58-60] Compared to these two optical measurement techniques, ultraviolet–visible (UV-Vis) absorption spectroscopy is fast, sensitive and nondestructive. As a result, it becomes an excellent tool to investigate working memory devices, which directly provides information of electronic transitions in these molecular layers.[6]

1.3.2.1 Raman Spectroscopy

Even though the signal of Raman spectroscopy is not strong, it is still a useful test method to characterize the materials. Kumar et al. [16] reported a method which used Raman Spectroscopy to spatially resolve polaron generation in solid state polythiophene/viologen memory devices (Figure 1.15). The intensity shift in the Gate (G) region shown as Figure 1.15 (c) indicated the Poly(3,3’’’-didodecylquaterthiophene) (PQT) polaron generation when memory device was “set” by V_{SG} = +2V. And PQT polaron can be reduced back to its neutral form

reversibly with a bias of V_{SG} = -2V. However, each spectrum here took 10 seconds to reach an useful signal to noise ratio, much longer than the time of polaron generation and disappearance. If one wants to observe what happens in the writing or erasing process, a much faster technique is required.

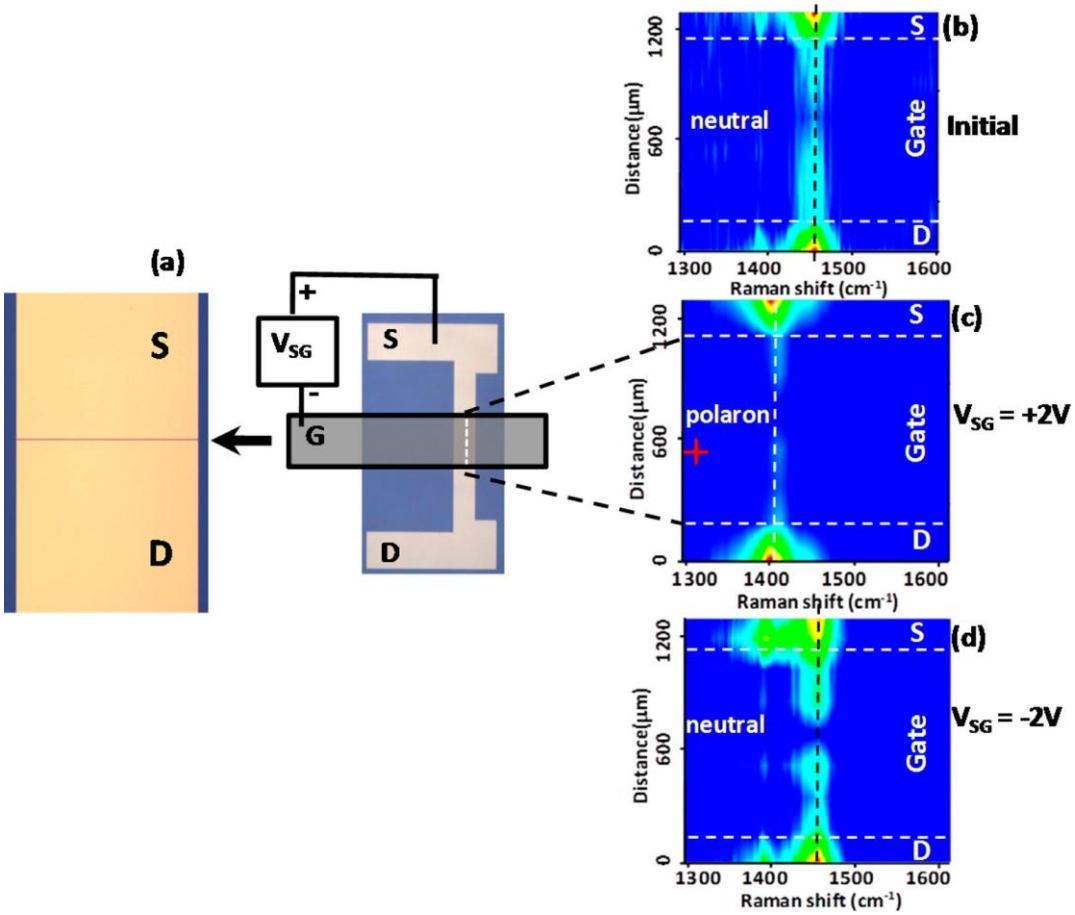

Figure 1.15 (a) Device schematic with bias polarities. The 1-μm channel is visible as a horizontal line in the left image. (b−d) Raman line scan image from three-terminal devices for the indicated bias values, composed of ten spectra acquired along the line between D and S. Each spectrum was acquired as a sum of fifteen 1-second spectra, and background was subtracted. Reprinted with permission from "Spatially Resolved Raman Spectroelectrochemistry of Solid-State Polythiophene/Viologen Memory Devices". Copyright (2012) American Chemical Society. [16]

1.3.2.2 UV-Vis Spectroscopy

Compared to the Raman spectroscopy, UV-Vis spectroscopy can probe structural changes of the device materials with much faster time resolution. A UV-Vis spectrometer generally monitors optical absorption in the 200nm to 700 nm spectral region. In this region of the electromagnetic spectrum, molecules containing n-electrons or π-electrons have the ability to absorb the energy in the form of ultraviolet or visible light, making these electrons excite to higher anti-bonding orbitals. [61]

(1) Electronic transitions in UV-Vis spectrum

As shown in Figure 1.16, four kinds of transitions are possible. However, the energies required to induce σ→σ* and n→σ* are relatively large, with most absorption peaks showing below 200 nm. As a result, commonly studied features in ultraviolet–visible region involve transitions of π→π* and n→π*.[61] Since π electrons are quite common in organic compounds, UV-Vis spectroscopy can be used as a very effective quantitative characterization method in organic thin films.[6] However, UV-Vis spectra have much broader features compared to FTIR or Raman spectra, which makes it difficult to provide detailed structural information.

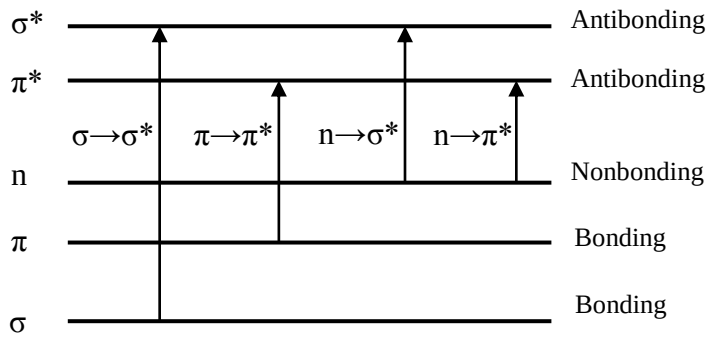

Figure 1.16 Electronic molecular energy levels

(2) Beer's Law

Traditional UV-Vis spectroscopy is based on the measurement of the absorbance A or transmittance T of solutions, as represented by the Beer's Law[61]:

$$A = -\log T = \log\frac{I_0}{I} = \epsilon bc$$

where I_0 and I are intensities of incident and emergent light, respectively. ϵ denotes molar absorptivity. b is path length, and c is concentration of organic compound.

But for thin film characterization, the absorbance of the molecular layer is quite small since the film thickness is usually 2-50 nm. As a consequence, I_0 and I are almost identical, which lead large photometric error in measurement. Hence, Beer's Law should be modified, as represented by the modified Beer's Law[6, 7]:

$$\Delta A(\lambda) = \sum_{i=1}^{i=n} \epsilon(\lambda)_i b \Delta c_i = \sum_{i=1}^{i=n} \epsilon(\lambda)_i \Delta\Gamma_i$$

where $\epsilon(\lambda)_i$ denotes molar absorptivity at wavelength λ of species i, Δc_i and $\Delta\Gamma_i$ are the changes in concentration and surface concentration, respectively. n is the

number of species in thin layer. This equation gives a rough estimation of absorbance changes in thin layers.

(3) In-situ UV-Vis spectroscopy in working devices

To investigate changes in a thin molecular layer, a spectrum without potential is first recorded as a reference. Then absorbance changes (ΔA) relative to the reference are generated after voltage pulses are applied.[6] Normally, current-voltage curves are also measured after each pulse to calculate the capacitance changes.

Because the absorbance change (ΔA) is usually small, and it also changes fast, the spectrometer must be sensitive and have good time resolution. An estimation was made to show absorbance changes (ΔA) is 1×10^{-3} for complete reduction of polymeric molecular layer, which is higher than the detection limit of UV-Vis spectrometer, making it practical to characterize thin film.[6] Also, as a fast and effective technique, UV-Vis spectrometer using CCD detectors are capable of acquiring 200 spectra per second.

For the illustration convenience, the notation of a molecule device means each layer from bottom to top. For example, C/NAB/SiO_2/Pt describes a device with a nitroazobenzene (NAB) film on e-beam carbon layer deposited on silicon wafer, and SiO2 and Pt layers deposited on the surface of NAB.

Figure 1.17 shows an example of in-situ analysis of a NAB thin layer in a solid state C/NAB/SiO_2/Pt geometry by UV-Vis absorption.[6] These clear and evident changes in spectra indicated the variations of structure of molecule in thin

film with the application of positive or negative bias. It also confirmed that NAB was reduced to NAB anion.[7]

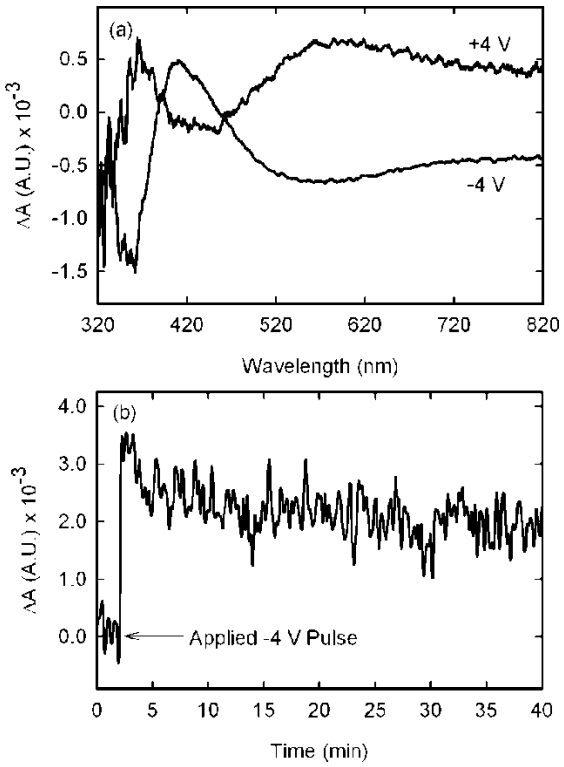

Figure 1.17 (a) ΔA of NAB/SiO2 after a -4 V pulse and subsequent +4 V pulse. ΔA of the two voltage pulses are nearly symmetric about zero ΔA; (b) ΔA of a NAB/SiO_2 at 410 nm before and after a -4 V pulse. The increase in ΔA at t=2 min was caused by the application of the -4 V pulse. Reprinted with permission from "In-Situ Optical Absorbance Spectroscopy of Molecular Layers in Carbon Based Molecular Electronic Devices". Copyright (2008) American Chemical Society.[6]

1.4 Research Objective

The overall objective of the research presented in this thesis is to establish fast and simultaneous optical spectroscopy coupled with electronic characterization to monitor the polymer redox process in a working memory device. In addition, optical and electronic measurements were performed simultaneously to explore how fast the polarons were formed and propagated though the device, as a complement to the previous research.[16] Previous

research has shown that poly(3,3‴-didodecylquaterthiophene) (PQT) polarons generated and propagated in the working memory device, but due to the slow speed of Raman spectroscopy, spectra were obtained after constant voltage was applied for 30s (not the real pulse measurement).[16] Another objective was exploration of the effect of solvation by polar molecules on memory device operation, as well as to find a method to improve the memory switching speed.

In the previous research, PEO matrix containing viologen was drop coated on the PQT layer, which led the thickness varied from chip to chip. In the work reported in this thesis, an alternative method was explored to replace drop coating method, to yield more reproducible devices and more closely approximate fabrication techniques used by the microelectronic industry.

Chapter 2 describes the fabrication procedure of the Au/P3HT/PEO-EV$(ClO_4)_2$/C/Au three terminal memory devices studied. Four devices are made on each 18×13 mm quartz substrate with TFT structure. A new fabrication method is used to form uniform electrolyte layer with controlled thickness of ~550nm between the bottom and top electrodes. Characterization using optical microscopy, profilometry, AFM and SEM is presented.

Chapter 3 describes the optical and electronic properties of P3HT memory device using in-situ optical detection coupled with three different electronic measurement systems. Multivariate Curve Resolution (MCR) analysis of the absorption spectra is presented. The characterizations of memory device in different time scale are examined by the in-situ detection method. Furthermore, an effect of local atmosphere on memory switching speed and retention is also

identified. A memory switching mechanism is proposed in the last part and confirmed using a simplified dual pulse detection method.

Finally, the thesis ends with a brief summary of all the experiment done, and a list of several ways which can improve the memory performance in the future.

CHAPTER 2

FABRICATION AND OPTICAL MONITORING OF POLYTHIOPHENE NONVOLATILE MEMORY DEVICES

2.1 Introduction

The main objective of this thesis is to in-situ characterize nonvolatile memory devices. In order to achieve this, memory devices should be transparent or semi-transparent, and the optical spectroscopy must provide fast detection. In this chapter, detailed descriptions are focused on semi-transparent memory device fabrication and the optical monitoring system.

In previous work on fabrication of transparent devices, the McCreery group demonstrated that vapor deposited thin metal films can provide ~50% transparency for UV-Vis light, and still had enough conductivity to be used as electrodes.[5, 6] Unlike the two terminal memory devices introduced in Chapter 1, memory devices discussed in this thesis have a three-terminal structure similar to thin film transistor (TFT), but use a totally different operation mechanism. Figure 2.1 shows the geometry of the memory device investigated in this thesis. This kind of device has some of the features of its original counterpart, metal–oxide–semiconductor field-effect transistor (MOSFET), which also has three contacts: Source (S), Drain (D) and Gate (G). The channel length between the Source and Drain electrodes is 20μm; the channel width, which means the width of Source and Drain electrodes, is 500μm. Thus the resistive changing area is 1×10^4 μm^2.

The memory operating principle is based on resistive switching of poly(3-hexylthiophene) (P3HT): The Source-Gate circuit is used to generate or reduce polarons in P3HT layer in this 1×10^4 μm^2 area, and the Source-Drain circuit is used to detect the ON (high conductance polaron form) or OFF (low conductance neutral form) of the device. This TFT structure has three benefits: (1) Memory switching process and readout process are separated, and readout voltage V_{SD} is much smaller than switching voltage V_{SG}, as a result, reading process does not affect the memory ON/OFF states. (2) Since the devices are made on an optically transparent quartz wafer, the optical detection system can easily probe the switching process in the channel without major intensity loss, since light only transmits through very thin Au and C layers. Moreover, Source and Drain electrodes can be made relatively thick to block the light, thus the observed optical signal change is only due to the polymer switching within the channel. (3) Fabrication methods are similar to MOSFET and "flash" memory, which may assist integration with conventional TFT fabrication processing.

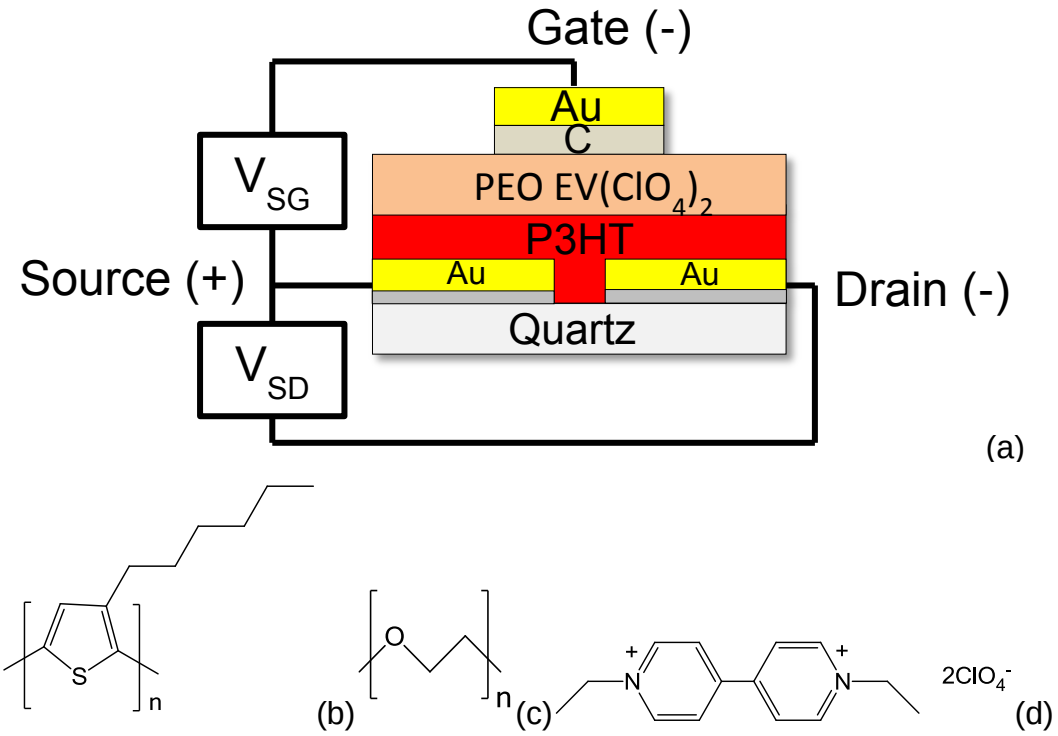

Figure 2.1 Schematic of memory devices under investigation (a) three terminal device with Gate, Drain and Source geometries. Chemical structures of (b) neutral form of P3HT (c) PEO and (d) ethyl viologen diperchlorate. Layer dimensions are not shown to scale.

2.2 Device Fabrication

The fabrication procedure of polythiophene nonvolatile memory devices has four major steps: (1) fabrication of bottom electrodes; (2) polythiophene layer preparation; (3) electrolyte layer preparation; (4) deposition of top contact. Figure 2.2 schematically shows the fabrication procedure. Detailed descriptions can be found in the following sections.

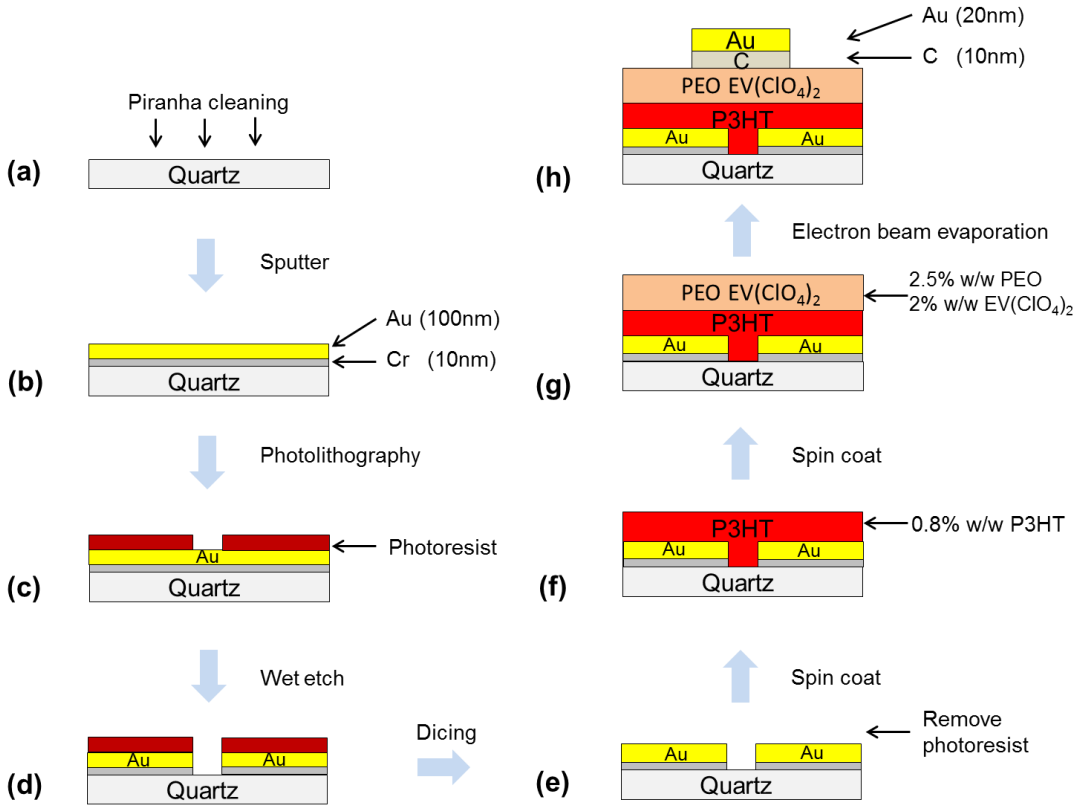

Figure 2.2 Process flow chart for the fabrication of Polythiophene Nonvolatile Memory Devices. (a) 4 inch quartz wafer was cleaned using hot Piranha for 10 minutes. (b) A ~100nm Au layer was deposited as bottom electrodes using sputtering deposition, followed by a ~10nm adhesion layer of Cr. (c) Photoresist HPR 504 was spin-coated and patterned through optical photomask using standard photolithography. Pattern was formed after development. (d) Au and Cr layers were etched using KI/I_2 Au etchant for 36s and Cr etchant for 5s respectively, to generate bottom Source and Drain contacts. Photoresist HPR 504 was spin-coated again to protect wafer surface from contamination during dicing. (e) Quartz wafer was cut into 18mm × 13mm substrates using dicing saw. Then substrates were cleaned ultrasonically in acetone, isopropanol and ultrapure water for 5 mins each to remove photoresist and other contaminants. (f) P3HT 0.8 wt % solution in 1,2-dichlorobenzene was spin-coated at 1000 rpm for 120 seconds. Then the spin coated substrates were dried in a vacuum oven at ~10^{-2} Torr, 100 ℃ for 5 minutes. (g) The electrolyte solution was prepared by adding 0.04g ethyl viologen diperchlorate and 0.05g poly(ethylene oxide) in acetonitrile. Then PEO solution was spin-coated at 1000rpm for 60s. (h) The memory device was completed by electron beam deposition of C (10nm) and Au (20nm) at top contacts through a shadow mask at pressure of < 4×10^{-6} Torr.

2.2.1 Fabrication of Bottom Electrodes

All the procedures described here were carried out in the nanoFAB of University of Alberta and the cleanroom of the National Institute for Nanotechnology.

2.2.1.1 Wafer Cleaning

A 4-inch double sides polished quartz wafer (0.5 mm thick, Technical Glass Products) was used as a substrate. In order to remove organic or metallic contaminants from the surface, this wafer was first placed in a Teflon carrier boat, then submerged into hot Piranha solution (mixture of 96% Sulfuric Acid and 30% Hydrogen Peroxide, 3:1 v/v) for 10 minutes, then rinsed in the automatic rinser with large amount of deionized water, and finally dried in a spin rinse drier in nitrogen flow. (Note: Hot Piranha solution is a violent oxidizer and may is very hazardous, it is essential to put on chemical apron, chemical resistant gloves and face shield before handling the chemicals, cleaning process must be done in fume hood)

2.2.1.2 Deposition of Cr/Au

The quartz wafer was loaded into the Magnetron Sputtering System "Floyd" (Kurt J. Lesker) at nanoFAB. Cr layer was first deposited at 11.5nm/min for 52 seconds, followed with Au layer deposition at 14.2nm/min for 422.5 seconds, resulting a 10nm Cr layer and 100nm Au layer. All the depositions were done within a controlled 7 mTorr Ar atmosphere.

The 10 nm Cr and 100 nm Au layers not only provide good conductivity which is necessary for bottom electrodes, but they also limit light transmission during optical characterization. Figure 2.3 shows the intensity of transmitted light through Cr and Au layers on quartz wafer, with a maximum value near 500nm of only 0.13%.

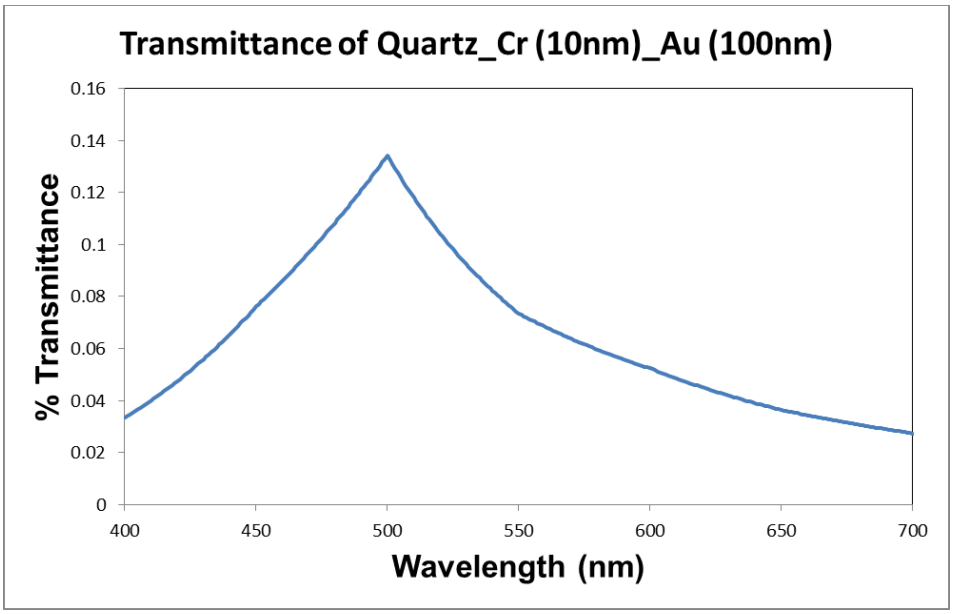

Figure 2.3 Transmittance Spectra of 10nm Cr and 100nm Au layers deposited on quartz wafer, simulated by Filmstar. The overall transmittance from 400nm to 700nm is less than 0.15%.

2.2.1.3 Photolithography

5ml photoresist HPR504 (MicroChem) was spin-coated on the Au layer at a speed of 200rpm for 10 seconds using a manual spinner. Then the spin speed went to 4000rpm for 40 seconds, followed by a spin speed of 3000rpm for 10 seconds. After removing backside residue photoresist, the wafer was transferred onto a preheated hotplate at 115℃ for 90 seconds in air. This photoresist layer was left in air to rehydrate for ~15 minutes before UV light exposure. The

Photomask and the wafer were loaded onto the Quintel Q-4000 mask aligner, then vacuum contact was engaged between wafer and mask. After 4.2s UV exposure, the wafer was immersed into a mixture of MF-26A developer (Rohm & Haas electronic Materials) and deionized water (1:2) for approximately 40 seconds until photoresist was washed away in exposed areas. The wafer was then rinsed with a large amount of deionized water to stop further development, and dried by nitrogen stream. Small features like channels were inspected under the microscope to identify whether further development was needed.

Following lithography, bottom electrodes were fabricated on wet etching desk. (Note: Because metal etchants are highly toxic and corrosive, chemical apron, chemical resistant gloves and face shield are needed before handling these chemicals.) Roughly 80mL KI/I_2 Au etchant (Sigma-Aldrich, etching rate: 28 Å /s) was first poured into a Teflon wafer tray. The Quartz wafer with Cr and Au deposited layers was immersed into the Au etchant for 36 seconds with slight shaking, then rinsed with deionized water, and blown dry with nitrogen. Optical Microscopy inspection revealed if further etching was needed. After cleaning the wafer tray, the same amount of Cr etchant (Sigma-Aldrich, etching rate: 40 Å /s) was used to etch the 10nm Cr layer. Enough etching time (more than 2.5 seconds) was needed until visible color change occurred. The wafer was rinsed and dried, and inspected using optical microscopy again. Photoresist HPR504 was spin coated on the wafer surface to protect the surface from particles or contamination during dicing. Finally, the 4 inch wafer was diced into 18×13 mm substrates using

quartz dicing saw (Diamond Touch). The completed substrate is shown as Figure 2.4.

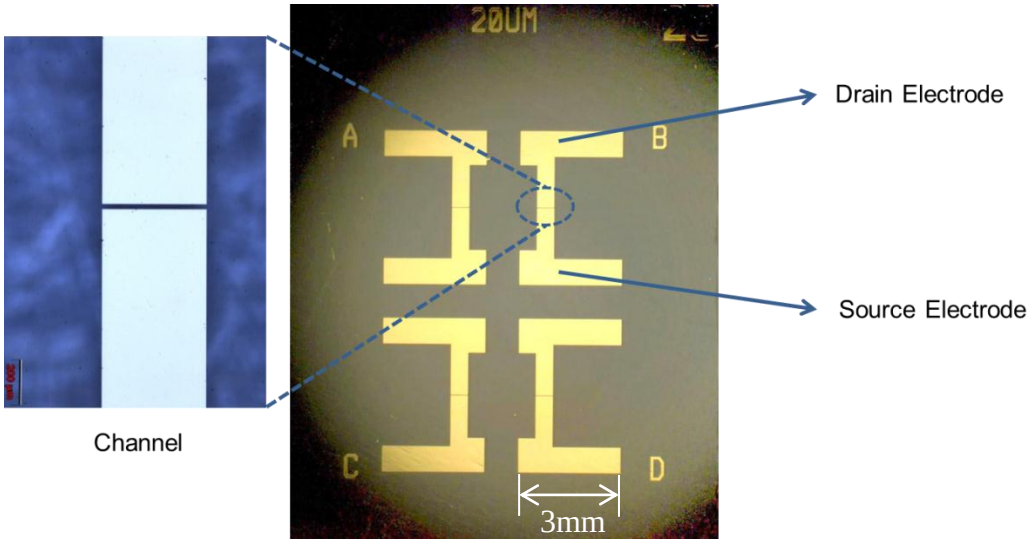

Figure 2.4 Top view of completed bottom electrodes using microscope. 4 devices are on each chip.

2.2.2 Polythiophene Layer Preparation

16mg of P3HT (Regioregular Sepiolid P100, Made by BASF in cooperation with Rieke Metals) was put into a scintillation vial, then 1,2-dichlorobenzene (DCB, HPLC grade, Sigma-Aldrich) was added to 2g total weight, resulting a 0.8% w/w solution of P3HT in DCB. The vial was sealed using Teflon septum protected cap after purging with Argon. Then the solution was sonicated in an 80℃ water bath until P3HT was dissolved.

In order to strip the protective photoresist, the diced substrates were sonicated in acetone (HPLC grade, Fisher), isopropanol (HPLC grade, Fisher) and deionized water (Millipore) respectively, each for 5 minutes. After drying in a

nitrogen flow, the dies were further cleaned in nanoFAB using oxygen plasma ash at 400mTorr, 100% flow and 75W power for 5 minutes. Small features were examined using microscope to detect visible damage.

The spin coater (Specialty Coating System) was programmed as listed in Table 2-1. 4 drops of P3HT solution in DCB was spin coated on each clean die using glass pipette. Then residual P3HT solution on the backside of the quartz die was cleaned using cleanroom tissue. After spin coating, the substrates were moved into a preheated vacuum oven at 100℃ for 10 minutes. The top view of substrate with spin coated P3HT is shown as Figure 2.5.

Table 2-1 Spin coater program for P3HT layer deposition

	Ramp Time (s)	Spin Speed (rpm)	Spin Time (s)
1	1	1000	120
2	5	3000	20
3	5	0	0

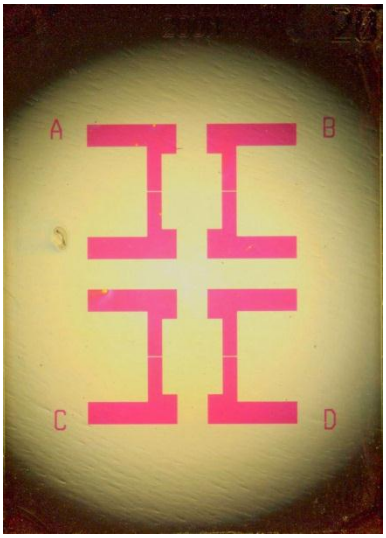

Figure 2.5 Top view of substrates with spin coated P3HT layer using microscope.

An AFM scratching method was used to determine the thickness of the P3HT layer, as described before.[62] It provides a direct technique to determine the thickness of the organic film, which is critical for understanding electronic behavior. In this measurement, AFM tip was forced to scratch the P3HT film which was spin coated on the substrate in contact mode. The force was adjusted not to scratch the quartz surface, but large enough to remove the P3HT layer. Then the "trench" area and its surroundings were imaged using AFM tapping mode. The thickness of the P3HT layer was determined statistically as the difference in height between the original film and the bottom of the "scratch".

Figure 2.6(a) shows the $5\times5\mu m^2$ AFM image of the spin coated P3HT layer in tapping mode with a scan rate of 2Hz, using DI3100 atomic force microscope (Digital Instruments) and silicon AFM tip (NSC15/AIBS, MikroMasch) with a resonant frequency of ~325kHz. The statistical surface rms roughness of the whole area (Ra) was 1.8nm. Then the contact mode was carried out in the middle $1\times1\mu m^2$ area, using the set point voltage of 0.8V and scan rate of 1Hz. Finally, AFM tapping mode was used again, shown as Figure 2.6(b). A rectangular box contained both shallow and regular area was selected using software "Nanoscope v 6.13", then the data was exported and Gaussian fitted, showed a statistical P3HT layer thickness of 26.2nm.

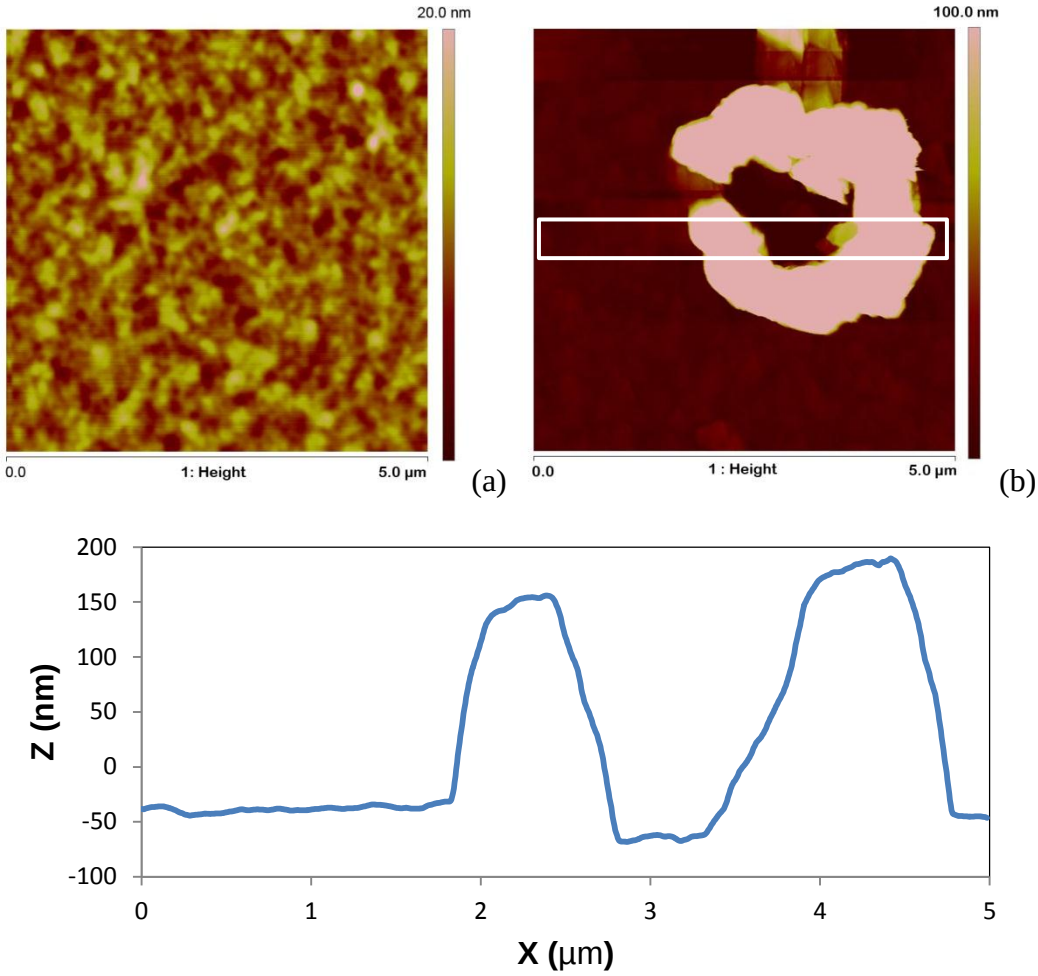

Figure 2.6 AFM images ($5\times5\mu m^2$) of spin-coated P3HT layer using tapping mode and contact mode respectively. (a) Rms roughness of P3HT layer (Ra) is 1.8nm. (b) Thickness of P3HT layer is 26.2nm using Gaussian Fits. (c) Statistical depth profile for the image in (b).

2.2.3 Electrolyte Layer Preparation

As reported previously, ethyl viologen diperchlorate ($EV(ClO_4)_2$) was combined with poly(ethylene oxide) (PEO) to form the second organic layer of the memory device. [16] In the original fabrication method, the $EV(ClO_4)_2$ and PEO in acetonitrile solution could not be spin coated on the P3HT layer due to the strong hydrophobic property of P3HT. Instead, the second layer was actually drop cast and dried on the polythiophene layer, forming the valley shape shown schematically in Figure 2.7. The thickness of the center region was heavily dependent on the drop volume and process time. Moreover, the thicker edge of the dried drop made the top contact deposition nonuniform.

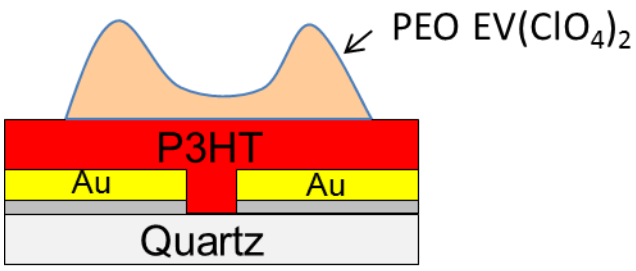

Figure 2.7 Drop coated ethyl viologen diperchlorate separated in polyethylene oxide matrix, with a valley shape in cross section.

For the current work, the method was modified to spin coat PEO-EV on the hydrophobic P3HT layer with much better uniformity and controlled thickness, even though the $EV(ClO_4)_2$ and PEO in acetonitrile solution was hydrophilic and P3HT layer is hydrophobic. The approach was to increase the viscosity of PEO-EV solution by controlling the polymerization degree and concentration of PEO in

acetonitrile. Thus, the solution could spread more evenly on the P3HT layer. The effect of different spin speeds on resulting layer thickness was also studied.

In order to increase the viscosity of PEO solution, 300K Da PEO was selected instead of 100K Da PEO used previously. Three concentrations of PEO in acetonitrile were prepared as shown in

Table 2-2. Proportion of $EV(ClO_4)_2$ to PEO was kept as 0.8 in each case, in order to make constant concentration of $EV(ClO_4)_2$ in PEO layer after the acetonitrile evaporated. $EV(ClO_4)_2$ (Sigma-Aldrich) was first added into acetonitrile in a cleaned scintillation vial, then PEO (300K Da, Sigma-Aldrich) was added gradually while the vial was sonicated in a water bath, in order to avoid PEO lumps. (Note: PEO lumps in acetonitrile solution were very difficult to dissolve.) The solution was further sonicated for 10 minutes until PEO was uniformly dissolved. Then the solution was spin coated onto the P3HT layer in 1000rpm, 2000rpm and 4000rpm for 60 seconds each. Thickness and rms roughness of spin coated PEO layer were measured by a profilometer (Alpha Step IQ) in nanoFAB (Figure 2.8). Optical examination was carried using an optical microscope (Olympus SZ61) and INFINITY CAPTURE Application v 5.0.4 (Figure 2.9).

Table 2-2 Formula of PEO- $EV(ClO_4)_2$ solution

Concentration of PEO	EV(ClO4)2	PEO (300kDa)	Acetonitrile
1% PEO	0.016g	0.02g	2g
2.5% PEO	0.04g	0.05g	2g
5% PEO	0.08g	0.1g	2g

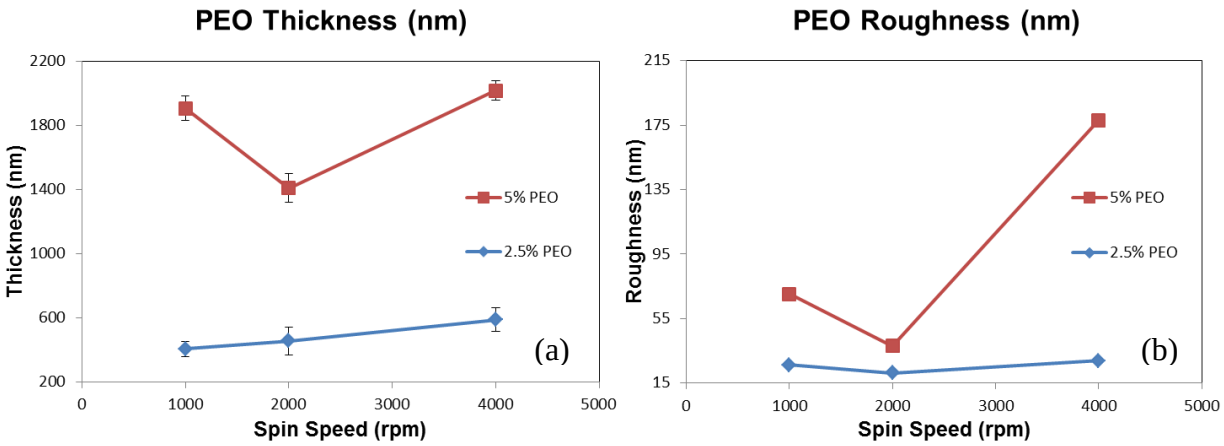

Figure 2.8 Effect of concentration and spin speed on PEO layer thickness and rms roughness. Data were measured by profilometer. Error bar is the thickness derivation.

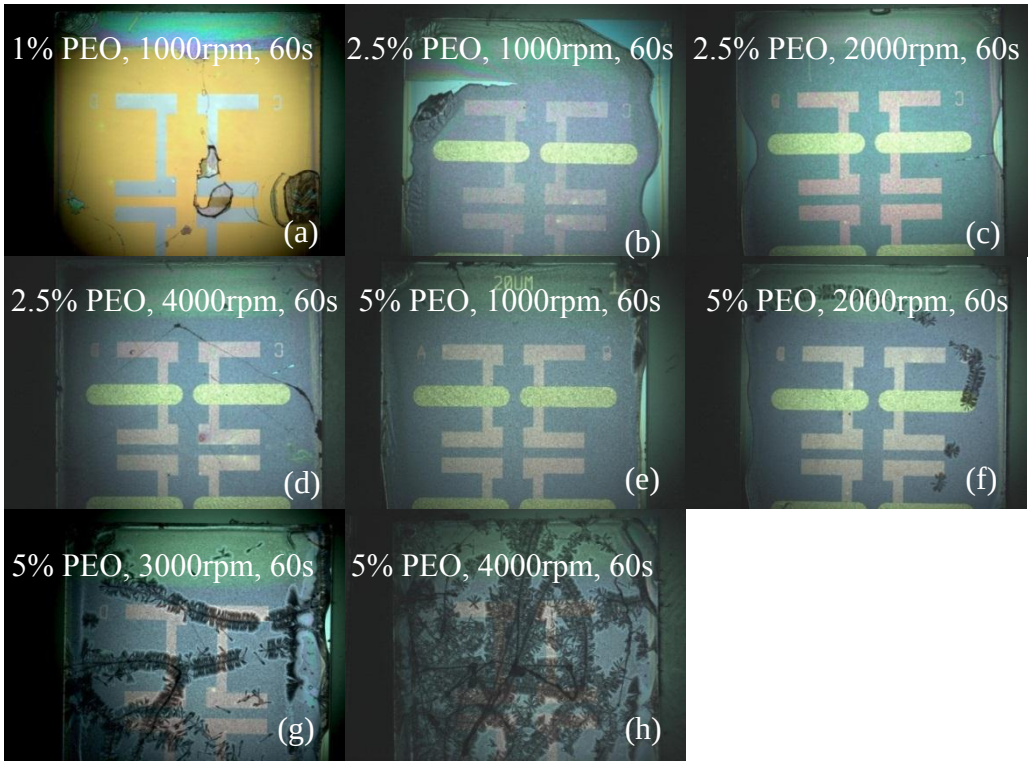

Figure 2.9 Spin coated PEO layer using the indicated conditions on P3HT surface. (a)1% PEO did not stick to P3HT layer because of the low viscosity. (f) Crystal patterns formed at high spin speed and high concentration of PEO, and resulted in much higher roughness.

1% PEO solution could not spin coated on P3HT layer due to its low viscosity caused by low PEO concentration, shown as Figure 2.9 (a). But this result also confirms that viscosity played a key role in formation of PEO layers by spin coating . By changing the concentration of PEO solution from 2.5% to 5%, the thickness changed from ~500nm to ~2000nm (Figure 2.8 (a)). Spin speed change did not have a large effect on the PEO layer thickness when using constant PEO concentration. For example, PEO layer thickness using 2.5% concentration only changed from 407±47nm to 590±74nm when spin speed changed from 1000rpm to 4000rpm. The phenomenon that layer thickness increased with the increasing spin speed implies that the PEO-EV$(ClO_4)_2$ solution behaves as a Non-

Newtonian fluid, which accumulates on the dies at high spin speed instead of spinning away. This also led a higher thickness deviation as shown in Figure 2.8 (a). When 5% PEO was spin coated at different speeds, crystal patterns were observed for 2000 rpm and above (Figure 2.9 (f)). As spin speed increased, more crystals were generated, resulting a dramatically increased rms roughness(Figure 2.8 (b)).

In order to obtain uniform and well defined PEO layer, the devices in this thesis were made using the a 2.5% PEO concentration and 1000rpm spin speed. The top view of device with spin coated PEO layer is shown as Figure 2.10. SEM images taken with a Hitachi S4800 SEM also shows the uniformity and thickness of spin coated PEO layer. Completed memory devices were cleaved and sputtered with a thin Cr layer to reduce electron charging effects and increase sample conductance. Figure 2.11 (a) and (b) both showed the 100nm Au and 550nm PEO layers on quartz substrates on different scales. The thickness of PEO layer is 550±20 nm, which is approximately similar with the data measured using profilometer (407±47nm). The Cr and P3HT layers were not resolved in the SEM images. The top view of PEO layer imaged with a 45° angle is shown as Figure 2.11 (c).

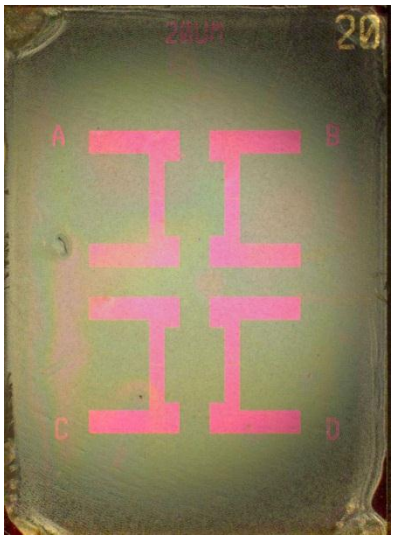

Figure 2.10 Top view of substrates with spin coated PEO layer using microscope.

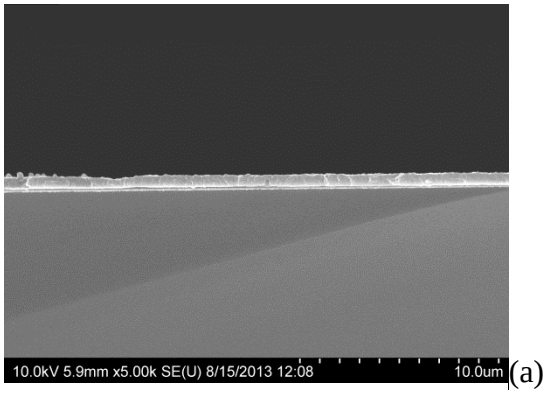

(a)

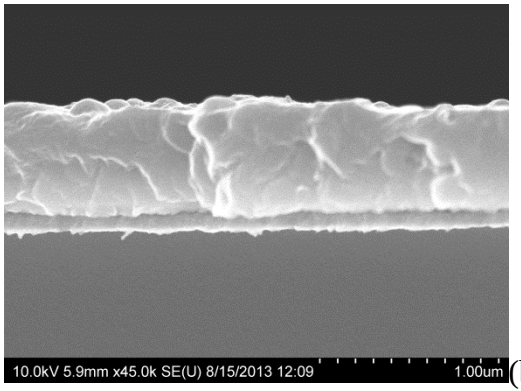

(b)

(c)

Figure 2.11 SEM images of spin coated PEO-EV$(ClO_4)_2$ layers. (a) PEO-EV$(ClO_4)_2$ solution formed uniform solid layer after spin coating with thickness of 550±20 nm. (b) A zoom out image shows 550nm PEO-EV$(ClO_4)_2$ on 100nm Au layer. (c) Top view of spin coated PEO-EV$(ClO_4)_2$ layer.

2.2.4 Deposition of Top Contacts

After PEO-EV(ClO_4)$_2$ layers were spin coated, the dies were transferred into a mask holder, followed by a mount spacer, a shadow mask and a top plate. Then the mask holder was loaded into a PVD 75 electron beam evaporator (Kurt J. Lesker). The e-beam chamber was pumped for at least 3 hours to reach a base pressure of ~3.0 $\times$ 10^{-6} Torr. 10nm C and 20nm Au were deposited onto the top of the dies through a shadow mask, in order to form the Gate electrodes. A Quartz Crystal Microbalance (QCM) was used to monitor the thickness and deposition rate of the top electrodes. (Note: The QCM crystal was replaced if the remaining crystal life is below 50%.) All the depositions here were carried in a range of 3.0 - 6.0 $\times$ 10^{-6} Torr.

Carbon was first deposited at ~0.05 Å/s for the first 1 nm and ~0.2 Å/s for another 9 nm, resulting in an amorphous, mostly sp^2 hybridized C layer. [63]. Au was deposited at ~0.1 Å/s for the first 2 nm and ~0.4 Å/s for the remaining 28 nm. It should be noticed that the deposition rate of C was rather unstable requiring careful adjustments of deposition power. The completed devices are shown in Figure 2.12.

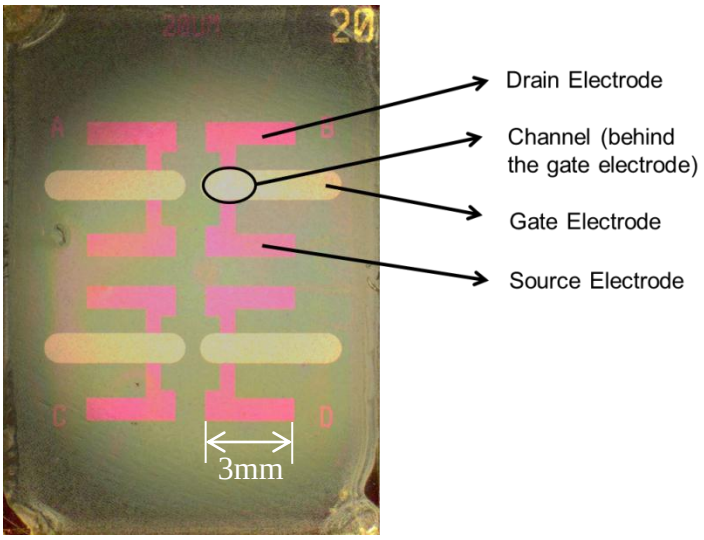

Figure 2.12 Top view of completed devices with top contacts using microscope.

Figure 2.13 shows the simulation of the transmission light intensity through 10nm C and 20nm Au layers, the ~20 – 30% transmittance is large enough for optical detection in 400nm to 700nm range.

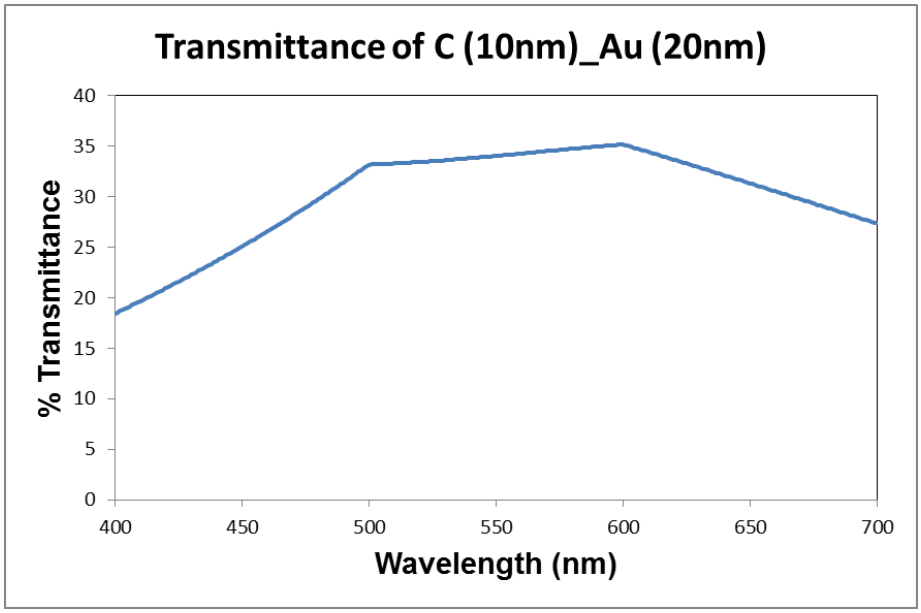

Figure 2.13 Transmittance Spectra of 10nm C and 20nm Au layers, simulated by Filmstar. The overall transmittance from 400nm to 700nm is ~20 - 35%.

Figure 2.14 shows the real measurement of bottom (10nm Cr and 100nm Au) and top (10nm C and 20nm Au) electrodes. The large noise signal from 400nm to 450nm is due to the limitation of light source, since quartz halogen bulb used as light source had very limited illumination at that range. The experimental values are similar to the simulated spectra, but slightly higher. The thick bottom electrode blocked most of the light, however, the top electrode still can provide an overall transmittance of ~30-40%.

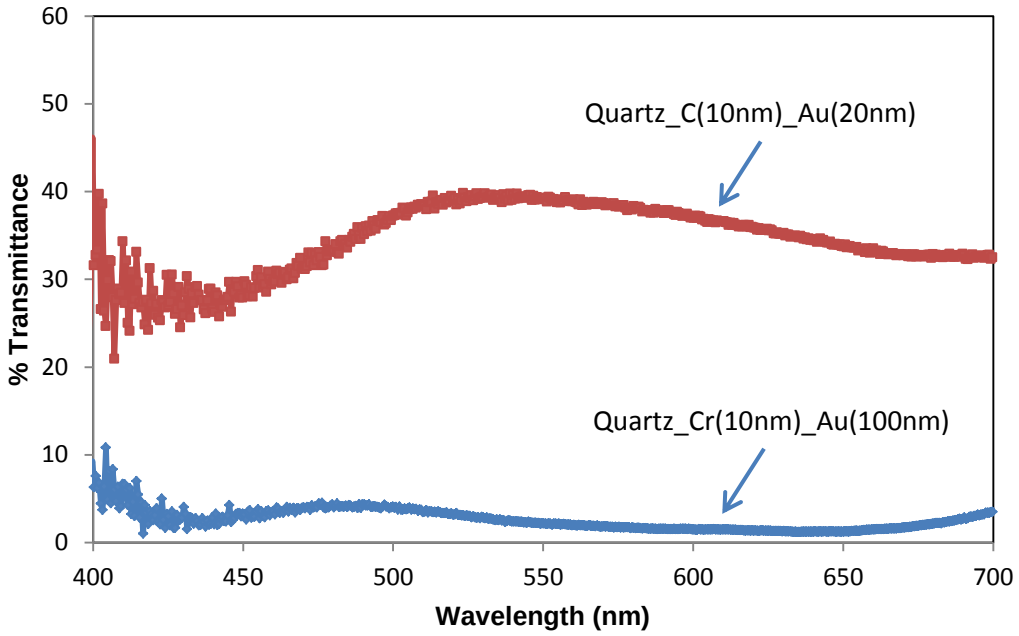

Figure 2.14 Transmittance of bottom and top electrodes using apparatus demonstrated in 2.3.2 with exposure time of 0.1s. The overall transmittance from 450nm to 700nm of bottom and top electrodes were ~1.3-4% and ~30-40% respectively.

2.3 In-situ Optical Monitoring System

In order to monitor changes in the P3HT active layer, three different in-situ optical arrangement were used with the same objective: to monitor changes in the P3HT layer absorbance when a voltage bias was applied. As noted in the previous chapter, each configuration has its own advantages: (1) Setup used for solution experiment: Optical detection system was used to monitor solid thin film in solution to provide spectral information about P3HT. (2) For measuring repetitive write/read/erase/read memory cycles: Optical detection system coupled with Keithley 2602A dual channel source measure unit identified the feasibility of independent optical detection of operating polythiophene memory devices, and provided direct correlation of spectroscopic and electronic measurements. (3) Setup used for measuring memory characteristics: Optical system coupled with National Instruments 6110DAQ board and two SRS 570 current amplifiers (Stanford Research Systems) acquire data faster than the Keithley system, which could be used to distinguish fast features during fast writing or erasing process.

2.3.1 Apparatus used for solution experiment

Special samples were made according to similar fabrication process indicated in 2.2. Four pieces of 18mm×13mm quartz substrates were sonicated in acetone (HPLC grade, Fisher), isopropanol (HPLC grade, Fisher) and deionized water (Millipore), each for 5 minutes. After drying with nitrogen gas, the dies were again cleaned in nanoFAB using oxygen plasma ash at 400mTorr, 100% flow and 75W power for 5 minutes. Then 10nm C and 20nm Au were deposited

using PVD 75 electron beam evaporator (Kurt J. Lesker) with speeds of ~0.2 Å/s and ~0.4 Å/s respectively at 3.0 - 6.0 $\times$ 10^{-6} Torr. One of four samples were used as reference sample, the remaining three samples were further spin coated with 0.8% w/w P3HT solution in DCB and dried in preheated vacuum oven for 10mins at 100 ℃.

Figure 2.15 shows detailed system configuration. Light from a 100W High Intensity Quartz Tungsten Halogen lamp (Model: Th3-100, Sciencetech Inc.) passed into a sample chamber (Sciencetech Inc.) where it passed through the sample which was inside an optical glass cell (Starna Cells Inc.) with special designed sample holder. The transmitted light, then entered a spectrograph (Shamrock sr-303i, Andor Technology), and was detected by a CCD detector (Newton, Andor Technology).

Before examining a P3HT sample, a reference sample was immersed into 0.1M TBHFP acetonitrile solution and used to record a reference spectrum. After that, the P3HT sample was connected to potentiostat (EC epsilon, Bioanalytical Systems, Inc.) as working electrode, and immersed into acetonitrile solution. A Pt wire and a non-aqueous $Ag/AgNO_3$ electrode were used as counter and reference electrodes, respectively. Once a particular voltage was applied to the P3HT sample, spectra were recorded using "Andor SOLIS" software.

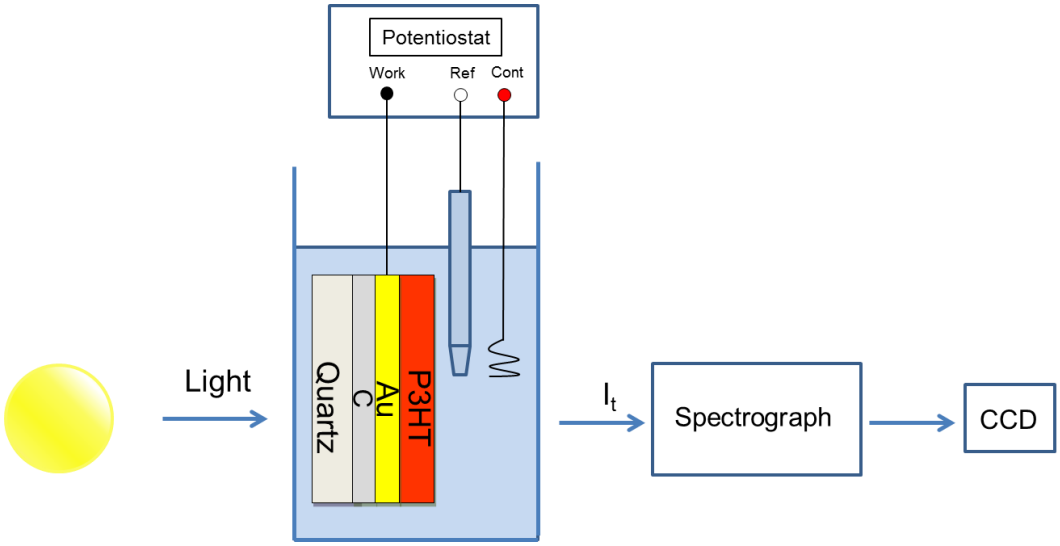

Figure 2.15 Schematic of optical system Setup used for solution experiment. Light passes through sample and then the spectrograph, and finally is monitored by a CCD detector. One sample, a Pt wire and one non-aqueous $Ag/AgNO_3$ electrode are used as working electrode, counter and reference electrodes, respectively, and are connected to a potentiostat.

2.3.2 Apparatus used for measuring repetitive write/read/erase/read memory cycles

Figure 2.16 shows the in-situ optical system setup used for measuring repetitive memory cycles. Light came from the 100 Watt Quartz Halogen bulb of the microscope (BX60, Olympus), transmitted through the channel of working memory device, reached a 50X objective lens, then was received by the spectrograph(Shamrock sr-303i, Andor Technology) and monitored by CCD detector (Newton, Andor Technology). Meanwhile, repetitive write/read/erase/read memory cycles were examined by a Keithley 2602A dual channel source measurement unit. A small readout voltage V_{SD} (~0.5V) was applied between Source and Drain, and the readout current was initially very low because the P3HT was not oxidized and the device was OFF. Then a relatively high voltage V_{SG} (~3—4V) was applied for 1s between Gate and Source to oxidize P3HT, resulting in an ON state of the device, which was confirmed by the relatively high readout current when the V_{SD} was applied. In the erasing process, an opposite bias V_{SG} (-3—-4V) was applied for 1s, resulting in an OFF state of the device, and the low readout current. The write/read/erase/read cycles was controlled and repeated by a laboratory computer and Visual Basic (Microsoft). The reference spectrum was taken using the “device” which did not have P3HT and PEO layers.

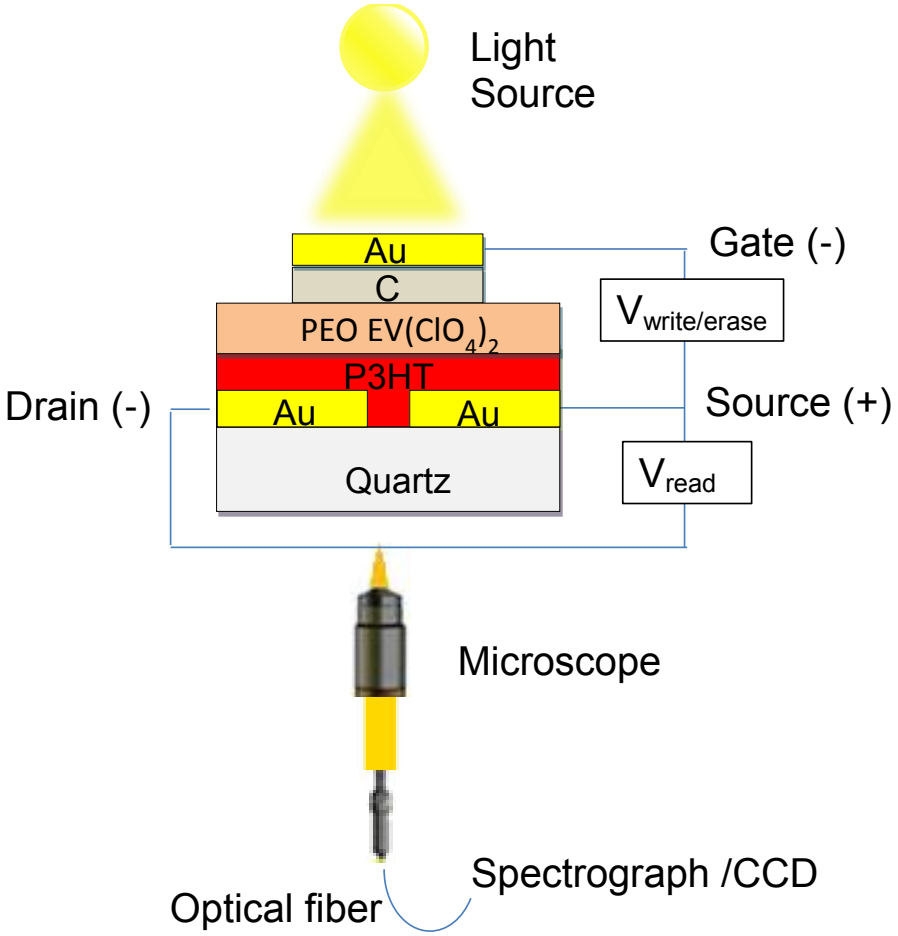

Figure 2.16 Schematic of In-situ optical system used for monitoring repetitive write/read/erase/read memory cycles. UV-Vis absorption spectroscopy is applied through a microscope to determine redox changes during polymer memory device operation.

2.3.3 Apparatus used for measuring memory switching characteristics

The write/read/erase/read cycles examined using Keithley 2602A dual channel source directly show evidence whether devices have memory effect. However, the design of the Keithley source limits the detection speed. In order to measure fast changes of memory devices in writing and erasing process, a more sophisticated electronic measurement system was used, as shown in Figure 2.17. supply constant voltage was of +0.5V was connected to Source electrode, and confirmed with a digital multimeter. A SRS current amplifier was connected to drain electrode, which is grounded in order to impose a constant readout voltage of +0.5V between Source and Drain. The "low" shielded input connector of a second SRS amplifier was controlled by the V_G output voltage (AO 0) of a National Instruments 6110 data acquisition board. V_G was +0.5V at the start of the memory cycle, and then shifted to -3.5V for 1s to impose a 4 V pulse between S and G, with S positive. Finally, a 5V pulse to a mechanical relay opened the Source-Gate circuit, resulting in an open S-G circuit. The absorption spectra were recorded as described in section 2.3.2, and was used during the whole memory cycle to detect optical changes. The current measurement system was much faster than the Keithley 2602. Software written in Labview by Bryan Szeto was used to automatically control the whole system.

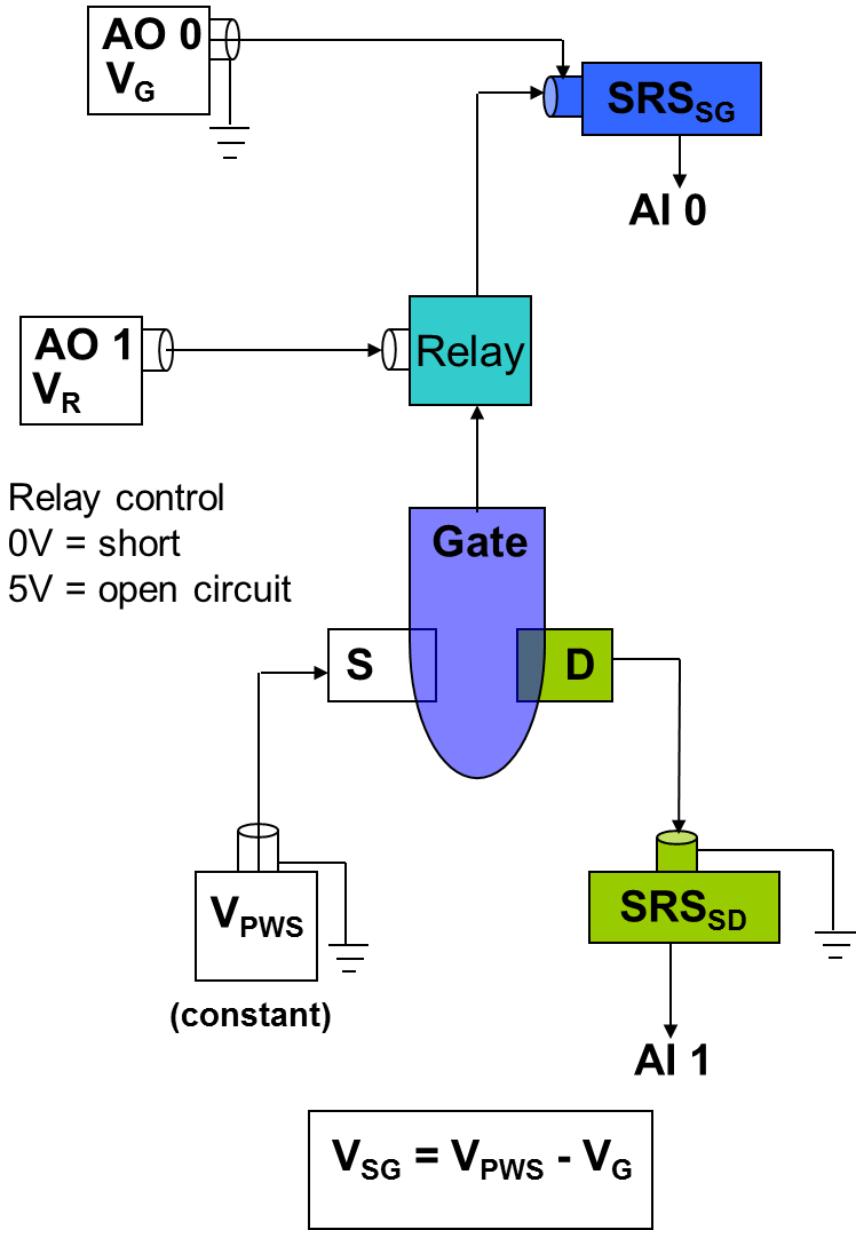

Figure 2.17 Schematic of electronic measurement part used for testing memory characteristics. Constant power supply is set as 0.5V and connected to source electrode. One SRS current amplifier is connected to drain electrode, which is grounded in order to make constant readout voltage of 0.5V between source and drain. The gate is connected to another SRS current amplifier, whose ground is firstly shifted to 0.5V, then -3.5V for 1s in order to write the memory device with a 4V difference between source and gate. Finally a 5V pulse is given to a mechanical relay to open the source-gate circuit. The absorption spectroscopy is used to detect any optical changes for the whole process.

2.4 Summary

In this chapter, the fabrication process of P3HT-based organic memory device was described. Each 18×13 mm quartz substrate contained 4 devices with a three-terminal structure. The channel width of each device was 20 μm. Simulation based on Filmstar showed that the transmittance through the channel was approximately ~20 - 35% from 400nm to 700nm, which was good for optical characterization.

Additionally, a new approach was used to form uniform electrolyte layer between the bottom and top electrodes, which were characterized by optical microscopy microscope, profilometry and SEM. Compared to drop cast layer reported previously, the devices fabricated with this new approach had thinner and more uniform thickness as well as low surface roughness.

Finally, in-situ optical detection was coupled with three different electronic measurement systems to probe the P3HT redox process in solution or solid state memory devices. Detailed system setup description was presented.

CHAPTER 3

IN-SITU SPECTROSCOPIC CHARACTERIZATION OF MEMORY DEVICES

3.1 Introduction

Optical studies of organic solid thin film have been reported in various research groups.[4, 6, 16, 23, 24, 64-66] In this thesis, a more powerful UV-Vis optical system is setup and used for in-situ characterization of memory device. Compared to the reported optical methods, this technique can fast detect a very small area (such as the channel part of the memory device), and this detection area can be further improved by changing objective lens part of the system.

There are three main reasons why spectroscopic characterization is widely used in detection of organic thin film: (1) Most of organic layer absorb light in the ultraviolet-visible region, which provides a possibility to simultaneously analyze any changes associated with organic layers in a wide range. (2) Optical studies directly show evidence of change within active organic layers, especially in UV-Vis range. It is straightforward to have an insight into energy level and transfer of electrons within or between the active layers, by measuring transition of absorption spectra as a function of time or voltage applied. (3) Time resolution of optical absorption detection system may reach to microseconds with broad-band light sources. It is necessary to reach a relative high time resolution for in-situ detection of working devices, since most electronic devices also work in a very

fast speed. For these reasons, optical absorption spectroscopy has been proven to be a useful and powerful in-situ detection technique of buried layers in organic electronic devices without damaging the working devices or adding interference.

3.2 Results and discussion

3.2.1 Spectroelectrochemistry in Solution

Figure 3.1 shows a cyclic voltammogram of solid P3HT film sample fabricated in 2.3.1, which was inserted into 0.1M TBHFP acetonitrile solution. The scan started at -400mV, and proceded to 1000mV and then scanned back to -400 mV, with a scan rate of 100mV/s. The $Ag/AgNO_3$ reference electrode was used for this voltammetry. Two quasireversible waves centered at 150 mV and 620 mV were observed at 0.1 V/s. The result shows that redox occurs in solid P3HT layer in electrolyte solution.

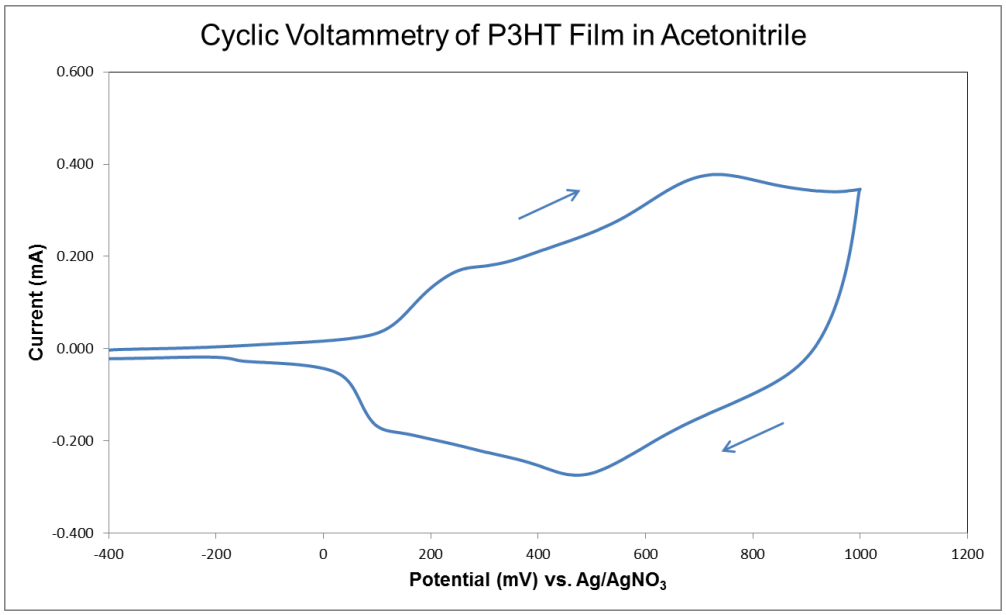

Figure 3.1 Cyclic voltammetry of solid P3HT film spin coated on quartz/C/Au substrates. Voltammetry occurred in acetonitrile containing 1.0M TBHFP versus $Ag/AgNO_3$ reference electrode. Scan begins from -400mV to 1000mV, and then goes back to -400mV with a scan rate of 100mV/s.

Absorbance changes were recorded by the optical system simultaneously with the voltammetric scan with an exposure time of 0.1 second, shown as Figure 3.2. The absorbance at 560nm and 650nm changed by ~0.2 absorbance unit, but in opposite directions, implying that the neutral P3HT is being oxidized to polaron. Reversal of the scan returned the absorbances to their initial values, indicating chemical reversibility. In all cases, reference spectrum was first recorded using reference sample made in 2.3.1. Both the results from CV and optical system indicate this redox process is reversible, a requirement for a memory device capable of repetitive write/erase cycles. The reason why 560nm and 650nm wavelength were chosen will be discussed in the next part.

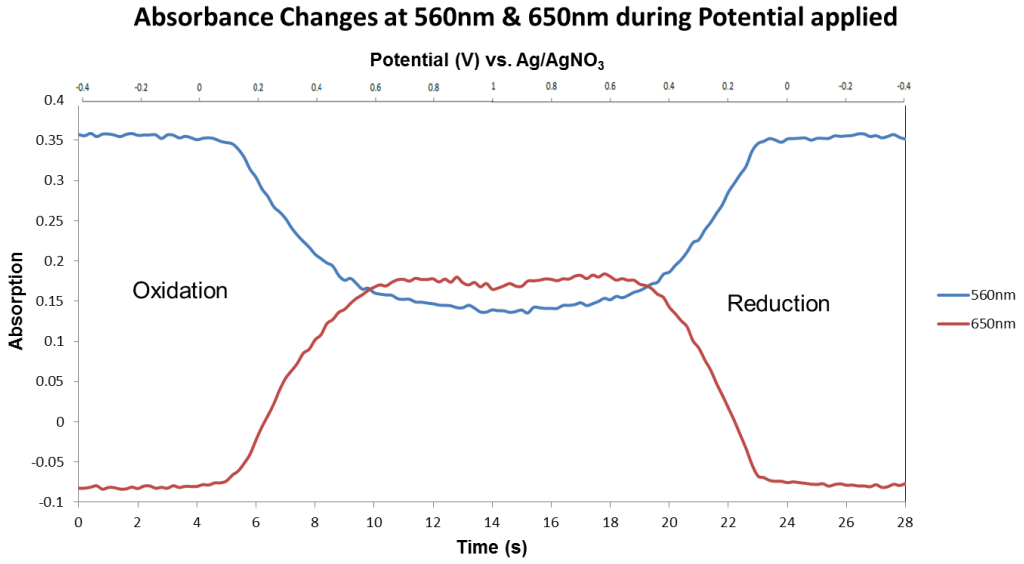

Figure 3.2 Absorbance changes at 560nm and 650nm during the cyclic voltammetry of solid P3HT film in acetonitrile containing 1.0M TBHFP versus $Ag/AgNO_3$ reference electrode. Scan rate is 100mV/s for voltammetry part. Exposure time of optical system is 0.1s in kinetic mode.

Figure 3.3 shows the absorbance spectrum of P3HT obtained with spectroelectrochemistry in 0.1M TBHFP acetonitrile solution. Constant voltages from 0-1.0V were applied to the sample for 60s at each voltage using DC potential amperometry mode of the potentiostat. A reference spectrum was first recorded using reference sample fabricated in 2.3.1. Then reference sample was replaced by the sample to be tested. Absorbance spectrum was taken in the last 5s of each voltage application, with exposure time of 0.1s. The typical absorbance spectrum of P3HT thin film obtained at 0V shows significant absorption from 400nm to 600nm, which is consistent with pervious reports.[24, 67-69] The peak at 510nm is assigned to the electron transition from HOMO to LUMO of the P3HT (2.43eV).[68] As the potential increases, the absorbance intensity from 400nm to 610nm decreases, but the absorption from 610nm to 850nm increases. In order to monitor the P3HT polaron generation as the neutral form is oxidized, 560nm was chosen for monitoring the P3HT neutral form, and 650nm was chosen to P3HT polaron form. (The reason will be discussed in next section) The apparent negative absorbance of 0.1 absorbance unit (A.U.) from 625nm to 850nm is due to the light reflection effect at the interfaces between Au, P3HT and ACN solvent. The P3HT layer apparently decreased the reflection of incident light, thus increasing the transmitted intensity above its value for the neutral film.

To estimate the concentration change of the neutral and polaron forms of P3HT during this spectroelectrochemistry experiment in solution, Beer's Law is introduced here to correlate concentration and absorbance data:

$$A(\lambda) = \sum_{i=1}^{i=n} \epsilon(\lambda)_i bc_i$$

where $\epsilon(\lambda)_i$ denotes molar absorptivity at wavelength λ of species i, c_i is the concentration, n is the number of species in thin layer. Also, two boundary conditions are introduced here: assume at 0V, the P3HT layer is only neutral, whereas P3HT is totally oxidized to polaron form at 1V. Assume b=26.2nm, c=1.1g/cm^3[70-72], and use a wavelength of 560nm, where the experimental values are: $A(560nm, 0V) = 0.3680$, $A(560nm, 1V) = 0.1665$), then:

$$A(560nm, 0V) = \epsilon(560nm)_{neutral} bc_{neutral}$$

$$A(560nm, 1V) = \epsilon(560nm)_{polaron} bc_{polaron}$$

Thus, $\epsilon(560nm)_{neutral} = 1.28 \times 10^5 g^{-1} cm^2$, $\epsilon(560nm)_{polaron} = 5.78 \times 10^4 g^{-1} cm^2$.

Table 3-1 shows the calculated results from 0V to 1V. As the potential increases, absorbance at 560nm decreases from 0.3680 to 0.1665, with $c_{neutral}$ and $c_{polaron}$ showing opposite trends. Ideally, the concentrations of neutral and polaron should obey the Nernst equation for the half reaction at 25 ℃:

$$E = E^{0'} - \frac{0.05916}{n} \log \frac{c_{neutral}}{c_{polaron}}$$

where E is the potential applied relative to Ag/Ag^{+} electrode, $E^{0'}$ is the formal potential, n is the number of electrons transferred in the reaction. Figure 3.4 shows the fitting of Nernst equation using the concentration which is calculated from Beer's law. The good linear fit (R^2=0.9977) also further confirms the calculated concentration of P3HT neutral and polaron states at different potential.

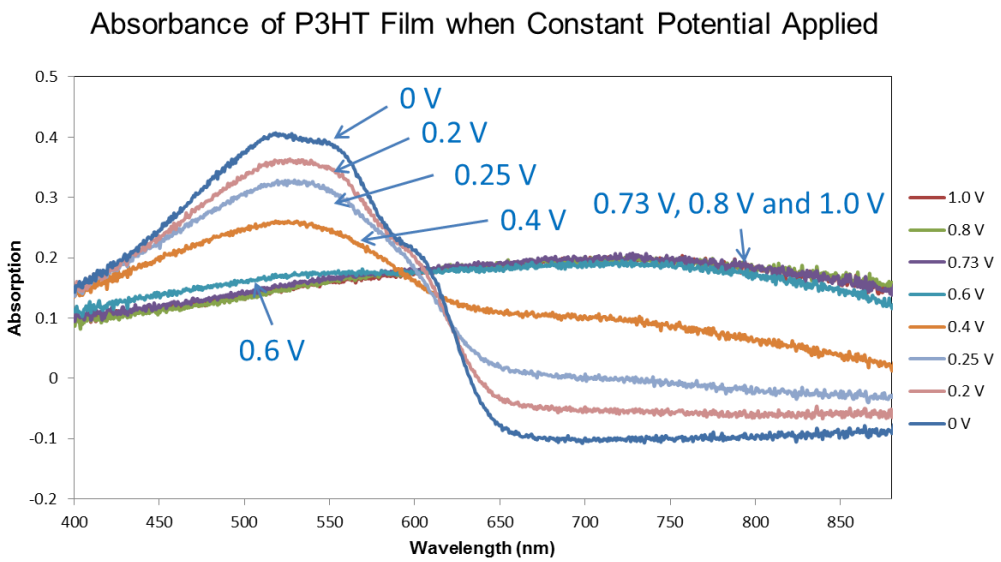

Figure 3.3 Spectroelectrochemistry characterization of P3HT film in 0.1M TBHFP acetonitrile solution. All voltages were referred to non-Aqueous $Ag/AgNO_3$ reference electrode. Each voltage was applied for 60s, and each spectrum was taken in the last 5s when potential was applied, with exposure time of 0.1s.

Table 3-1 Calculated concentrations of P3HT neutral and polaron forms

Voltage (V)	A(560nm)	$c_{neutral}$	$c_{polaron}$	$\log(\frac{c_{neutral}}{c_{polaron}})$
0.00	0.3680	1.1000	0.0000	N/A
0.20	0.3283	0.8754	0.2246	0.590797
0.25	0.2978	0.7133	0.3867	0.265898
0.40	0.2349	0.3714	0.7286	-0.29265
0.60	0.1763	0.0526	1.0474	-1.29913
0.73	0.1699	0.0181	1.0819	-1.77651
0.80	0.1682	0.0090	1.0910	-2.08358
1.00	0.1665	0.0000	1.1000	N/A

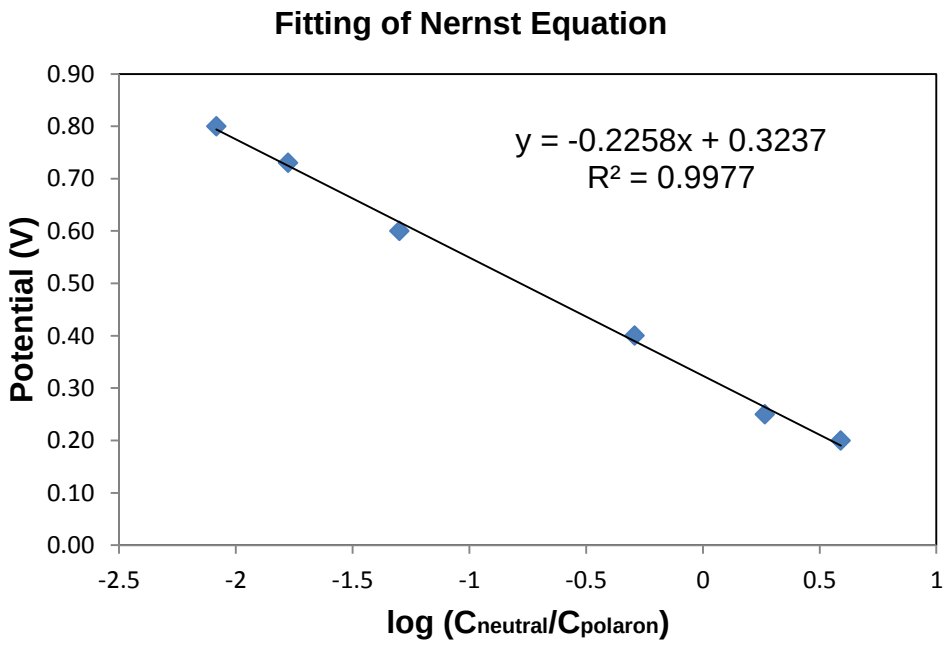

Figure 3.4 Fitting of Nernst equation using the concentration data calculated from Beer's Law. Fitting plot shows reasonable linear regression with R^2=0.9977.

In order to determine the rate of oxidation of P3HT in 0.1M TBHFP acetonitrile solution, two fast detection methods were chosen to work together to probe changes in the P3HT thin layer. Repetitive spectra were acquired for 40s to record absorbance changes with exposure time of 0.001s and sample interval time of 0.005s. Simultaneously, the DC potential amperometry mode of the potentiostat was used at 2s and recorded the current for 30s with a sample interval time of 0.05s. The result is shown as Figure 3.5. The absorbance changed immediately when the potential was applied at 2s. ~9.25×10^{-9} mol electrons were removed from the P3HT layer, corresponding to ~5.08×10^{-9} mol/cm^2 (sample-solvent contact area: 1.3cm $\times$ 1.4cm), which was close to the theoretical prediction using 4 thiophene rings per polaron unit (4.34×10^{-9}mol/cm^2). Furthermore, the solid film of P3HT can be completely changed from neutral form to polaron form within 0.5s, and reduced back to neutral at a similar rate. Most importantly, the polaron form of P3HT generated in Figure 3.5 (a) remains after the potential is removed for 5 minutes at open circuit until it is reduced back to neutral form in Figure 3.5 (b), which further indicates the feasibility of using P3HT to fabricate organic memory devices based on redox process

In order to examine whether the current followed the behavior expected for a simple diffusion control, the Cottrell equation is introduced here:

$$i = \frac{nFAc_j^0\sqrt{D_j}}{\sqrt{\pi t}}$$

where i is current, n is number of electrons to oxidize or reduce analyte j, F is Faraday constant which equals to 96,485 C/mol, A is area of the planar electrode, c_j^0 is initial concentration of the reducible analyte j; D_j is diffusion coefficient for species j; t is time of the process. Current consistent with the Cottrell equation is expected for a diffusion limited oxidation (or reduction). Although Figure 3.6 (a) show a linear region for a plot of I vs $t^{-\frac{1}{2}}$, it occurs for a limited time after oxidation began (2 to 2.5 sec). In addition, the reduction step (Figure 3.6b) is nonlinear. This is because reduction expels ions from the film, which oxidation incorporates ions from solution into the film. These results imply that diffusion of the counterion is likely involved in the oxidation, the polymer does not behave like a simple redox system in solution.

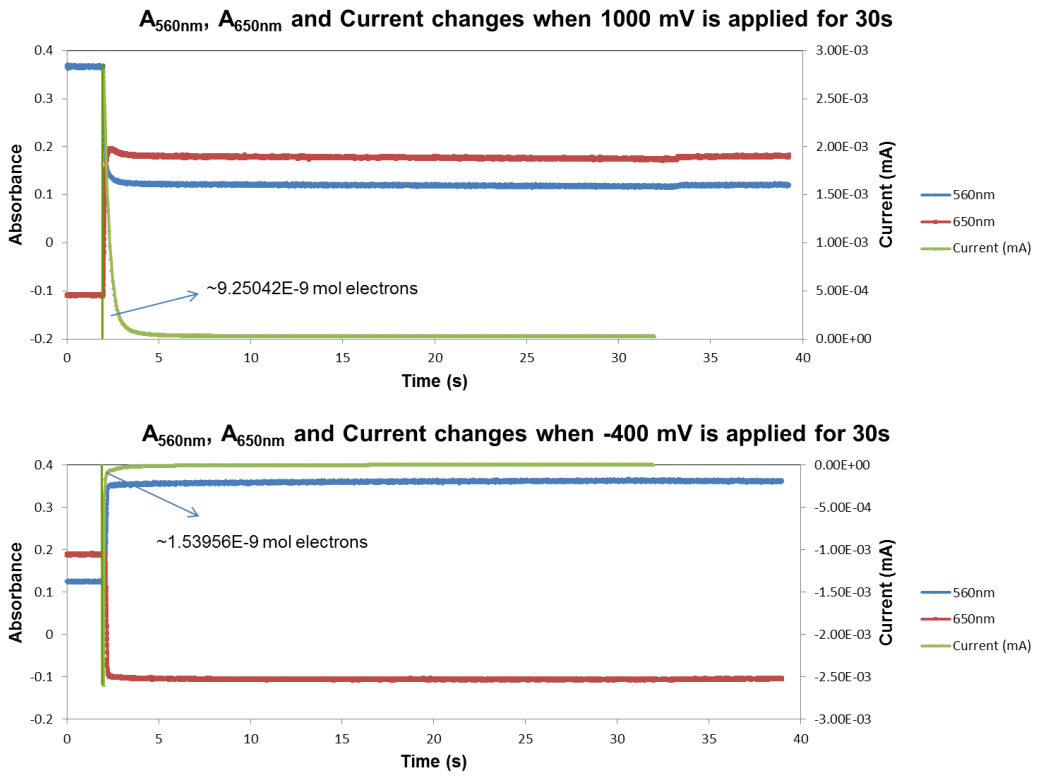

Figure 3.5 Correlation of A_{560nm}, A_{650nm} and current when constant voltage is applied for 30s. The sample interval of potentiostat and optical system are 0.05s and 0.005s, respectively. (a) 1000mv was used to oxidize P3HT to polaron form. (b) -400mV was used to reduce P3HT back to neutral form. The potential used here was related to $Ag/AgNO_3$ electrode.

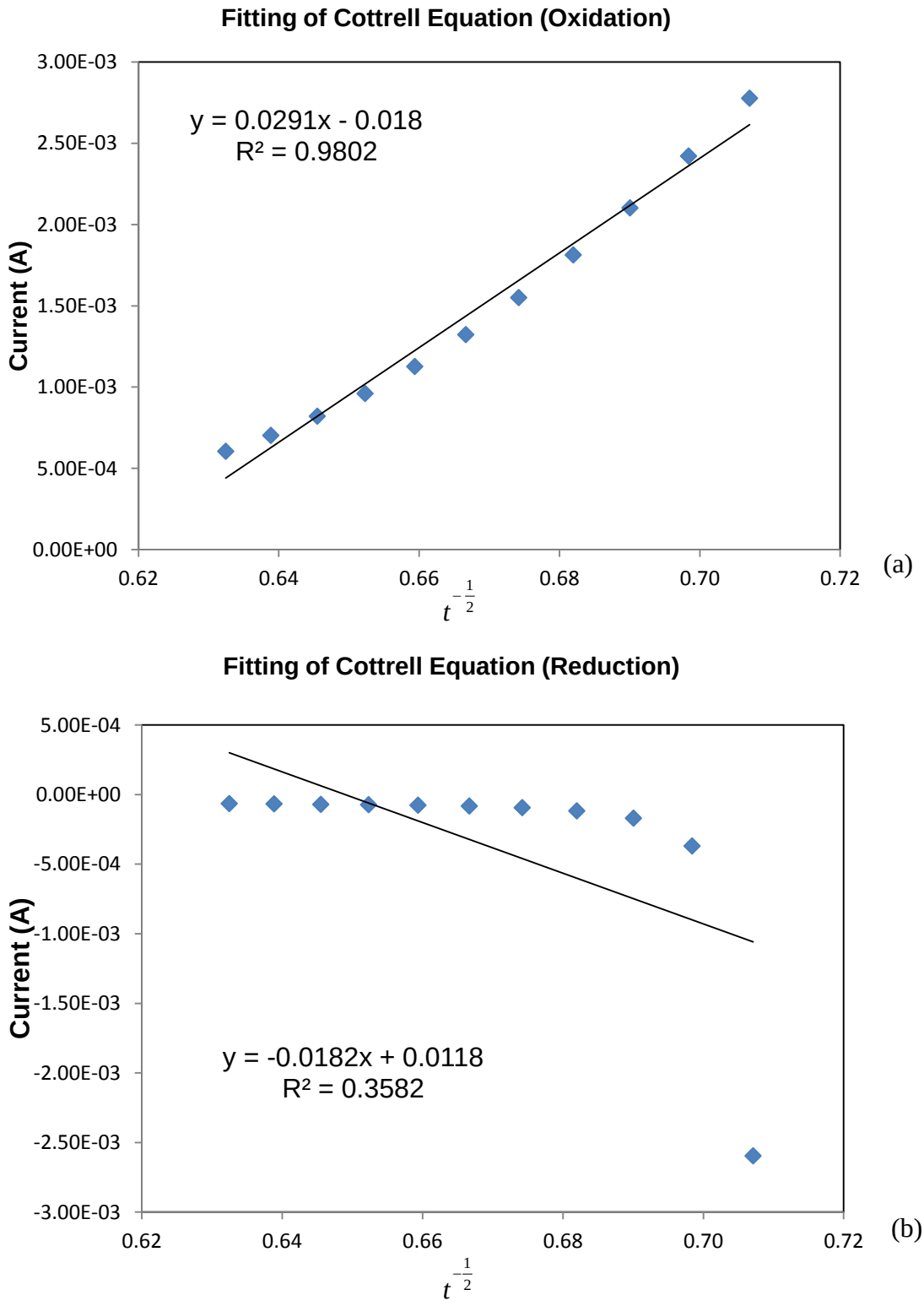

Figure 3.6 Fitting of Cottrell equation using current and time data from 2s to 2.5s. (a) Fitting using oxidation data. (b) Fitting using reduction data.

3.2.2 Absorption Spectroscopy in Solid State Devices

Figure 3.7 shows absorption spectra from 480nm to 700nm using the setup shown in 2.3.2. Constant voltages from -4V to +4V were applied to Source and Gate electrode for 10 seconds each. Ten absorption spectra were recorded during the voltage pulses using the optical system with exposure time of 1s for each voltage, then averaged into one spectrum with standard deviation of 0.002-0.008 A.U for each wavelength. As observed during the spectroelectrochemistry experiment in solution, when voltage increases from -4V to +4V, the absorbance from 480nm to 618nm decreases, but absorbance from 618nm to 700nm increases, with an isosbestic point at 618nm.

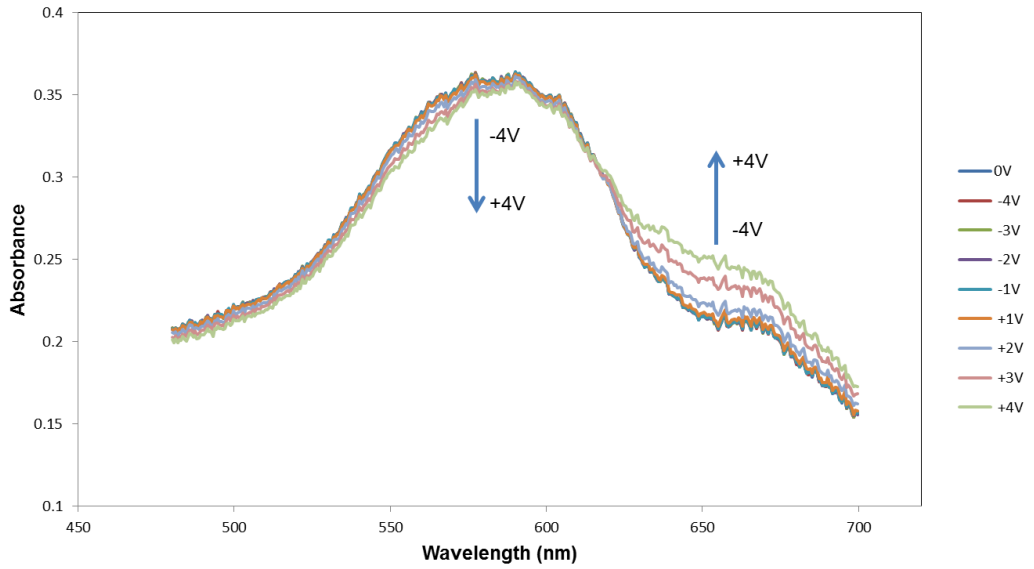

Figure 3.7 Absorption spectra of memory channel when different constant V_{SG} is applied. Drain electrode is floating.

In order to identify and assign particular wavelength to neutral and polaron forms of P3HT, the change in absorbance (ΔA) is introduced here, where ΔA is the change relative to the reference spectrum of the sample prior to an applied bias. Using this convention, a positive sign of ΔA identifies an absorbance increase and a negative sign of ΔA identifies an absorbance decrease relative to the reference spectrum.[6] Thus, ΔA is used to indicate and monitor small absorbance changes when the sample has a large total absorbance. Figure 3.8 shows a comparison of ΔA for the solid state Au/P3HT/PEO+EV$(ClO_4)_2$/C/Au memory device which produced Figure 3.7 and a P3HT film in solution (Figure 3.3). Both the solid state and solution spectra show decrease trend at 560nm and increase trend at 650nm were obtained when P3HT was oxidized to polaron form, which provides the evidence that similar redox process of P3HT occurs in memory devices compare to redox reaction of P3HT layer in solution shown in 3.2.1. Moreover, ΔA data show peaks at these two wavelengths in solid state devices during a change in bias voltage. However, the P3HT layer in the solid state memory device cannot be totally oxidized, resulting a smaller ΔA compared to that in solution, where counterions are available. Figure 3.9 shows the absorbance changes at 560nm and 650nm as bias increases in Au/P3HT/PEO+EV$(ClO_4)_2$/C/Au memory device. The error bar is one standard deviation calculated using 10 spectra, which is almost invisible in the figure.

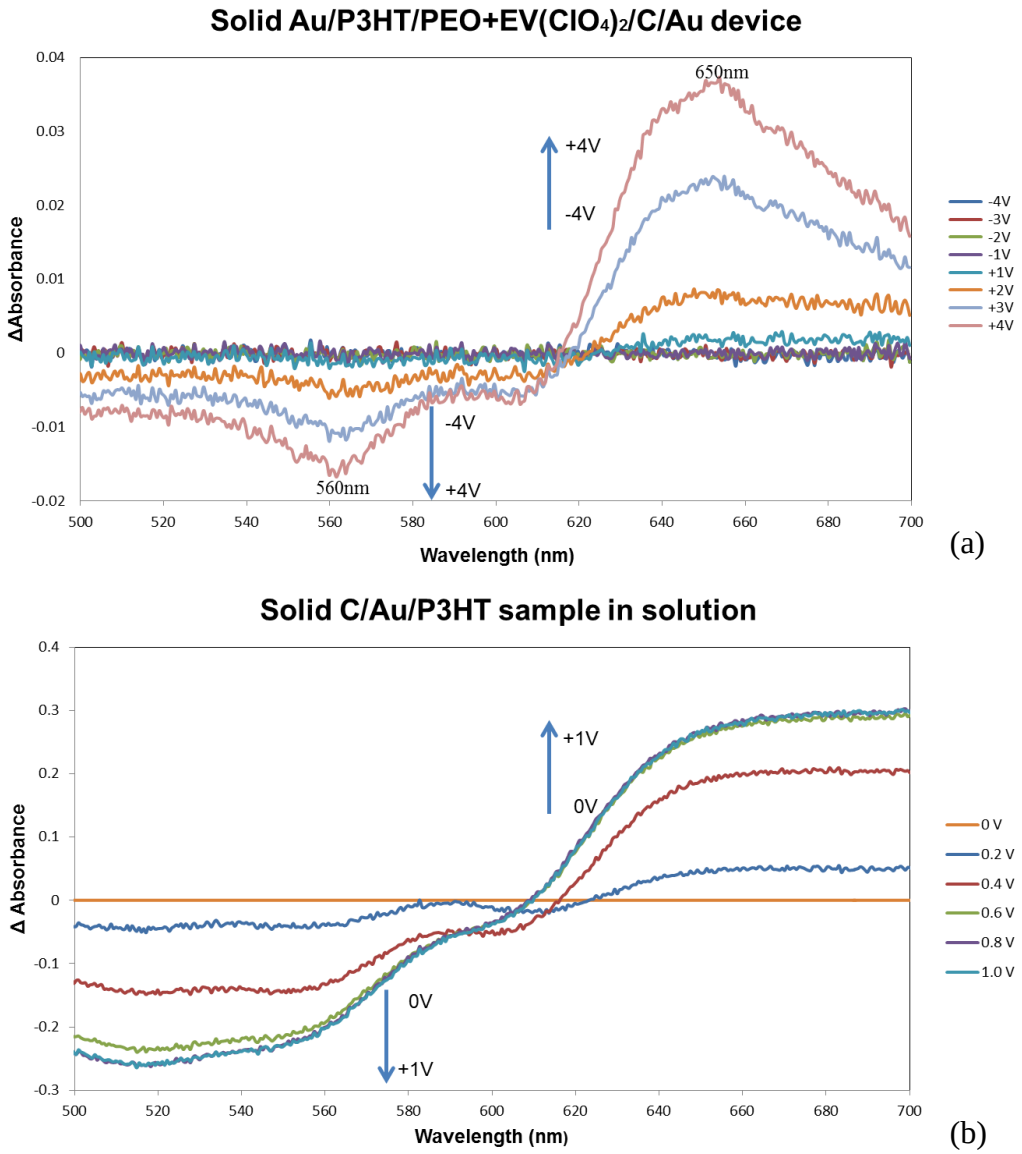

Figure 3.8 ΔAbsorbance of P3HT film in (a) solid state and (b) solution, showing isosbestic point at around 610nm. Same increase trend at 560nm and decrease trend at 650nm were obtained when P3HT was oxidized to polaron form.

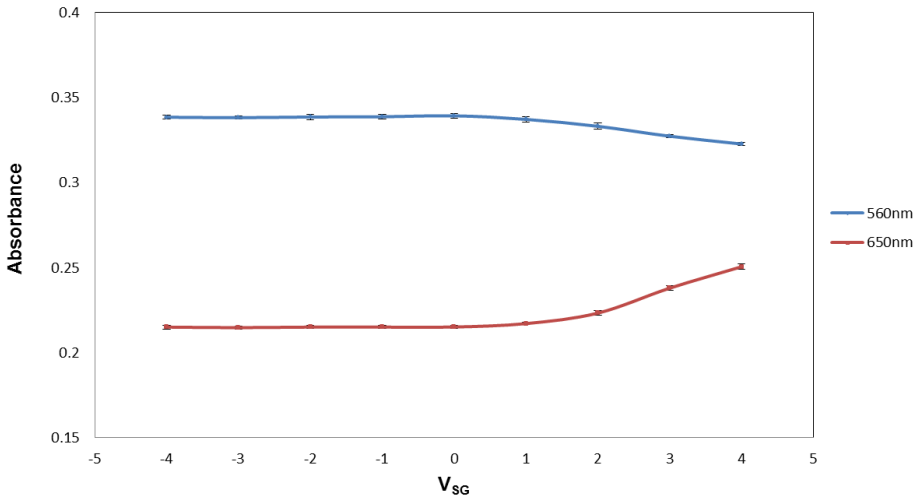

Figure 3.9 Correlation of A_{560nm}, A_{650nm} and V_{SG} in Au/P3HT/PEO+EV$(ClO_4)_2$/C/Au memory device. Error bar is one standard deviation.

Multivariate curve resolution (MCR) analysis (software provided by Eigenvector Research) was performed on the spectra in Figure 3.7 to determine the principal absorbing species distributions and their attribution (loading) to the observed absorption spectrum. 90 spectra obtained during different constant bias applied to the Au/P3HT/PEO+EV$(ClO_4)_2$/C/Au memory device comprised the input data set. Two boundary conditions were further input into the analysis: (1) each component only has a non-negative absorbance value at any wavelength. (2) the contribution of each component only has non-negative values during the whole experiment. No preprocessing of the raw spectra was performed during the MCR analysis. The two principal components (Figure 3.10(a)) accounted for 99.99% of the variation in the input raw spectra. Using previously reported spectra for the neutral and polaron forms [31, 73, 74], the red spectrum of Figure 3.10 was assigned to the polaron and the blue spectrum to the neutral P3HT. The spectrum loadings for different bias conditions are shown in Figure 3.10 (b), which indicates changes in distribution of neutral and polaron forms of P3HT as a function of bias. Also, at 560nm and 650nm, the MCR calculated spectra indicates apparent absorbance difference, which is consistent with the analysis in Figure 3.8. Thus 560nm and 650nm are assigned to neutral and polaron forms of P3HT respectively, and will be used to monitor P3HT polaron generation (memory ON state) and disappearance (memory OFF state) in this thesis. The "neutral" spectrum in Figure 3.10(a) contains contributions both from the neutral P3HT spectrum and from components of the device which do not change with applied voltage, particularly PEO.

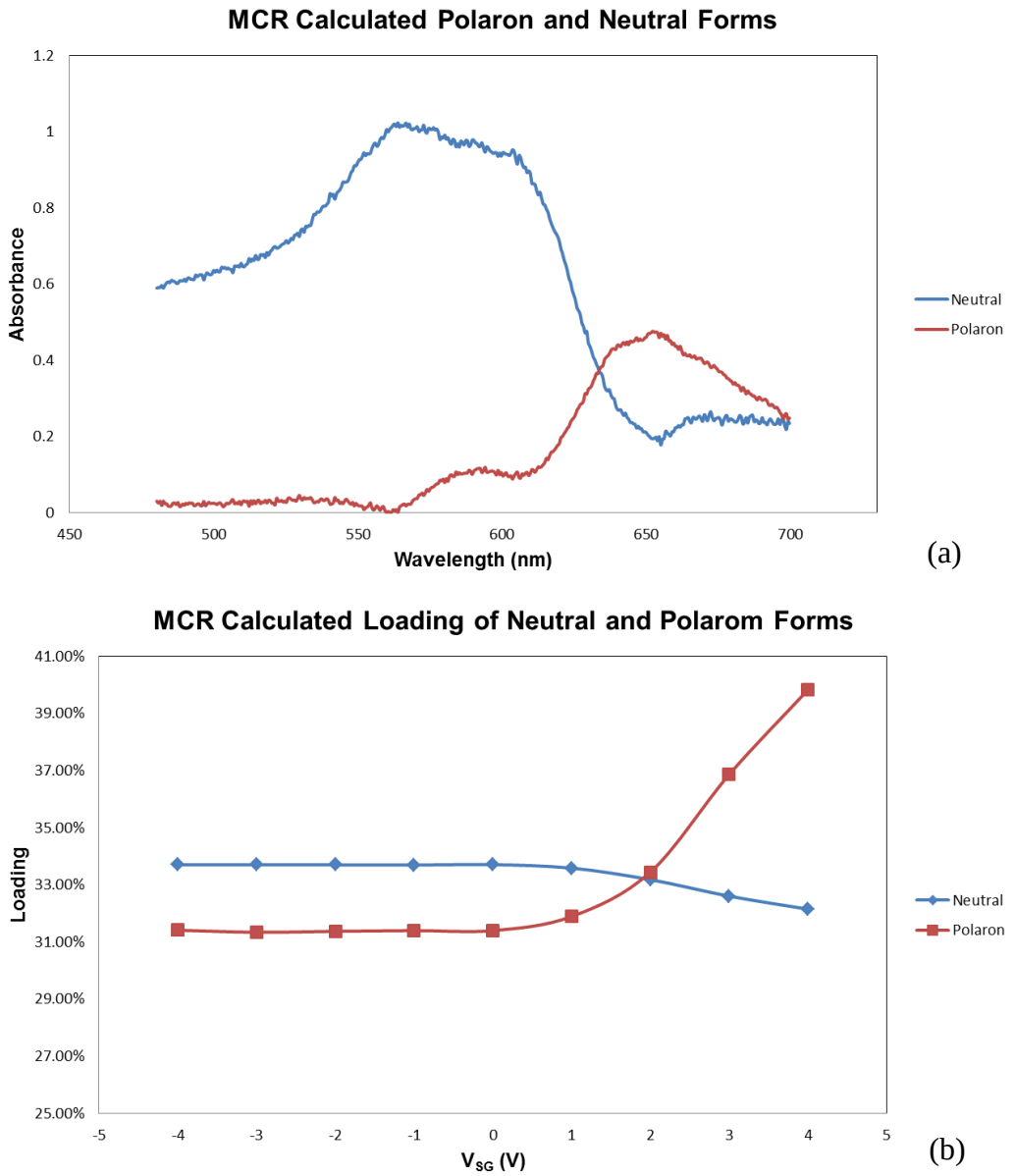

Figure 3.10 MCR analysis of absorption spectra obtained during different constant bias is added to Source and Gate electrodes of memory device. (a)MCR calculated spectra of two components in the P3HT layer. (b)MCR calculated loading of the two components during constant potential is applied.

Figure 3.11 shows the in-situ detection results of working memory device following the procedure indicated in 2.3.2. Memory device is switched by a SG square writing (+4V) and erasing (-4V) voltage lasting 1 second, the corresponding SG current is also recorded, as shown in Figure 3.11 (a) and (b). At the same time, a constant 0.5V SD readout voltage determined the SD conductivity which represents the "readout" of the memory device. Five SD current readings were taken in each state of the memory device at an interval of 2s when circuit of SG is open, as shown in Figure 3.11 (c) and (d). Due to the P3HT polaron generation after the SG writing pulse, the memory device is changed to ON state with a relatively high SD current (~10^{-5} to 10^{-4} A). After SG erasing pulse, the P3HT polaron form is reduced back to its neutral form, resulting in an OFF state with a low SD current (~10^{-8} to 10^{-7} A). The ON/OFF ratio is ~10^{2}. Absorption spectroscopy data at 560nm and 650nm also further confirm this ON state (low absorbance at 560nm and high absorbance at 650nm) and OFF state (high absorbance at 560nm and low absorbance at 650nm), using exposure time of 0.1s and cycle time of 0.15s (interval between two absorbance points), as shown in Figure 3.11 (e) and (f). When memory device is changed from OFF state to ON state, the absorbance at 560nm decreased by ~0.10 A.U., however, the absorbance at 650nm increased by ~0.06 A.U.

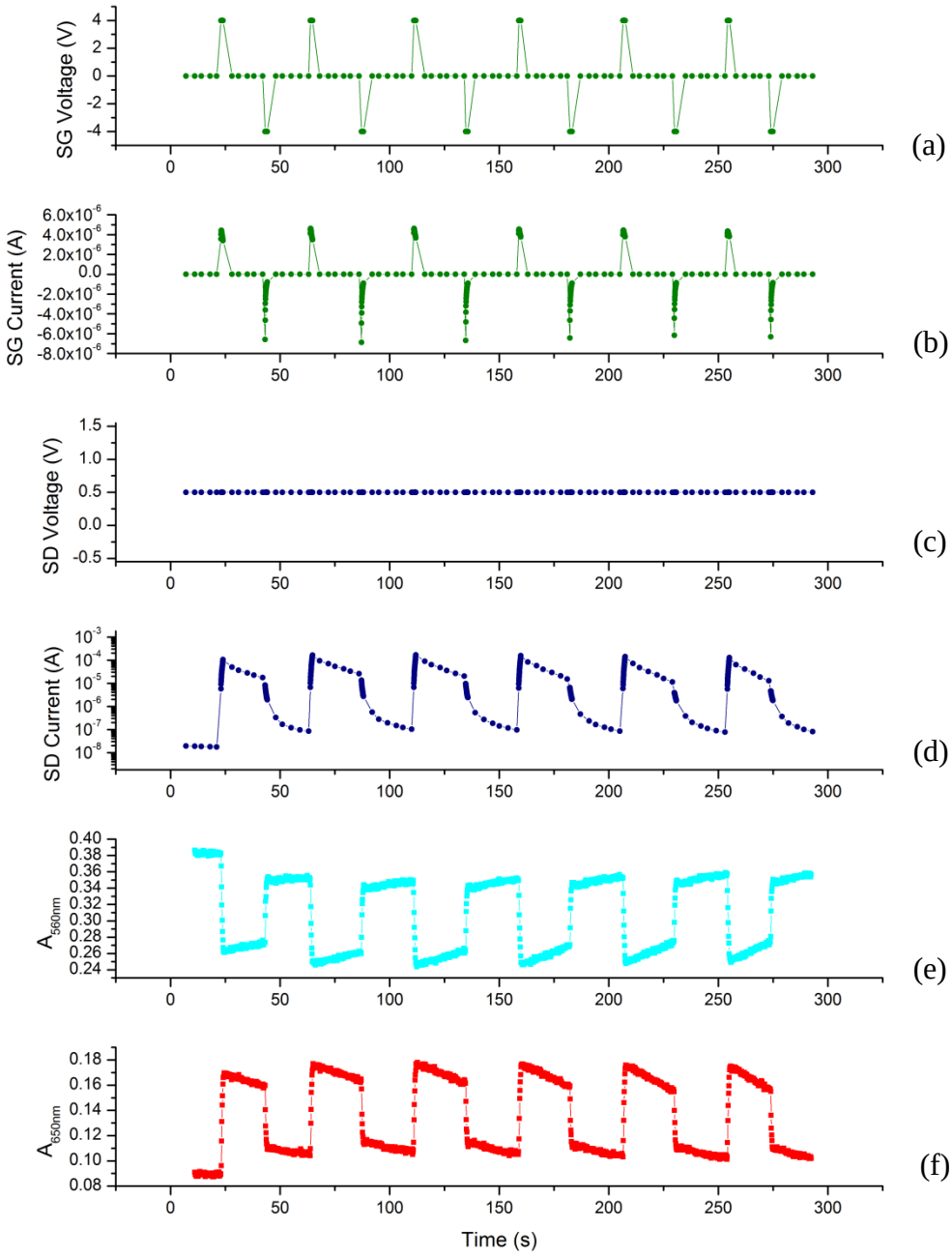

Figure 3.11 In-situ detection and correlation of A_{560nm}, A_{650nm} and I_{SD} on working memory device. (a) In the W/R/E/R cycles, V_{SG} is applied as 4V to write the device and -4V to erase, both for 1s. (b) I_{SG} is recorded during memory switching process. (c) V_{SD} is always applied as 0.5V to read out memory device status continuously. (d) SD current (e) Absorbance at 560nm (f) Absorbance at 650nm are used to identify the ON and OFF states. The exposure time of optical system was 0.1s with kinetic cycle time of 0.15s.

The reason of the slow decay after the device is changed to ON state is currently being investigated, but the most reasonable explanation is a recombination reaction between P3HT polaron and the reduced EV^{+} at the interface between P3HT and PEO. Figure 3.12 shows a comparison using and open or closed SG circuit after a writing or erasing pulse. Note that if Source and Gate circle is connected after writing/erasing pulse (i.e. SG circle is closed, Figure 3.12 b), the SD current, A_{560nm} and A_{650nm} decay much faster compared to open circuit shown in Figure 3.12 (a), which is not ideal for nonvolatile memory device. One explanation is that electrons are transferred back to Source from the Gate through the closed SG circuit, thus reducing the P3HT polaron to neutral form. This process is analogous to "shorting" a battery after it is charged, thus returning the system to its pre-charged state. This fast decay of ON state can also be found in retention study in Figure 3.13. Compare to the open SG circuit operation in Figure 3.13 (a), the closed SG circuit results in a short retention time (~20s), shown in Figure 3.13 (b). If the SG circuit is open after the writing process, the SD current, A_{560} and A_{650} remain longer in their ON states. In conclusion, the open SG circuit is strongly preferred for operation of memory devices, to extend the retention time,

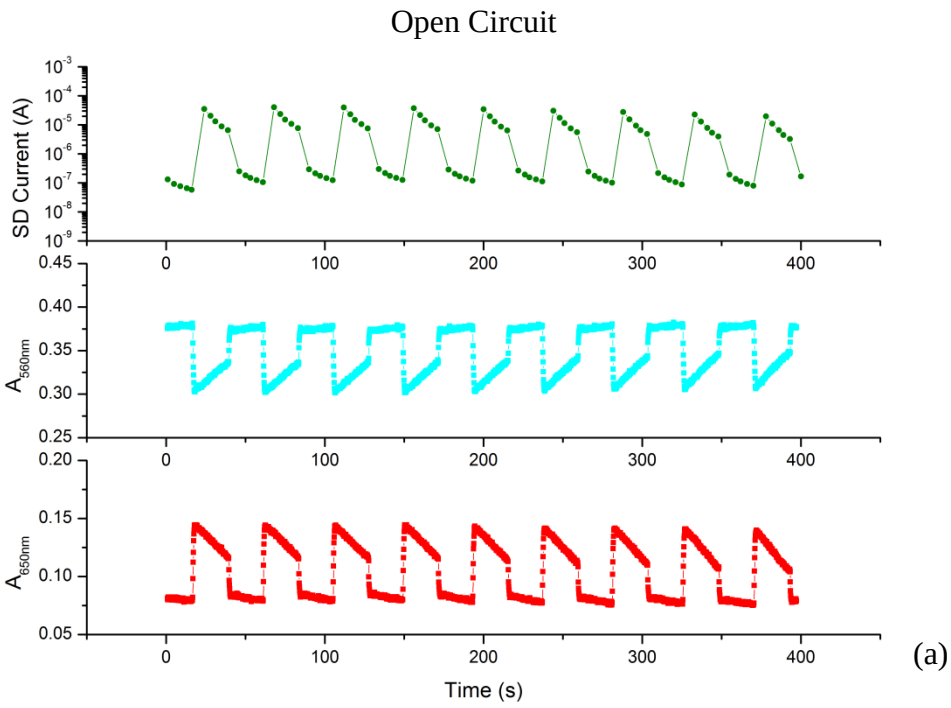

(a)

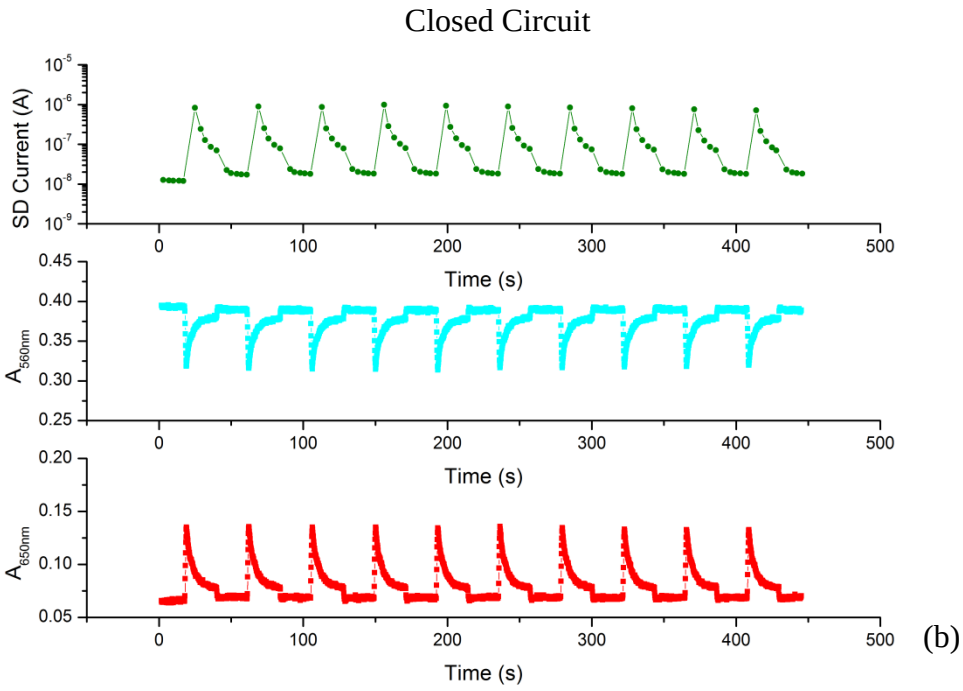

(b)

Figure 3.12 In-situ detection and correlation of A_{560nm}, A_{650nm} and I_{SD} on working memory device in (a) open circuit and (b) closed circuit.

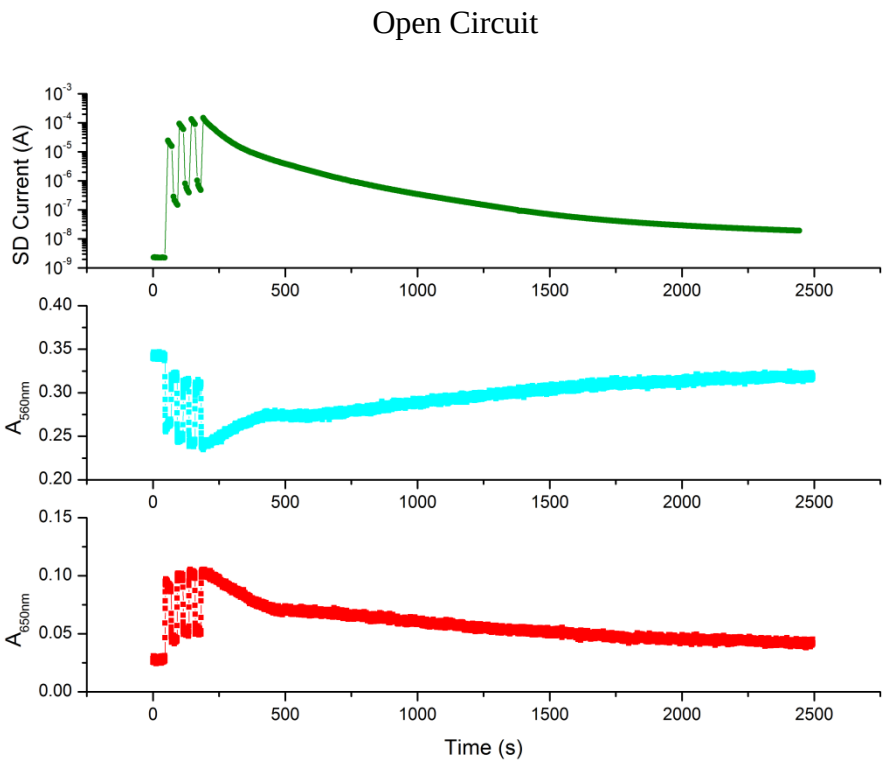

(a)

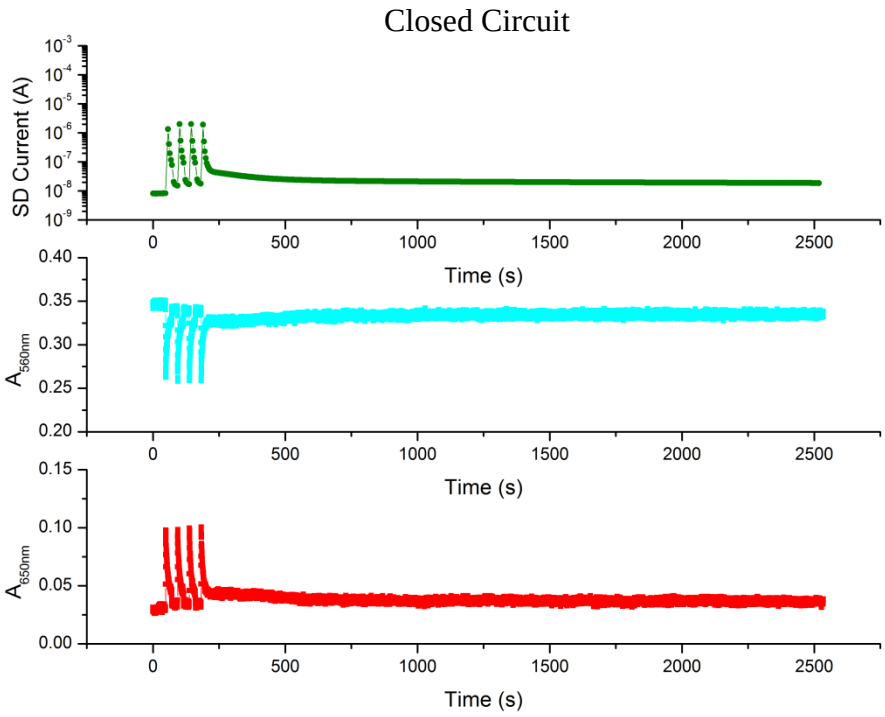

(b)

Figure 3.13 In-situ detection of memory retention time in (a) open circuit and (b) closed circuit.

The device geometry and dimensions were kept constant in this thesis to permit comparison to devices prepared by other researchers. However, the thickness of P3HT and the channel length can also affect the electronic and optical characterization. ON and OFF ratio may be higher by increasing the P3HT layer thickness. On the other hand, decreasing the P3HT layer thickness may decrease the ON state as well as the optical absorbance at 650nm. Furthermore, it may break the P3HT layer continuity at the edge of bottom electrodes in spin coating process. Changing the channel length can directly affect the switching speed of the memory device, which means broader channel length will have slower switching for the memory device, the mechanism is discussed in 3.2.4.

3.2.3 Dual Pulse Experiment

The setup in 2.3.3 provides a powerful technique to measure the characteristics of memory devices. In order to observe detailed SD and absorbance response during and after the writing process of P3HT memory device, 4V SG voltage was used to write the device for 1 second, and then the relay disconnected the S and G electrodes to form an open circuit as shown in Figure 3.14 (a). A comparison experiment was carried out without disconnecting the S and G electrodes, resulted a closed SG circuit as shown in Figure 3.14 (b). The time resolution of the current measurement is 10 μs, and the optical system can acquire a spectrum every 5 msec. Both the "open" and "closed" SG cases show similar SD current rise and absorbance changes in 560nm and 650nm during the 1 second writing pulse, which indicates polaron generation and a transition

from the OFF state to ON state. However, after this writing pulse, the SD current, A_{560nm} and A_{650nm} decay much slower for SG open circuit compared to those for the SG closed circuit. The results are similar to those generated using Keithley 2602A source (Figure 3.12 and Figure 3.13), but dual pulse system provides a much faster detection in a short period of time, which is as fast as 10 μs/point shown here, and up to 0.375 μs/point in 3.2.4.

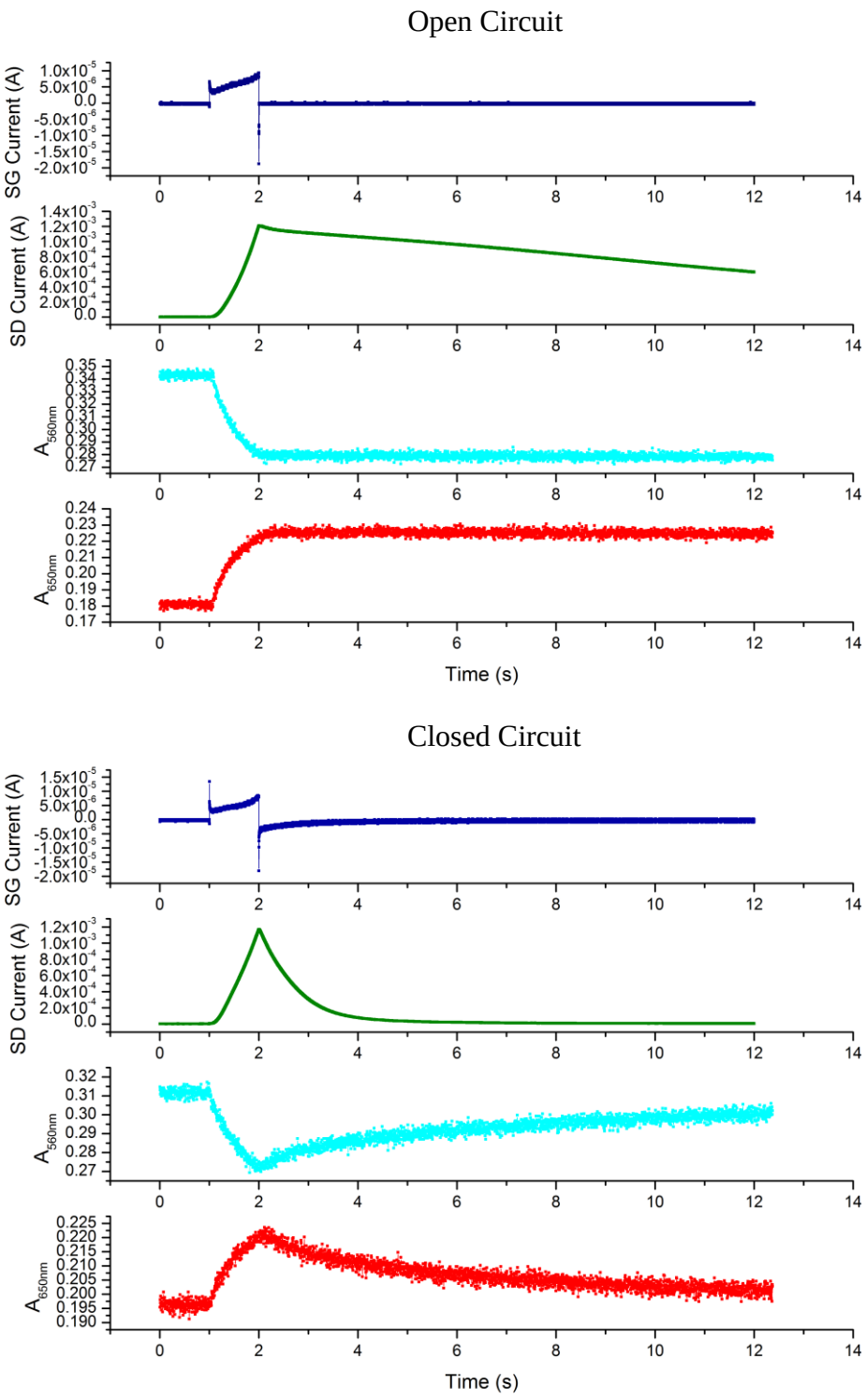

Figure 3.14 Characteristics of memory device during writing process using fast dual pulse system in (a) open circuit and (b) closed circuit. The entire test is carried out in ambient.

The SG and SD current response corresponding to the writing process for different atmospheres during testing on the PQT/PEO-EV$(ClO_4)_2$ three terminal memory device was reported previously.[75] In the current experiment, the absorbance measurements were combined with the dual pulse measurement to investigate the effect of atmosphere on switching behavior. A single device was first tested in air, then in nitrogen after exposure to vacuum (~1.0×10^{-5} torr) for 12h, then again after exposure to vacuum for an additional 12 hours followed by saturated acetonitrile vapour in nitrogen. The motivation of the vacuum treatment is to remove residual moisture in the memory device, especially in the P3HT and PEO-EV$(ClO_4)_2$ layers, since water can act as a redox system and can also solvate ions. Acetonitrile is unlikely to undergo redox reactions but can solvate ions to increase their mobility. [75-78] The gate electrode is sufficiently thin to permit equilibration of the inside of the junction with the local atmosphere, thus modulate the optical and current responses, as shown in Figure 3.15 and Figure 3.16. The SD current in ACN vapour increases faster than that in air and nitrogen, shown as Figure 3.15(a), indicating a strong effect of local atmosphere. This is also consistent with Δabsorbance at 560nm shown in Figure 3.15 (b), where Δabsorbance at 560nm also decreases faster in ACN vopour compared to that in nitrogen condition, as well as slightly faster than that in air condition in the first 0.5s upon careful analysis. Figure 3.15 (c) shows the generation of polaron in air is much quicker than in nitrogen. Even through Δabsorbance in ACN vapour is almost the same as that in nitrogen, the absolute value of absorbance in ACN vapour is much higher than that in nitrogen in original recorded data, which is not

shown here. Figure 3.16 shows how the local environment affects the retention of the memory device. Compared to the normal detection in air, the ON current of memory device in nitrogen is ~100 times lower than that in air or ACN vapour, but this ON state is more stable. Furthermore, the ON state of device decays quite fast in ACN vapour, and relaxes to the OFF state again within 40s. These results are consistent with increased ion mobility in ACN vapour, resulting in more rapid recombination of polarons and reduced ethyl viologen. The results further confirm the correlation between polaron formation and conductivity, but also illustrate the importance of polar molecules such as water and ACN on speed and retention.

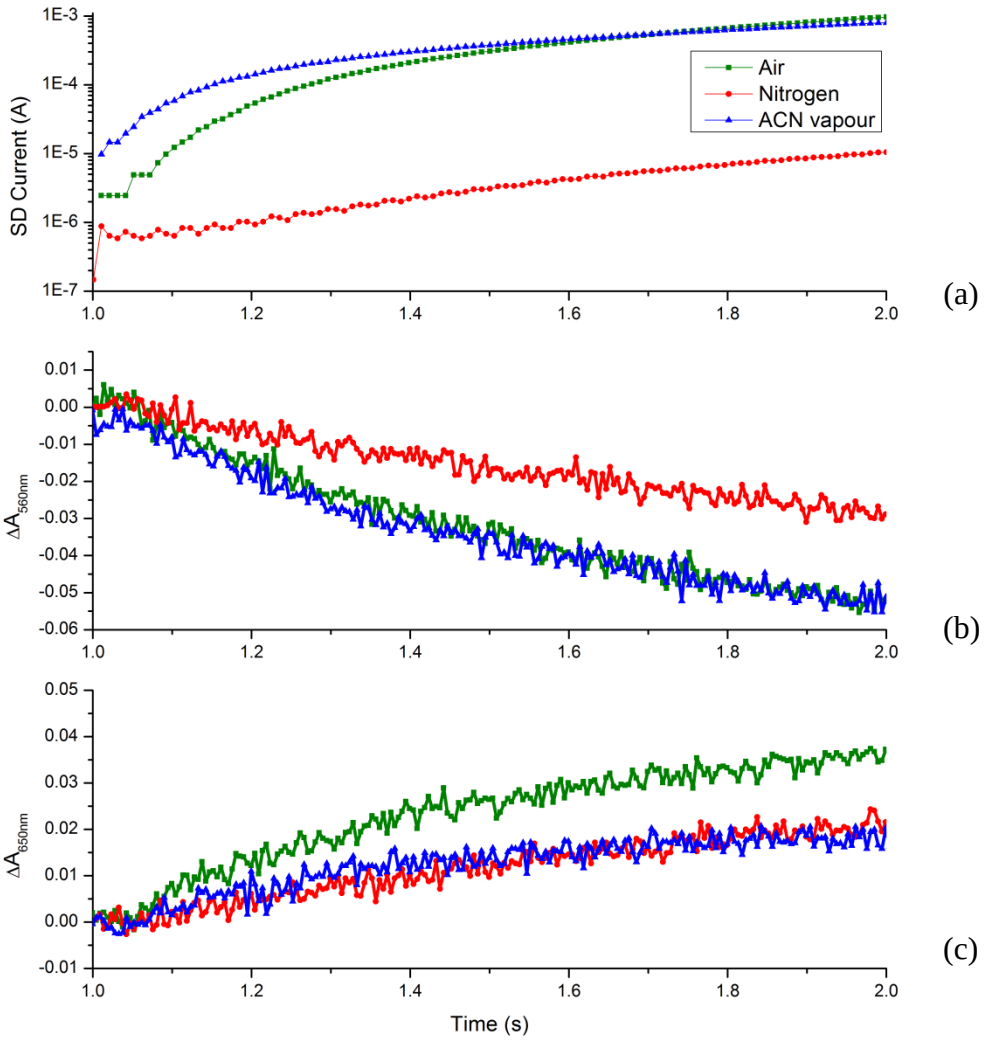

Figure 3.15 SD Current, ΔA_{560nm} and ΔA_{650nm} response of a P3HT memory device in the writing process using dual-pulse measurements under air, nitrogen, and acetonitrile vapor conditions. (a) SD current (b) ΔA_{560nm} and (c) ΔA_{650nm} response corresponding to the 1 second writing process. The "write" potential between source and gate electrodes is V_{SG} = +4 V, and the "read" potential between source and drain electrodes is V_{SD} = +0.5 V.

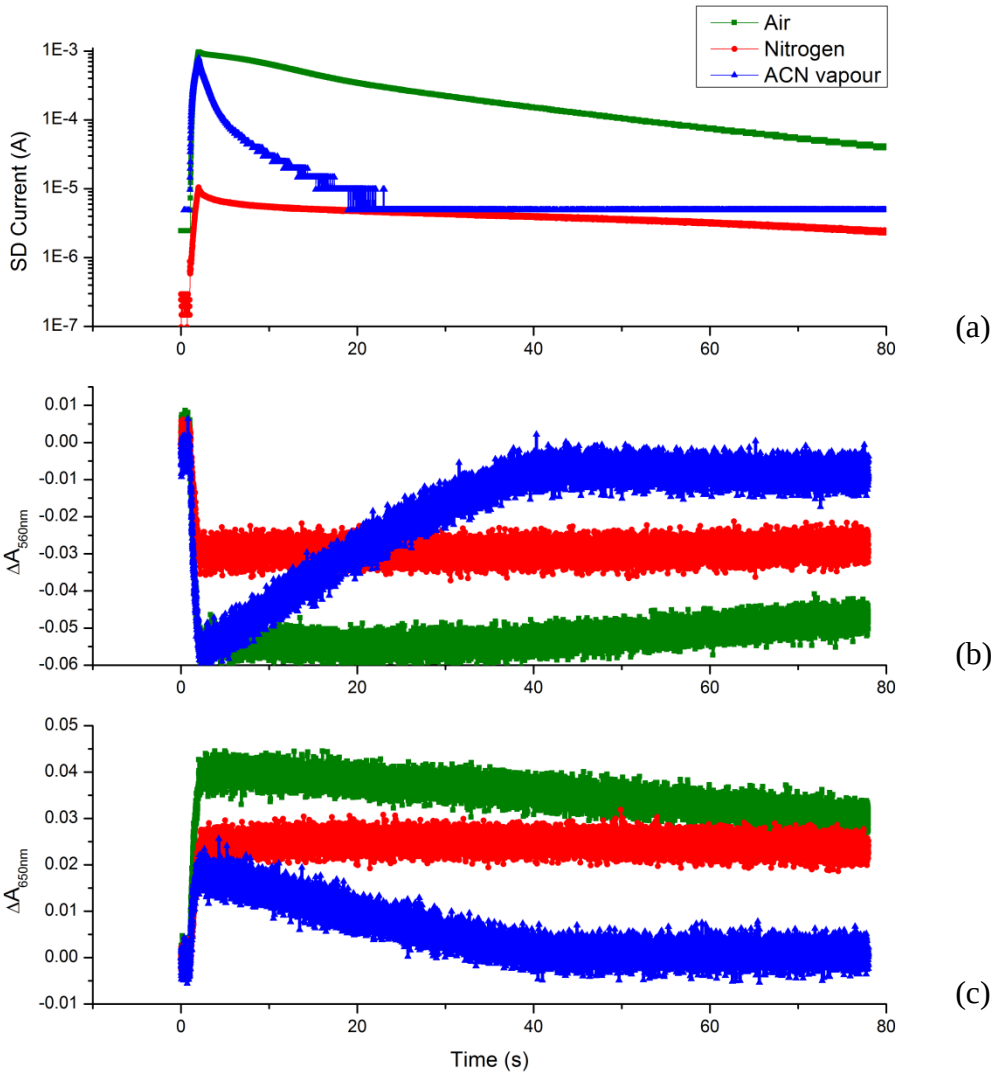

Figure 3.16 SD Current, ΔA_{560nm} and ΔA_{650nm} retention response using dual-pulse measurements under air, nitrogen, and acetonitrile vapor conditions. (a) SD current (b) ΔA_{560nm} and (c)ΔA_{650nm} response after writing process for 80s. The "write" potential between source and gate electrodes is V_{SG} = +4 V and last 1s in the beginning, the "read" potential between source and drain electrodes is V_{SD} = +0.5 V.

3.2.4 Polaron propagation and device switching mechanism

If we reconsider the geometry of this memory device to be similar to that of a thin film transistor, one could notice that the writing and erasing voltage is not present in the channel during the switching process, but only between the the Source and Gate electrodes. However, the generation and disappearance of P3HT polaron in the SD channel is confirmed by the SD current and spectroscopic results in 3.2.2. It is not immediately obvious how the polaron can be generated within the channel, when only the SG circuit is active. One possible mechanism is as follows: At the beginning, polarons are generated near the Source electrode during the writing process. Then these polaron may undergo a redox exchange reaction with P3HT neutral form in the channel, resulting in the oxidation of additional polarons between the S and D electrodes. By successive redox exchange reactions, the polarons may "propagate" across the SD channel and reach the Drain electrode. At the same time, EV^{2+} in the PEO layer is reduced to EV^{+}, and a ClO_4^- ion then transports from PEO layer to P3HT layer to compensate the polaron positive charge. As the channel is filled with P3HT polarons, the SD current increases and memory device changes from the OFF state to the ON state. During the erasing process, the polarons near the Source electrode are first reduced back to neutral form, and then the polarons near the Drain electrode then propagate back and are reduced at the Source electrode. The mechanism is shown schematically as Figure 3.17.

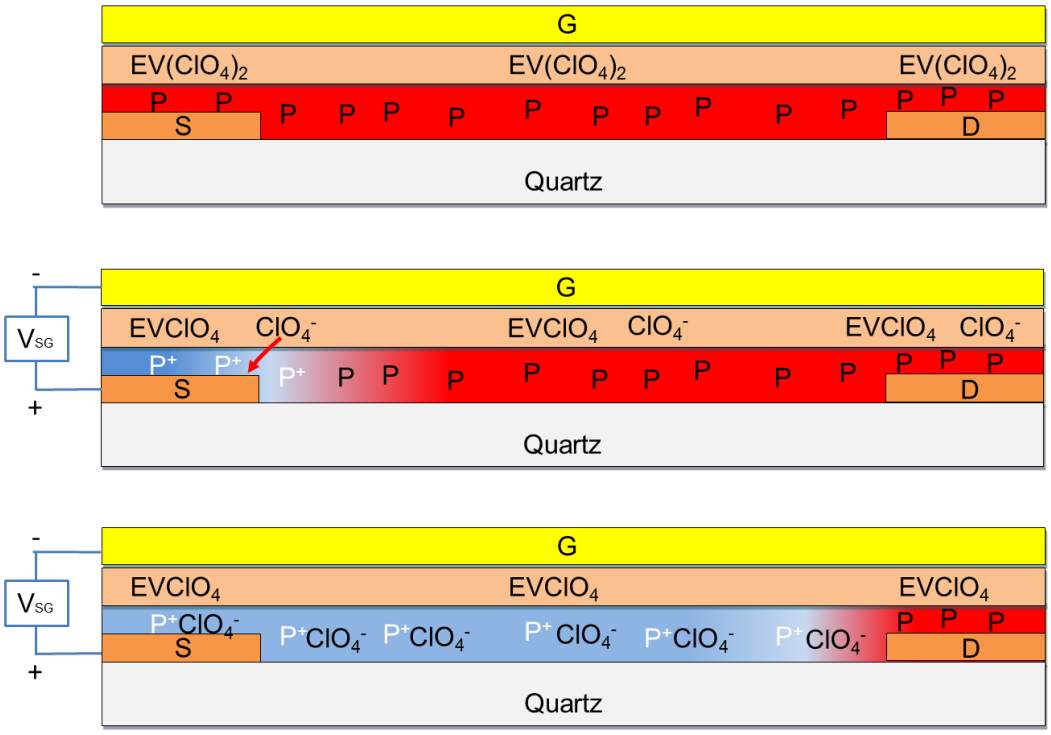

Figure 3.17 Proposed polaron propagation mechanism. EV is ethyl viologen and P is P3HT. Arrows indicated ClO_4^- transfers from the PEO layer to the P3HT film. The channel width is 20 µm. Not drawn to scale.

Based on this mechanism, two phenomena should be observed: (1) Polarons need time to propagate through the SD channel. (2) The SD conductivity changes as a function of time since polarons accumulate in the SD channel after the "front" reaches the Drain. In order to confirm this proposal, a fast and simplified detection characterization method was used with very similar arrangement to that shown in Figure 2.17. The relay was removed to keep Source and Gate connected. The Gate and Drain electrodes were connected to two SRS current amplifiers respectively, with both G and D held at virtual ground. For 100ms, 0V was applied to the Source, resulting zero voltage at all three electrodes. Then 3V was applied to the Source for 100ms, which generates P3HT polaron between the S and G electrodes. During this time, the current is monitored at the D electrode to indicate SD conductivity. Finally, the Source is returned to 0 V for 100ms to end the experiment. 8×10^5 points were recorded for each channel, resulting in 0.375 μs time resolution. The recorded SG and SD current of one sample are shown as Figure 3.18. After a delay time of ~10ms after the beginning of the "write" pulse, the SD current begins to increase as a function of time. Figure 3.19 shows SG and SD current overlay of 4 devices, where the log scale of SD current is used in order to magnify the current rise time. The propagation time is defined as the delay time after the beginning of the 3 V pulse required for an observable increase in the SD current. The average propagation time in this case is 16.3ms with a standard deviation of 5.2ms. So, the P3HT polaron propagation speed in this test is ~1.22mm/s, which is reasonable compared to 0.4-5mm/s reported in literature, where the propagation rate was

measured in a 20nm thick and 5-50mm long P3HT film using video camera to record the front position and potentiostat to measure the conductivity between two electrodes located in two sides of P3HT film.[79]

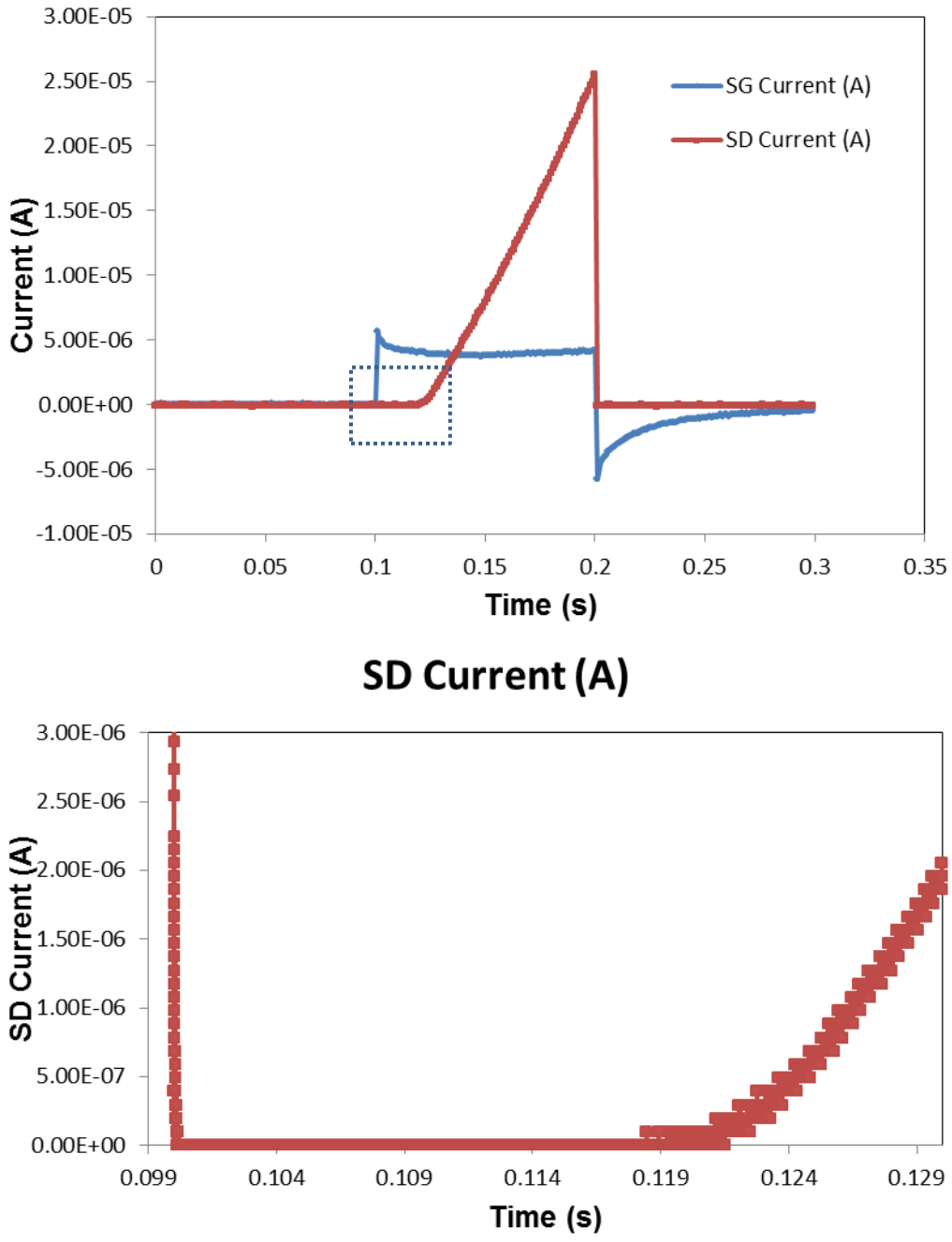

Figure 3.18 (a) SG and SD current recorded by high resolution detection system. (b) SD current in the beginning of writing process.

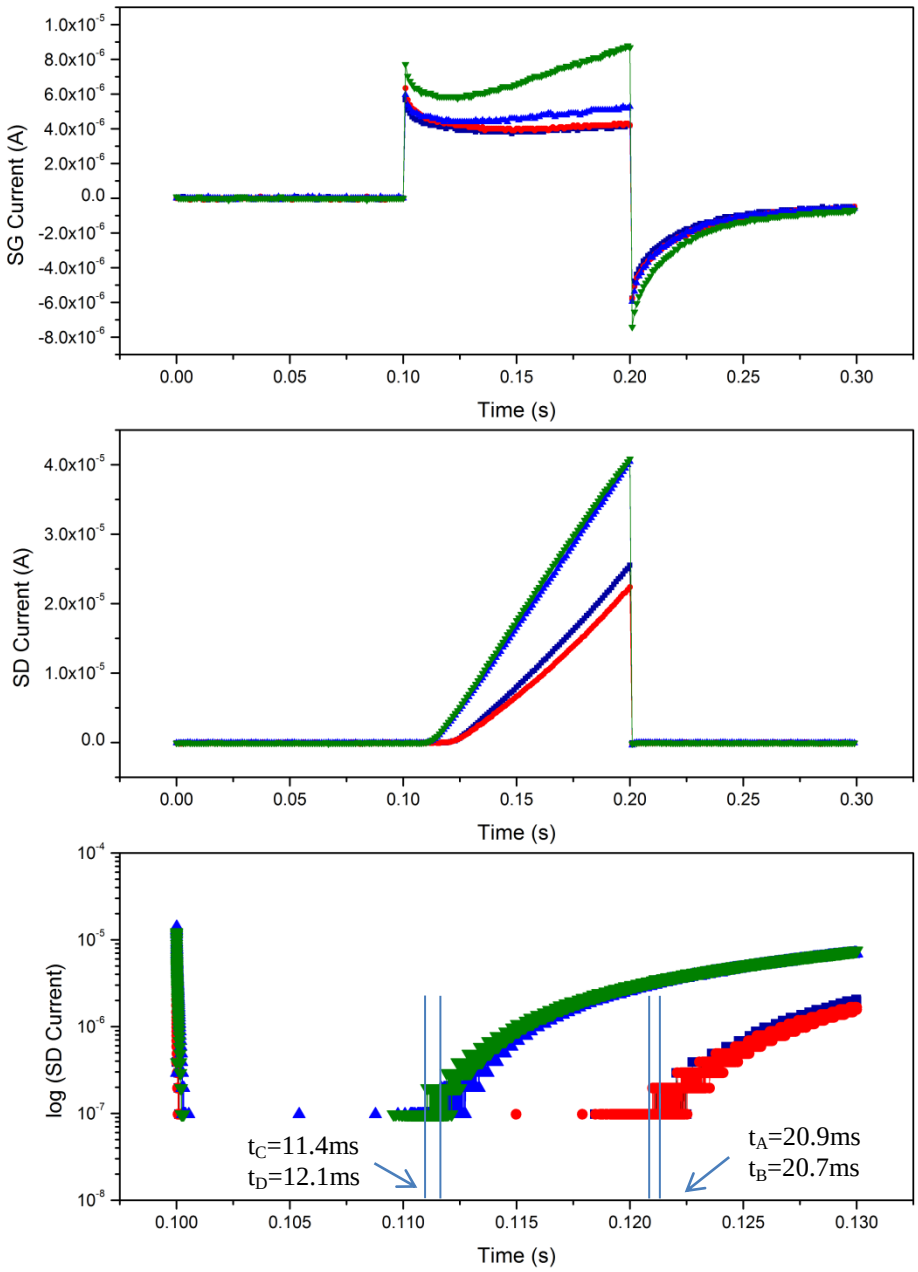

Figure 3.19 Propagation time of 4 memory devices using high resolution detection system with 0.375 µs resolution. (a)SG current (b) SD current (c)SD current in log scale in order to show the propagation time.

The time required for charging the capacitance between the S and G electrodes should be fast compared to the propagation time in order to accurately assess propagation across the channel. For a voltage pulse between the S and G electrodes, the following equation should apply for capacitive charging:

$$\ln i = -\frac{1}{RC}t + \ln\frac{\Delta E}{R}$$

where i is the SG current, R is the circuit resistance, C is the circuit capacitance, t is time, and ΔE is the voltage difference, which is 4V in this thesis. Table 3-2 shows the RC constants of four devices on the same chip, determined from the slope of ln i vs t, indicating an RC constant of ~40μs. This system response time is much smaller than the propagation time of P3HT polaron, thus confirming the feasibility of using the method shown in figure 3.19 to measure the propagation time.

Table 3-2 RC constants of system

Sample No.	Forward Edge	R^2	RC (s)	R (Ω)	C (F)
A	y = -23698x - 9.8646	R² = 0.9925	4.21977E-05	7.69E+04	5.48E-10
B	y = -22752x - 9.9499	R² = 0.9938	4.39522E-05	8.38E+04	5.24E-10
C	y = -24908x - 9.8723	R² = 0.9969	4.01477E-05	7.75E+04	5.18E-10
D	y = -23675x - 9.6905	R² = 0.9958	4.22386E-05	6.47E+04	6.53E-10
Sample No.	Reverse Edge	R^2	RC (s)	R (Ω)	C (F)
A	y = -23396x - 8.548	R² = 0.9944	4.27423E-05	2.06E+04	2.07E-09
B	y = -28729x - 8.4879	R² = 0.9943	3.48080E-05	1.94E+04	1.79E-09
C	y = -30502x - 8.7019	R² = 0.9943	3.27847E-05	2.41E+04	1.36E-09
D	y = -20583x - 8.1211	R² = 0.9940	4.85838E-05	1.35E+04	3.61E-09

3.3 Summary

In this chapter, in-situ optical detection was coupled with three different electronic measurement systems to probe the redox process P3HT film. The solution experiment provided some basic parameters related to the redox reaction in P3HT layer, and confirmed the feasibility of using P3HT as the active layer in nonvolatile memory device. Both of the Δabsorbance data and MCR analysis using in-situ detection measurement provided evidence that two principle components, which were assigned to P3HT neutral and polaron, and were correlated with the memory device ON and OFF states. The in-situ optical detection system coupled with a Keithley 2602A source measurement unit was used to monitor the memory device on a microsecond to second time scale, permitting simultaneous monitoring of SG current, SD current, A560nm and A650nm. A faster in-situ detection system using Labview data acquisition modules was used to monitor the characteristics of memory devices during the writing process with time resolutions down to 0.375 μs for SG and SD current and 5ms for optical absorbance. Furthermore, the switching speed and retention of memory devices were examined in different local atmospheres, showing a strong dependence on the presence of polar molecules. Finally, the polaron propagation mechanism was proposed and examined by a different dual pulse configuration, which shows a ~1.22mm/s propagation speed.

CONCLUSIONS AND FUTURE WORK

Solid-state nonvolatile memory (NVM) device is commonly used in consumer electronics, where "flash" memory based on inorganic materials is still the major product in the NVM market. In order to achieve possibly lower fabrication costs and operation power, polymer memory as an alternative creates a considerable research area. In this thesis, Au/P3HT/PEO-EV$(ClO_4)_2$/C/Au NVM device was developed based on resistive switch of conducting polymers using ± 4V to switch ON and OFF states in the solid state. However, it is quite challenging to probe the internal structure and redox changes of very thin solid state molecular layers "buried" under a metal electrode[7, 80]. Herein, a fast, non-destructive and simultaneous optical absorbance technique was coupled to different electronic characterizations to in-situ probe the polymer redox reaction in the working memory device, in order to investigate switching speed and retention time.

In chapter 2, the fabrication procedure of Au/P3HT/PEO-EV$(ClO_4)_2$/C/Au three terminal memory device was described. The fabrication was carried on 4-inch quartz wafer using conventional techniques, resulting in 20 chips with each containing 4 devices with TFT structure. Spin coating was used to deposit uniform P3HT and electrolyte layers with controlled thickness between the top and bottom electrodes. AFM was used to measure P3HT layer thickness as 26.2nm using Gaussian fit of depth profile, and shows the roughness Ra of 1.8nm. The characterization methods such as optical microscopy, profilometry and SEM

were used to examine the PEO-EV$(ClO_4)_2$ layer, resulting 550±20 nm thickness and 26nm roughness.

In chapter 3, the optical and electronic properties of P3HT memory device were described, based on in-situ absorbance spectroscopy coupled to three electronic measurement systems with different time resolution. Two principle components in the redox reaction, which are assigned to P3HT neutral and polaron forms with different conductivities and absorption, were identified through the analysis of the Source-Drain current and absorption spectra in the channel of the working memory device. Furthermore, a significant effect of solvent vapour on memory switching speed and retention was identified. Finally, the memory device working mechanism is proposed and confirmed using a simplified dual pulse experiment setup.

The work in this thesis demonstrates two independent methods to monitor redox changes in-situ in the solid state. Further improvements are possible, based on optimizing the characterization system design and memory fabrication process: First, spatial resolution can be achieved if using higher magnification objective lens with long working distance, so the optical system could have the ability to spatially resolve the redox process happened in the channel. Second, the memory retention time may be increased by adding a separator to the current design. Rational control of memory device working environment by designing a sealed and transparent sample holder can also further improve the retention. Finally, doing all the fabrication process in the cleanroom can further eliminate impurities and particles, which may improve the memory reproducibility.

BIBLIOGRAPHY

1. Chih-Yuan, L. and H. Kuan, *Nonvolatile semiconductor memory revolutionizing information storage.* Nanotechnology Magazine, IEEE, 2009. **3**(4): p. 4-9.

2. Scott, J.C. and L.D. Bozano, *Nonvolatile Memory Elements Based on Organic Materials.* Advanced Materials, 2007. **19**(11): p. 1452-1463.

3. Heremans, P., et al., *Polymer and Organic Nonvolatile Memory Devices.* Chemistry of Materials, 2011. **23**(3): p. 341-358.

4. Itoh, T. and R.L. McCreery, *In situ Raman spectroelectrochemistry of electron transfer between glassy carbon and a chemisorbed nitroazobenzene monolayer.* Journal of the American Chemical Society, 2002. **124**(36): p. 10894-10902.

5. Nowak, A.M. and R.L. McCreery, *In situ Raman spectroscopy of bias-induced structural changes in nitroazobenzene molecular electronic junctions.* Journal of the American Chemical Society, 2004. **126**(50): p. 16621-16631.

6. Bonifas, A.P. and R.L. McCreery, *In-situ optical absorbance spectroscopy of molecular layers in carbon based molecular electronic devices.* Chemistry of Materials, 2008. **20**(12): p. 3849-3856.

7. Bergren, A.J. and R.L. McCreery, *Analytical Chemistry in Molecular Electronics.* Annual Review of Analytical Chemistry, Vol 4, 2011. **4**: p. 173-195.

8. Cho, B., et al., *Rewritable Switching of One Diode-One Resistor Nonvolatile Organic Memory Devices.* Advanced Materials, 2010. **22**(11): p. 1228-+.

9. Chen, J.R., et al., *The temperature-dependent physical and electrical characteristics of a polymer/RAFT-polymer stabilized nanoparticle system for organic nonvolatile memory.* Nanotechnology, 2009. **20**(25).

10. Hahm, S.G., et al., *Novel Rewritable, Non-volatile Memory Devices Based on Thermally and Dimensionally Stable Polyimide Thin Films.* Advanced Functional Materials, 2008. **18**(20): p. 3276-3282.

11. Ling, Q.D., et al., *Synthesis and dynamic random access memory behavior of a functional polyimide.* Journal of the American Chemical Society, 2006. **128**(27): p. 8732-8733.

12. Song, S., et al., *Three-Dimensional Integration of Organic Resistive Memory Devices.* Advanced Materials, 2010. **22**(44): p. 5048-+.

13. Waser, R., et al., *Redox-Based Resistive Switching Memories - Nanoionic Mechanisms, Prospects, and Challenges.* Advanced Materials, 2009. **21**(25-26): p. 2632-+.

14. Gregor, L.V., *Polymer Dielectric Films.* Ibm Journal of Research and Development, 1968. **12**(2): p. 140-&.

15. Cho, B., et al., *Organic Resistive Memory Devices: Performance Enhancement, Integration, and Advanced Architectures.* Advanced Functional Materials, 2011. **21**(15): p. 2806-2829.

16. Kumar, R., et al., *Spatially Resolved Raman Spectroelectrochemistry of Solid-State Polythiophene/Viologen Memory Devices.* Journal of the American Chemical Society, 2012. **134**(36): p. 14869-14876.

17. Singh, T.B., et al., *Nonvolatile organic field-effect transistor memory element with a polymeric gate electret.* Applied Physics Letters, 2004. **85**(22): p. 5409-5411.

18. Unni, K.N.N., et al., *A nonvolatile memory element based on an organic field-effect transistor.* Applied Physics Letters, 2004. **85**(10): p. 1823-1825.

19. Naber, R.C.G., et al., *High-performance solution-processed polymer ferroelectric field-effect transistors.* Nature Materials, 2005. **4**(3): p. 243-248.

20. Roncali, J., *Conjugated Poly(Thiophenes) - Synthesis, Functionalization, and Applications.* Chemical Reviews, 1992. **92**(4): p. 711-738.

21. McCullough, R.D., *The chemistry of conducting polythiophenes.* Advanced Materials, 1998. **10**(2): p. 93-+.

22. Ghosh, B. and A.J. Pal, *Conductance Switching in TiO2 Nanorods is a Redox-Driven Process: Evidence from Photovoltaic Parameters.* Journal of Physical Chemistry C, 2009. **113**(42): p. 18391-18395.

23. Shoute, L.C.T., et al., *Redox driven conductance changes for resistive memory.* Applied Physics a-Materials Science & Processing, 2011. **102**(4): p. 841-850.

24. Shrotriya, V., et al., *Absorption spectra modification in poly(3-hexylthiophene): methanofullerene blend thin films.* Chemical Physics Letters, 2005. **411**(1-3): p. 138-143.

25. Jeong, J.W., et al., *The Emission Properties of Integrated Organic Light Emitting Diodes With Organic Photo Sensor for Emotional Lighting Applications.* Ieee Electron Device Letters, 2011. **32**(3): p. 348-350.

26. Sirringhaus, H., N. Tessler, and R.H. Friend, *Integrated optoelectronic devices based on conjugated polymers.* Science, 1998. **280**(5370): p. 1741-1744.

27. Skotheim, T.A., R.L. Elsenbaumer, and J.R. Reynolds, *Handbook of Conducting Polymers*1998: M. Dekker.

28. Mccullough, R.D., et al., *Self-Orienting Head-to-Tail Poly(3-Alkylthiophenes) - New Insights on Structure-Property Relationships in Conducting Polymers.* Journal of the American Chemical Society, 1993. **115**(11): p. 4910-4911.

29. Chen, T.A., X.M. Wu, and R.D. Rieke, *Regiocontrolled Synthesis of Poly(3-Alkylthiophenes) Mediated by Rieke Zinc - Their Characterization and Solid-State Properties.* Journal of the American Chemical Society, 1995. **117**(1): p. 233-244.

30. Klauk, H., *Organic Electronics: Materials, Manufacturing, and Applications*2006: Wiley.

31. Cook, S., A. Furube, and R. Katoh, *Analysis of the excited states of regioregular polythiophene P3HT.* Energy & Environmental Science, 2008. **1**(2): p. 294-299.

32. Sirringhaus, H., et al., *Two-dimensional charge transport in self-organized, high-mobility conjugated polymers.* Nature, 1999. **401**(6754): p. 685-688.

33. Ling, Q.D., et al., *Polymer electronic memories: Materials, devices and mechanisms.* Progress in Polymer Science, 2008. **33**(10): p. 917-978.

34. Chu, C.W., et al., *Organic donor-acceptor system exhibiting electrical bistability for use in memory devices.* Advanced Materials, 2005. **17**(11): p. 1440-+.

35. Liu, G., et al., *Bistable electrical switching and write-once read-many-times memory effect in a donor-acceptor containing polyfluorene derivative and its carbon nanotube composites.* Journal of Applied Physics, 2007. **102**(2).

36. Kamitsos, E.I., C.H. Tzinis, and W.M. Risen, *Raman-Study of the Mechanism of Electrical Switching in Cu Tcnq Films.* Solid State Communications, 1982. **42**(8): p. 561-565.

37. Tseng, T.C., et al., *Charge-transfer-induced structural rearrangements at both sides of organic/metal interfaces.* Nature Chemistry, 2010. **2**(5): p. 374-379.

38. Smits, J.H.A., et al., *Electrically rewritable memory cells from poly(3-hexylthiophene) Schottky diodes.* Advanced Materials, 2005. **17**(9): p. 1169-+.

39. Verbakel, F., S.C.J. Meskers, and R.A.J. Janssen, *Electronic memory effects in a sexithiophene-poly(ethylene oxide) block copolymer doped with NaCl. Combined diode and resistive switching behavior.* Chemistry of Materials, 2006. **18**(11): p. 2707-2712.

40. Chintapalli, S. and R. Frech, *Effect of plasticizers on ionic association and conductivity in the (PEO)(9)LiCF3SO3 system.* Macromolecules, 1996. **29**(10): p. 3499-3506.

41. Donhauser, Z.J., et al., *Conductance switching in single molecules through conformational changes.* Science, 2001. **292**(5525): p. 2303-2307.

42. Lim, S.L., et al., *Conformation-induced electrical bistability in non-conjugated polymers with pendant carbazole moieties.* Chemistry of Materials, 2007. **19**(21): p. 5148-5157.

43. Bandyopadhyay, A. and A.J. Pal, *Multilevel conductivity and conductance switching in supramolecular structures of an organic molecule.* Applied Physics Letters, 2004. **84**(6): p. 999-1001.

44. Carbone, A., B.K. Kotowska, and D. Kotowski, *Space-charge-limited current fluctuations in organic semiconductors.* Physical Review Letters, 2005. **95**(23).

45. Taylor, D.M., *Space charges and traps in polymer electronics.* Ieee Transactions on Dielectrics and Electrical Insulation, 2006. **13**(5): p. 1063-1073.

46. Majumdar, H.S., et al., *Memory device applications of a conjugated polymer: Role of space charges.* Journal of Applied Physics, 2002. **91**(4): p. 2433-2437.

47. Majumdar, H.S., A. Bolognesi, and A.J. Pal, *Conductance switching and data-storage in oriented polymer-based devices: impedance characteristics.* Thin Solid Films, 2004. **446**(2): p. 296-300.

48. Dearnale.G, A.M. Stoneham, and D.V. Morgan, *Electrical Phenomena in Amorphous Oxide Films.* Reports on Progress in Physics, 1970. **33**(11): p. 1129-&.

49. Pagnia, H. and N. Sotnik, *Bistable Switching in Electroformed Metal-Insulator-Metal Devices.* Physica Status Solidi a-Applied Research, 1988. **108**(1): p. 11-65.

50. Dearnaley, G., D.V. Morgan, and A.M. Stoneham, *A model for filament growth and switching in amorphous oxide films.* Journal of Non-Crystalline Solids, 1970. **4**(0): p. 593-612.

51. Joo, W.J., et al., *Study on threshold behavior of operation voltage in metal filament-based polymer memory.* Journal of Physical Chemistry B, 2007. **111**(27): p. 7756-7760.

52. Pender, L.F. and R.J. Fleming, *Memory Switching in Glow-Discharge Polymerized Thin-Films.* Journal of Applied Physics, 1975. **46**(8): p. 3426-3431.

53. Segui, Y., B. Ai, and H. Carchano, *Switching in Polystyrene Films - Transition from on to Off State.* Journal of Applied Physics, 1976. **47**(1): p. 140-143.

54. Sivaramakrishnan, S., et al., *Controlled insulator-to-metal transformation in printable polymer composites with nanometal clusters.* Nature Materials, 2007. **6**(2): p. 149-155.

55. Nguyen, D.N., et al., *Radiation effects on advanced flash memories.* Ieee Transactions on Nuclear Science, 1999. **46**(6): p. 1744-1750.

56. Ouyang, J.Y., et al., *Programmable polymer thin film and non-volatile memory device.* Nature Materials, 2004. **3**(12): p. 918-922.

57. Minami, S. and Y. Kamigaki, *A Novel Monos Nonvolatile Memory Device Ensuring 10-Year Data Retention after 10(7) Erase Write Cycles.* Ieee Transactions on Electron Devices, 1993. **40**(11): p. 2011-2017.

58. de Boer, B., et al., *Synthesis and characterization of conjugated mono- and dithiol oligomers and characterization of their self-assembled monolayers.* Langmuir, 2003. **19**(10): p. 4272-4284.

59. Richter, C.A., C.A. Hacker, and L.J. Richter, *Electrical and spectroscopic characterization of metal/monolayer/Si devices.* Journal of Physical Chemistry B, 2005. **109**(46): p. 21836-21841.

60. Richter, C.A., et al., *Interface characterization of molecular-monolayer/SiO2 based molecular junctions.* Solid-State Electronics, 2006. **50**(6): p. 1088-1096.

61. Skoog, D.A., F.J. Holler, and S.R. Crouch, *Principles of Instrumental Analysis*2007: Thomson Brooks/Cole.

62. Anariba, F., S.H. DuVall, and R.L. McCreery, *Mono- and multilayer formation by diazonium reduction on carbon surfaces monitored with atomic force microscopy "scratching".* Analytical Chemistry, 2003. **75**(15): p. 3837-3844.

63. Blackstock, J.J., et al., *Ultraflat carbon film electrodes prepared by electron beam evaporation.* Analytical Chemistry, 2004. **76**(9): p. 2544-2552.

64. Sakanoue, T. and H. Sirringhaus, *Band-like temperature dependence of mobility in a solution-processed organic semiconductor.* Nature Materials, 2010. **9**(9): p. 736-740.

65. Manceau, M., et al., *The mechanism of photo- and thermooxidation of poly(3-hexylthiophene) (P3HT) reconsidered.* Polymer Degradation and Stability, 2009. **94**(6): p. 898-907.

66. Edwards, J.L., et al., *Insitu and Exsitu Characterization of Gaas/Alas Quantum-Well Structures Using Spectroscopic Ellipsometry.* Journal of Crystal Growth, 1992. **120**(1-4): p. 78-83.

67. Qu, Y.P., et al., *A novel melting behavior of poly(3-alkylthiophene) cocrystals: premelting and recrystallization of component polymers.* Polymer Chemistry, 2012. **3**(12): p. 3301-3307.

68. Wu, J.H., et al., *An ultraviolet responsive hybrid solar cell based on titania/poly(3-hexylthiophene).* Scientific Reports, 2013. **3**.

69. Dissanayake, N.M. and Z.H. Zhong, *Unexpected Hole Transfer Leads to High Efficiency Single-Walled Carbon Nanotube Hybrid Photovoltaic.* Nano Letters, 2011. **11**(1): p. 286-290.

70. Bernardi, M., M. Giulianini, and J.C. Grossman, *Self-Assembly and Its Impact on Interfacial Charge Transfer in Carbon Nanotube/P3HT Solar Cells.* Acs Nano, 2010. **4**(11): p. 6599-6606.

71. Pingel, P., R. Schwarzl, and D. Neher, *Effect of molecular p-doping on hole density and mobility in poly(3-hexylthiophene).* Applied Physics Letters, 2012. **100**(14).

72. Prosa, T.J., et al., *X-Ray Structural Studies of Poly(3-Alkylthiophenes) - an Example of an Inverse Comb.* Macromolecules, 1992. **25**(17): p. 4364-4372.

73. Guo, J.M., et al., *Near-IR Femtosecond Transient Absorption Spectroscopy of Ultrafast Polaron and Triplet Exciton Formation in Polythiophene Films with Different Regioregularities.* Journal of the American Chemical Society, 2009. **131**(46): p. 16869-16880.

74. Korovyanko, O.J., et al., *Photoexcitation dynamics in regioregular and regiorandom polythiophene films.* Physical Review B, 2001. **64**(23).

75. Das, B.C., et al., *Redox-Gated Three-Terminal Organic Memory Devices: Effect of Composition and Environment on Performance.* Acs Applied Materials & Interfaces, 2013. **5**(21): p. 11052-11058.

76. Sullivan, M.G. and R.W. Murray, *Solid-State Electron Self-Exchange Dynamics in Mixed-Valent Poly(Vinylferrocene) Films.* Journal of Physical Chemistry, 1994. **98**(16): p. 4343-4351.

77. Terrill, R.H., et al., *Electric-Field Driven Electron Self-Exchanges in Dry Nafion Containing Mixed-Valent Osmium Bipyridine.* Journal of Physical Chemistry, 1994. **98**(19): p. 5127-5134.

78. Kaihovirta, N., et al., *The Effects of Moisture in Low-Voltage Organic Field-Effect Transistors Gated with a Hydrous Solid Electrolyte.* Advanced Functional Materials, 2010. **20**(16): p. 2605-2610.

79. Johansson, T., N.K. Persson, and O. Inganas, *Moving redox fronts in conjugated polymers studies from lateral electrochemistry in polythiophenes.* Journal of the Electrochemical Society, 2004. **151**(4): p. E119-E124.

80. McCreery, R.L., *Analytical challenges in molecular electronics.* Analytical Chemistry, 2006. **78**(11): p. 3490-3497.